Water management of proton exchange membrane fuel cells
two-phase flow simulation in gas diffusion layers and channels

Yang, Danan

2025

Document Version:
Publisher's PDF, also known as Version of record

Link to publication

Citation for published version (APA):
Yang, D. (2025). *Water management of proton exchange membrane fuel cells: two-phase flow simulation in gas diffusion layers and channels*. [Doctoral Thesis (compilation), Department of Energy Sciences]. Department of Energy Sciences, Lund University.

Total number of authors:
1

LUND UNIVERSITY

PO Box 117
221 00 Lund
+46 46-222 00 00

Water Management of Proton Exchange Membrane Fuel Cells

Two-phase Flow Simulation in Gas Diffusion Layers and Channels

DANAN YANG
DEPARTMENT OF ENERGY SCIENCES | FACULTY OF ENGINEERING | LUND UNIVERSITY

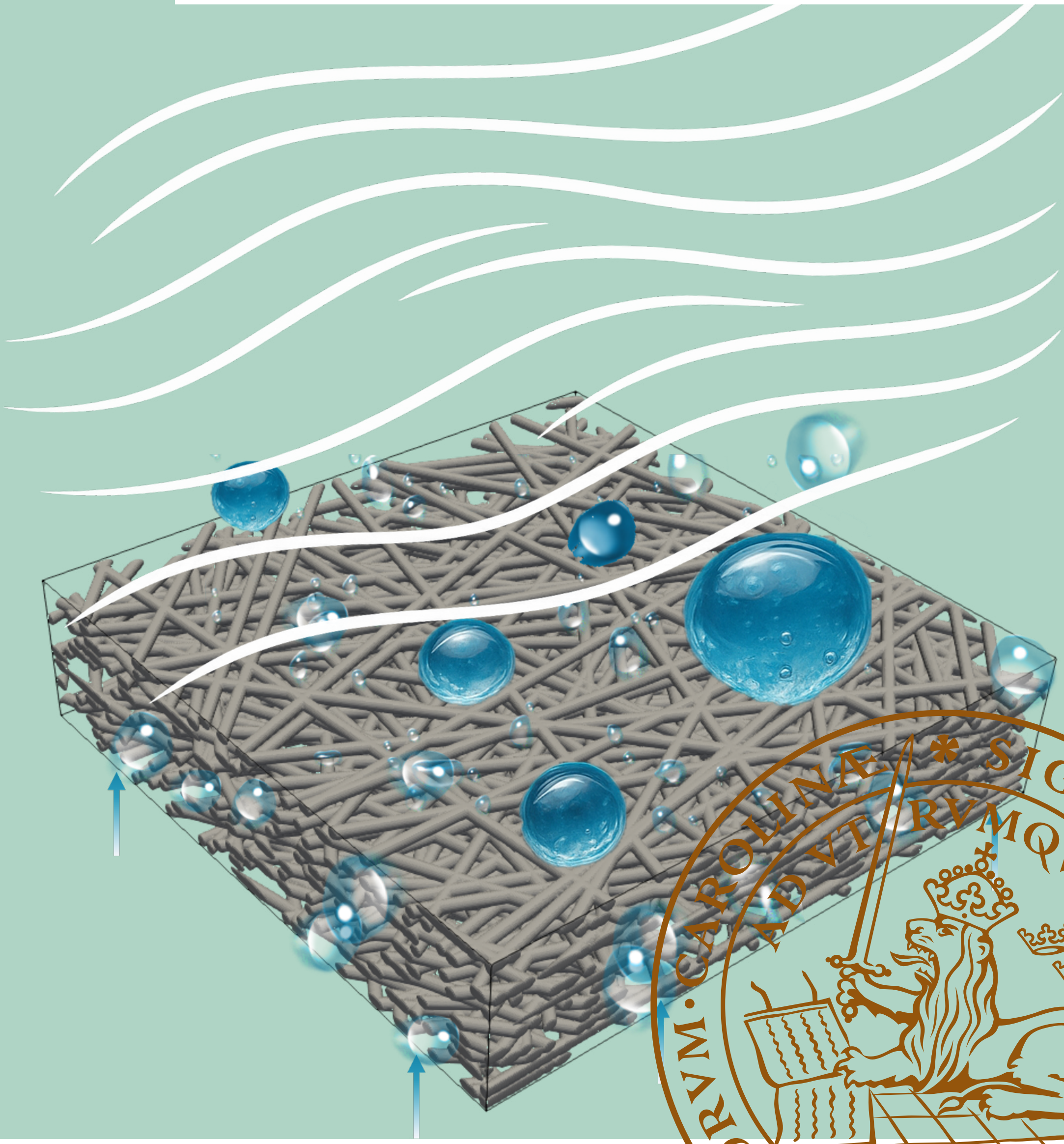

Printed by Media-Tryck, Lund 2025 NORDIC SWAN ECOLABEL 3041 0903

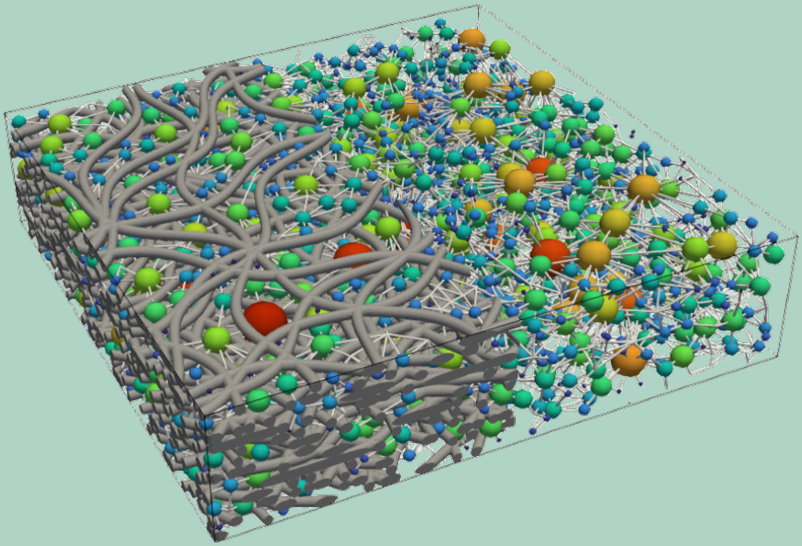

Faculty of Engineering (LTH)
Department of Energy Sciences
Division of Heat Transfer

ISBN 978-91-8104-577-2
ISSN 0282-1990
ISRN: LUTMDN/TMHP-25/1182

LUND
UNIVERSITY

Water Management of Proton Exchange Membrane Fuel Cells
Two-phase Flow Simulation in Gas Diffusion Layers and Channels

Academic Integrity Statement

During the preparation of this thesis, ChatGPT has been employed to polish part of the thesis text. The author preserves full responsibility for the content, originality, and academic integrity of the work. All AI-assisted text revisions have been carefully reviewed and confirmed.

The front cover is generated with the assistance of Sora (OpenAI), together with the provided reference images and command prompts.

All figures and tables are either original contributions or reproduced from published articles with permission from the respective publishers.

All software tools used in this thesis comply with relevant legal and institutional regulations. They are either open-source or operated under appropriate and valid software licenses.

Water Management of Proton Exchange Membrane Fuel Cells

Two-phase Flow Simulation in Gas Diffusion Layers and Channels

Danan Yang

LUND
UNIVERSITY

DOCTORAL DISSERTATION
Doctoral dissertation for the degree of Doctor of Philosophy
Thesis supervisors: Prof. Martin Andersson, Asst. Prof. Himani Garg

Faculty opponent:
Dr.-Ing. Alexander Stroh
Institute of Fluid Mechanics, Karlsruhe Institute of Technology (KIT), Germany.

To be presented, with the permission of the Faculty of Engineering (LTH) of Lund University, for public criticism on Friday, the 29th of August 2025 at 10:15 AM in LTH, Lund, Sweden.

Organization
LUND UNIVERSITY

Department of Energy Sciences
Box 118
SE–221 00 LUND
Sweden

Document name
DOCTORAL DISSERTATION

Date of disputation
2025-08-29

Sponsoring organization
China Scholarship Council (CSC)

Author(s)
Danan Yang

Title and subtitle
Water Management of Proton Exchange Membrane Fuel Cells: Two-phase Flow Simulation in Gas Diffusion Layers and Channels

Abstract

Effective water management remains a significant challenge for proton exchange membrane fuel cells. Water product can accumulate in porous electrodes and flow channels, causing flooding that hinders reactant gas transport to the catalyst sites and degrades performance. Understanding two-phase flow behavior in gas diffusion layers and channels is crucial for improving drainage and overall efficiency.

This thesis presents a series of numerical investigations into two-phase flow in gas channels and gas diffusion layers, utilizing the volume of fluid method within the OpenFOAM v7 framework. The study focuses on the following key aspects: (i) the impact of bipolar plate surface wettability and water inlet design on channel water transport and pressure drop; (ii) the effects of fiber geometry and additive content on gas diffusion layer structure and liquid distribution; and (iii) the influence of liquid inlet configurations and gas outlet conditions of gas diffusion layers on overall water transport. A stochastic reconstruction algorithm was developed to generate the fibrous structure of gas diffusion layers, enabling systematic evaluation of fiber diameter, curvature, and additive content on capillary pressure and water saturation.

Experimental results indicate that prolonged operation of bipolar plates leads to a wettability transition from hydrophobic to hydrophilic, accompanied by performance degradation. This transition further accelerates under sustained use of hydrophilic plates and is associated with increased transport resistance, implying a higher risk of flooding. Two-phase flow simulations in a straight gas channel confirm that hydrophobic surfaces facilitate faster water removal, reduce accumulation, and stabilize pressure drops more effectively than hydrophilic ones.

In addition, two-phase flow simulations of gas diffusion layer and channel assemblies have been conducted. Results reveal that fiber diameter and curvature critically affect two-phase flow in gas diffusion layer and channel assemblies. Larger diameters enlarge pores, causing earlier breakthrough and greater water retention in the gas diffusion layers, while higher curvature enhances capillary pressure and spreading, increasing saturation. Variability in liquid transport mainly stems from random fiber stacking but decreases with increased curvature. Additives reduce small pores; their effect is negligible under hydrophobic conditions at low loadings but becomes significant at higher concentrations. Water inlet configuration of the gas diffusion layer also plays a key role: full-area inlets ensure broad wetting, whereas localized inlets generate discrete flow paths. Allowing reverse gas flow alters liquid distribution, emphasizing counter-flow effects. The results highlight the critical influence of channel surface wettability, water inlet configuration, fiber geometry, and additive content on two-phase transport efficiency.

Key words
Proton exchange membrane fuel cell; Two-phase flow; Volume of fluid; Gas diffusion layer; Gas channel; Water saturation; Capillary pressure; Pressure drop

Classification system and/or index terms (if any)

Supplementary bibliographical information

Language
English

ISSN and key title
ISSN: 0282-1990
ISRN: LUTMDN/TMHP-25/1182

ISBN
978-91-8104-577-2 (print)
978-91-8104-578-9 (pdf)

Recipient's notes

Number of pages
240

Price

Security classification

I, the undersigned, being the copyright owner of the abstract of the above-mentioned dissertation, hereby grant to all reference sources the permission to publish and disseminate the abstract of the above-mentioned dissertation.

Signature ____________________ Date 2025-05-14

DOKUMENTDATABLAD enl SIS 61 41 21

Water Management of Proton Exchange Membrane Fuel Cells

Two-phase Flow Simulation in Gas Diffusion Layers and Channels

Danan Yang

LUND
UNIVERSITY

A doctoral thesis at a university in Sweden takes either the form of a single, cohesive research study (monograph) or a summary of research papers (compilation thesis), which the doctoral student has written alone or together with one or several other author(s).

In the latter case the thesis consists of two parts. An introductory text puts the research work into context and summarizes the main points of the papers. Then, the research publications themselves are reproduced, together with a description of the individual contributions of the authors. The research papers may have already been published or are manuscripts at various stages (in press, submitted, or in draft).

Cover illustration: The front cover includes an AI assistant picture based on a provided stochastic GDL. The back cover shows the pore network extraction from Paper III.

Funding information: Computer time for this research was partly provided by the Swedish National Infrastructure for Computing (SNIC) and its successor, the National Academic Infrastructure for Supercomputing in Sweden (NAISS). This support was provided through funding from the Swedish Research Council under grant agreement no. 2018-05973 and 2022-06725. Additional computational resources were provided by the Centre for Scientific and Technical Computing at Lund University (LUNARC), through reference no. LU 2025/2-40, supported by Lund University. The work is mainly funded by the China Scholarship Council (202006070174).

Division of Heat Transfer
Department of Energy Sciences
Faculty of Engineering (LTH)
Box 118
SE–221 00 LUND
Sweden

ISBN: 978-91-8104-577-2 (print)
ISBN: 978-91-8104-578-9 (pdf)
ISSN: 0282-1990
ISRN: LUTMDN/TMHP-25/1182

Printed in Sweden by Media-Tryck, Lund University, Lund 2025

“天行健，
君子以自强不息；
地势坤，
君子以厚德载物。”
– 《周易》

Contents

List of publications

This thesis is based on the following publications, referred to by their Roman numerals:

I **The influence of bipolar plate wettability on performance and durability of a proton exchange membrane fuel cell**
D. Yang, P. Fortin, H. Garg, M. Andersson
International Journal of Hydrogen Energy, 95, 1284-1298, 2024
https://doi.org/10.1016/j.ijhydene.2024.08.510

II **Numerical simulation of two-phase flow in gas diffusion layer and gas channel of proton exchange membrane fuel cells**
D. Yang, H. Garg, M. Andersson
International Journal of Hydrogen Energy, 48(41), 15677-15694, 2023
https://doi.org/10.1016/j.ijhydene.2023.01.013

III **Effect of fiber curvature on gas diffusion layer two-phase dynamics of proton exchange membrane fuel cells**
D. Yang, M. Andersson, H. Garg
International Journal of Hydrogen Energy, 85, 635-651, 2024
https://doi.org/10.1016/j.ijhydene.2024.08.307

IV **Two-phase fluid dynamics in proton exchange membrane fuel cells: counter-flow liquid inlets and gas outlets at the electrolyte-cathode interface**
D. Yang, S. B. Beale, H. Garg, M. Andersson
Journal of The Electrochemical Society, 171 (10), 104501, 2024
https://doi.org/10.1149/1945-7111/ad7d3d

V **Numerical investigation of two-phase flow transport in additive-treated gas diffusion layers for proton exchange membrane fuel cells**
D. Yang, M. Andersson, H. Garg
Manuscript in preparation

All papers are reproduced with permission from their respective publishers.

Publications not included in this thesis:

I **Analysing tortuosity for solid oxide fuel cell anode material: experiments and modeling**
Xiaoqiang Zhang, **D. Yang**, M. Xu, A. Naden, M. Espinoza-Andaluz, T. Li, J. T. S. Irvine, M. Andersson
Journal of The Electrochemical Society, 170(9): 094502, 2023
https://doi.org/10.1149/1945-7111/acf884

II **Numerical investigation on two-phase flow pressure drop in cathode channels of proton exchange membrane fuel cells**
D. Yang, H. Garg, M. Andersson
ECS Transactions, 114, 577, 2024
https://doi.org/10.1149/11405.0577ecst

III **Numerical reconstruction of proton exchange membrane fuel cell gas diffusion layers**
D. Yang, H. Garg, M. Andersson
ECS Transactions, 112(4), 49, 2023
https://doi.org/10.1149/11204.0049ecst

Acknowledgements

As I begin writing this page, the emotional narrative hidden behind the research finally comes to light. Looking back on my doctoral journey, I recall the loneliness of sitting by the cold window, the hardship of overcoming difficulties, and the joy of sudden enlightenment. I realize that this is not only the mutual replacement of water and gas in the microscopic world of proton exchange membrane fuel cells, but also my self-iteration spanning four years. Those games with two-phase flow simulations are now like water in the cracks, eventually penetrating the disordered topological structure of the gas diffusion layer, turning into water droplets, quietly gathering in the channel, reflecting the light of collective wisdom, and finally flowing to an unknown distance. This incredible journey cannot be accomplished alone. Here, I would like to express my sincere gratitude to those who have provided me with guidance, encouragement, and companionship.

First and foremost, I extend my deepest gratitude to my supervisors, Prof. Martin Andersson and Asst. Prof. Himani Garg. I am deeply grateful to Martin for his trust in my abilities and for providing me with the opportunity to pursue my studies here. I am pleased to witness and celebrate his promotion to Professor. I am also profoundly thankful to Himani, who transitioned from a two-day office mate into my important co-supervisor at the very start of my doctoral journey. I am delighted to see her promotion to Assistant Professor, which is a well-deserved recognition of her dedication and efforts. Their expertise, insightful feedback, and unwavering support have played a crucial role in shaping my academic growth. Their patience and encouragement not only guided my studies but also strengthened my confidence as a researcher. Through their support, I have participated in international conferences, which led to my involvement in two significant collaborations during my doctoral studies. Thanks for Martin's invitation to your home party. I owe special thanks to Himani, whose constant encouragement and meticulous guidance, even down to pronunciation corrections, significantly improved my English presentation skills ahead of my conference talks. Beyond academics, their kindness and support during difficult times for me and my family have been a huge comfort, and I am truly grateful for that.

I am also sincerely thankful to my collaborators, Dr. Patrick Fortin and Prof. Steven B. Beale, for their invaluable insights and contributions, which have significantly enriched my research. I appreciate Steven for his active participation in online discussions, as well as his rigorous expectations in numerical simulations, writing, and visualization, which encouraged me to refine my work. I am equally grateful to Patrick for introducing me to the different experimental aspects of fuel cell research, which broadened my understanding and skill set. This research trip was initially made possible by the help of the Assoc. Prof. Tingshuai Li. Thank you for your valuable advice on applying

for the scholarship and for your greetings during my time abroad. I would also like to thank the senior staff who have made great efforts to secure supercomputing resources, which have greatly benefited my research.

I would also like to thank all my current and former colleagues in the Department of Energy Sciences for creating a friendly and inclusive research environment. I am grateful for the interesting and insightful conversations in the lunchrooms at Kemicentrum and M-huset, and for their collaborative spirit in tackling challenges in both course and research projects. I will cherish many unforgettable shared activities, e.g., department breakfast gathering every Wednesday; making and eating dumplings together in the lunchroom; hiking in Söderåsen national park and Kullabergs naturreservat; paddling on the River Rönne å; picking mushrooms in the forest near Frostavallens strövområde; joint participation in the Lundaloppet running race; Friday jogging; sea water baths and sauna in Bjerreds Saltsjöbad; experiencing nation brunches; after-work drinks, dinner, shuffleboard and bowling games. Many thanks to all the organizers associated with the above-mentioned activities for giving me the opportunity to make my life colorful, vibrant, and less lonely. In these four years, I have seen new people joining this big family, and some leaving after completing their studies or visiting. I have the pleasure of experiencing this family growth along with most of you. For those I have crossed paths with, I have most of your names and faces in my mind, and the group photos in my saved album to remind myself of you guys when I miss this journey in the future. Together with the new PhD students, I wish everyone here all the best and that all their wishes come true.

I want to thank my good friends, who are here and in China right now, for their encouragement, support, and the countless wonderful times. For example, enjoying delicious food made by their own cooking skills, home Karaoke, road cycling, and traveling together in Germany, Hungary, the Czech Republic, Austria, and France, and there are still too many to mention individually. The time we have experienced together in Lund served as a reminder that life is more than just research. I deeply treasure the moments we shared, whether in times of celebration or struggle.

Beyond academia, I really appreciate my father, Lin Yang; my mother, Caixiang Li; my wife, Dr. Lan Yang; my brother, Zhao Yang; my mother-in-law, Yongfang Luo; and my other relatives. Their unwavering love, encouragement, and belief in me have been my most significant source of strength in my academic journey. I know my parents miss me and want to video call me, but they are worried that it will disturb me. My beautiful wife unconditionally supported my decision to study abroad despite the unknown challenges it would bring to our relationship. Her encouragement carried me through the most challenging moments. Our time in different countries is coming to an end, and I look forward to the reunion and building our future together, a future filled with love and shared dreams. Thanks again, my family.

Popular science summary

Green energy is important in making electricity while keeping the planet clean. One terrific way to do this is with a proton exchange membrane fuel cell. It makes electricity using hydrogen and oxygen gas, and the only leftovers are water and heat without pollution. Imagine it like a high-tech sandwich, with layers of different sponge-like ”bread” (called porous structures) in the middle, and each layer is filled with tiny pores of various sizes. The two sides are flanked by plates with grooves (small channels). Hydrogen and oxygen separately enter through channels in the two plates, pass through the tiny connecting pores, and reach the central area. There, a special reaction occurs, producing water and energy to power cars, houses, and more!

While water is naturally made in the fuel cell, it also presents a significant challenge. Since fuel cells work at warm but not very hot temperatures (around 60–80 °C), most of the water stays as a liquid. The water needs to be removed so the fuel cell can keep working smoothly. Think of it like breathing through a straw: if there is too much water inside, the air cannot get through, and one will struggle to breathe. In the same way, if water gets stuck inside the tiny pores and channels of the fuel cell, it blocks the hydrogen and oxygen from getting where they need to go. This makes the fuel cell work less efficiently or even completely stop working. Thus, controlling the water inside the fuel cell is crucial to keep it running well for a long time.

Understanding the movement of water and gases inside fuel cells could provide better guidance for managing water. But, it is not straightforward to observe internal fluid flow directly because the fuel cells have a closed and opaque structure. Advanced image scanning techniques are utilized to visualize water movement, much like using X-rays or nuclear magnetic resonance to reveal internal structures in the human body. However, these methods are expensive, difficult to access, and not flexible enough for many studies. As a result, computer-based numerical simulations have emerged as a viable alternative. These models provide a three-dimensional representation of velocity, pressure, and water content over time, offering insights that are otherwise difficult to obtain experimentally.

Even though significant improvements have been made in studying how water and air move in fuel cells, there are still many unanswered questions. One of the ongoing debates is: Should the inside walls of fuel cell channels repel water (hydrophobic) or attract it (hydrophilic) to work better? Another challenge is that many simulations study different parts of the fuel cell separately, such as the gas channels or one of the sponge-like porous layers made of stacked tiny fibers (hence the fibrous layer). Few studies have examined how these two layers work together, making it harder to understand how water flows between them. Another research gap involves the role of fiber

structure within the fibrous porous layer. The effects of fiber shape, such as thickness and curvature, on the overall pore structure and water transport remain underexplored. Furthermore, defining how water enters the simulation space is not standardized. Different models use varying inlet designs, ranging from local to global water inputs or single-hole versus multi-hole configurations. The impact of these choices on simulation accuracy is not yet fully understood.

To address these limitations, this thesis employs a popular numerical model, the volume of fluid model, in an open-source simulation framework to examine water-gas transport in a porous layer and channel assembly. This model can simulate how water and gases move while maintaining a clear boundary between them, ensuring their natural separation, also known as immiscibility. A new method for reconstructing the fibrous porous layer has been developed, mimicking the stacking of cylindrical spaghetti in a bowl to create pore spaces. The findings reveal that hydrophobic channel surfaces initially enhance water removal but may gradually develop a hydrophilic property over time, affecting long-term performance. The study also shows that increasing fiber diameter reduces water accumulation in the porous layer but leads to greater accumulation in the gas channel, requiring a balance in drainage design. Additionally, fiber curvature has a significant impact on water movement. Higher curvature increases the number of small pores, which slows down water transport and causes water to remain trapped for longer periods. It is like water in a dense sponge with tiny pores, moving slowly, while in a loose sponge with larger pores, it can flow easily.

Another important discovery is that the randomness of fiber influences simulation outcomes. Even when porous layers have nearly identical porosity (pore space) and dimensional size, differences in fiber arrangement during stacking led to variations in water behavior. In particular, straight-fiber porous domains exhibited inconsistent water distribution, while curved-fiber porous domains had more uniform saturation patterns. This suggests that running multiple simulations with different random fiber arrangements is crucial for obtaining reliable predictions, a factor that has been frequently overlooked in previous studies. Furthermore, the results indicate that the water inlet configuration has a significant influence on drainage patterns. To ensure more accurate assessments of porous layer performance, a global inlet design is recommended for thorough evaluation of water transport.

This thesis makes two significant contributions to the field. First, it introduces a novel method for reconstructing fibrous porous structures, incorporating fiber characteristics to provide a more realistic model for studying the internal fluid transport. Second, the simulation results provide more profound insights into two-phase flow behavior, enabling future studies to enhance fuel cell design and develop more efficient water management strategies for proton exchange membrane fuel cells.

Abstract

Proton exchange membrane fuel cells are a promising green energy conversion technology for clean and sustainable power generation. However, effective water management remains a critical challenge. Water produced by electrochemical reactions can accumulate within porous electrodes and flow channels, leading to flooding that impedes the reverse transport of reactant gases to the reaction zone, thereby reducing fuel cell efficiency. A comprehensive understanding of two-phase flow behavior within gas diffusion layers and channels is essential for optimizing water removal strategies and enhancing overall performance. Despite extensive experimental and numerical investigations, the detailed dynamics of liquid–gas transport and interfacial interactions in these components remain inadequately characterized.

This thesis presents a series of high-fidelity numerical investigations of two-phase flow evolution in gas channels and gas diffusion layers, conducted using the volume of fluid method within the OpenFOAM v7 framework. The research investigates the water-gas interactions with a focus on (i) effects of bipolar plate surface wettability and water inlet configuration on channel water transport and pressure drop; (ii) the influence of fiber shape and additive content on microstructure topology and transport properties; and the role of liquid inlet configurations and gas outlet boundary conditions of gas diffusion layers on water transport. To facilitate these analyses, a stochastic reconstruction algorithm was developed to generate detailed fibrous representations of the gas diffusion layer, enabling a systematic study of fiber diameter, curvature, and additive structure content on capillary pressure and water saturation.

Experimental characterization of proton exchange membrane fuel cells reveals performance degradation concomitant with a transition of bipolar plate surface wettability from hydrophobic to hydrophilic following extended operation. This degradation process accelerates under continuous use of hydrophilic plates and correlates with increased transport resistance, suggesting an elevated flooding probability. To verify this hypothesis, two-phase flow simulations conducted in a straight gas channel demonstrate that hydrophobic channel surfaces promote more rapid water evacuation, minimize water accumulation, and stabilize pressure-drop fluctuations more effectively than hydrophilic surfaces.

In addition, two-phase flow simulations of gas diffusion layer and channel assemblies reveal that fiber diameter and curvature exert a pronounced influence on liquid transport. At constant porosity, increasing the fiber diameter enlarges pore spaces, precipitating earlier liquid breakthrough and increasing water retention within the gas diffusion layer, while reducing saturation levels in the adjoining hydrophilic flow channels. Conversely, increasing fiber curvature introduces a greater proportion of smaller pores, increasing capillary pressure and promoting liquid spreading, which in turn enhances overall water saturation. Multi-sample analyses, employing consistent stochastic reconstructions, indicate that variability in liquid transport arises principally from the random stacking of fibers. Nevertheless, this variability may be mitigated by increasing fiber curvature. In addition, the introduction of the additive predominantly decreases the fraction of smaller pores. As a result, at relatively low additive loadings, the additive exerts minimal influence on water saturation under highly hydrophobic conditions. However, once the additive concentration exceeds a certain threshold, its effect on water removal cannot be neglected, yielding a notable reduction in water retention. Comparative evaluation of distinct inlet configurations further demonstrates that the spatial distribution and size of liquid entry profoundly alter two-phase transport. A full-area inlet yields broad wetting coverage, whereas localized inlets generate discrete flow pathways. Under a localized inlet scheme, permitting reverse gas outflow at the diffusion layer lower corners alters liquid propagation patterns, underscoring the necessity of accounting for counter-flow effects in two-phase flow studies.

This work is expected to enhance the understanding of two-phase interaction within gas diffusion layers and gas channels. The findings emphasize the pivotal roles of fiber geometry, additive content, channel surface wettability, and liquid inlet arrangement in governing transport efficiency. However, to offer practical guidance for manufacturing and application, the present findings should be integrated with complementary studies on gas diffusion layer functionality, including gas transport, electrical conductivity, and thermal conductivity, as well as the compatibility between different components.

Nomenclature

Symbol	**Unit**	**Description**
$\mathbf{u}$	m/s	Velocity
$\mathbf{f}_\sigma$	N	Surface tension force
$\mathbf{g}$	m/s^2	Gravitational acceleration factor
μ	Pa·s	Dynamic viscosity
ρ	kg/m^3	Density
σ	N/m	Surface tension coefficient
θ	$^\circ$	Contact angle
d	μm	Fiber diameter
S	$-$	Water saturation
V	m^3	Volume
A	m^2	Surface area
P_c	Pa	Capillary pressure

Superscript	**Description**
g	Gas
l	Liquid
w	Water
p	Pore

Abbreviation	**Description**
PEMFC	Proton Exchange Membrane Fuel Cell
GC	Gas Channel
GDL	Gas Diffusion Layer
CL	Catalyst Layer
MPL	Microporous Layer
BPP	Bipolar Plate
VOF	Volume of Fluid
PTFE	PolyTetraFluoroEthylene
HOR	Hydrogen Oxidation Reaction
ORR	Oxygen Reduction Reaction

Chapter 1

Introduction

1.1 Background

The rapid global industrialization and the over-exploitation of fossil fuels have significantly intensified the ongoing climate crisis and accelerated environmental degradation. In response, 197 member parties of the United Nations Framework Convention on Climate Change unanimously agreed at the Paris Climate Change Conference to adopt the Paris Agreement on December 12, 2015. Each country agreed to limit the global temperature increase to less than 2 °C and work to limit the global temperature increase to less than 1.5 °C [1]. In 2017, Sweden was the first nation to legislate a mid-century—2045—net-zero target. As of May 2024, 148 countries worldwide have made explicit commitments to carbon neutrality and to achieve net-zero carbon emissions by 2050-2070 [2]. However, at the beginning of 2024, the World Meteorological Organization confirmed that the global mean near-surface temperature in 2023 reached a record-breaking value of 1.45 ± 0.12 °C above pre-industrial levels [3]. Furthermore, the average temperature for the period from January to September 2024 was reported as 1.54 ± 0.13 °C, placing the year 2024 on track to create a new record. This temperature has been around 1.5 °C, as called for in the Paris Agreement. Therefore, it has become an increasingly urgent global imperative to develop green, sustainable, and efficient technologies that enable the transition to clean energy while simultaneously meeting the growing energy demand.

Carbon dioxide is principally a representative greenhouse gas, which can be produced during transportation, agriculture, and power generation using fossil fuels such as coal and natural gas. To reduce the utilization of fossil fuels, hydrogen energy, as a clean, efficient, and zero-emission energy carrier, is emerging as a cornerstone of the global energy transition. It plays a vital role in transportation, power generation, industrial processes, and energy storage, enabling decarbonization across multiple sectors. Among the various hydrogen energy applications, fuel cells have gained significant attention due to their ability to convert chemical energy directly into electricity via electrochemical reactions. Proton Exchange Membrane Fuel Cell (PEMFC) is a type of fuel cell, which operates at a relatively low temperature range (60-80 °C), produces high power density with an electrical efficiency of 40-60% and water as the byproduct [4]. Moreover, its fast start-up enables dynamic load regulation. These characteristics align with the goals of environmental protection and carbon neutrality. Thus, PEMFCs hold great potential for application in transportation, stationary, and portable power systems. Specifically, transportation applications include fuel cell vehicles, buses, trucks, trains, drones, ships, and aircraft. Stationary utilization includes microgrids, data centers, backup power, and combined heat and power systems. Portable settings include military field operations and emergency scenarios [5].

PEMFC technology has made significant progress over the past 20 years, with around a 60% decrease in fuel cell system cost compared to 2006 [6]. However, large-scale commercialization of high-performance PEMFC systems still faces critical barriers, like a relatively short lifespan and high costs from manufacturing to operation and maintenance. For instance, Toyota announced the latest fuel cell electric vehicle, the Mirai XLE, with a starting suggested retail price of \$ 50,190, which is much higher than the price of battery electric vehicles, e.g., the Tesla Model 3 with a cost of around \$ 35,000. The Department of Energy of the United States has established the following goals by 2030 to develop a 68% peak-efficient direct hydrogen fuel cell system for heavy-duty trucks with 25,000-hour durability and a production cost of \$ 80/kW, and stationary systems with 80,000-hour durability at \$ 1000/kW [7]. To achieve these goals, it is necessary to optimize manufacturing processes, materials, and operations to enhance power density, reduce cost and degradation, and minimize maintenance.

Water management has been a significant issue while operating a PEMFC. Figure 1.1(a) and (b) present the schematic diagram of a PEMFC internal structure and working principle, respectively. A PEMFC consists of a Proton Exchange Membrane (PEM) in the middle and different electrode layers on both sides, i.e., Catalyst Layers (CLs), Gas Diffusion Layers (GDLs), and Microporous Layers (MPLs). At both ends, Bipolar Plates (BPPs) are sandwiched with grooves, forming Gas Channels (GCs). Similar structures exist in the cathode and anode regions. Fig. 1.1(b) illustrates the transport of reactants and products, like water (marked in blue), heat, and electricity. It shows a comprehensive view of the coupled multiphysics in PEMFCs. During operation, hydrogen gas diffuses to the anode CLs and undergoes the Hydrogen Oxidation Reaction (HOR), producing protons and electrons. Protons migrate through the membrane to the cathode, while electrons flow through the external circuit, generating current. Simultaneously, oxygen at the cathode reacts with protons and electrons via the Oxygen Reduction Reaction (ORR), forming water. The HOR and ORR reactions are shown in Eq. 1.1.

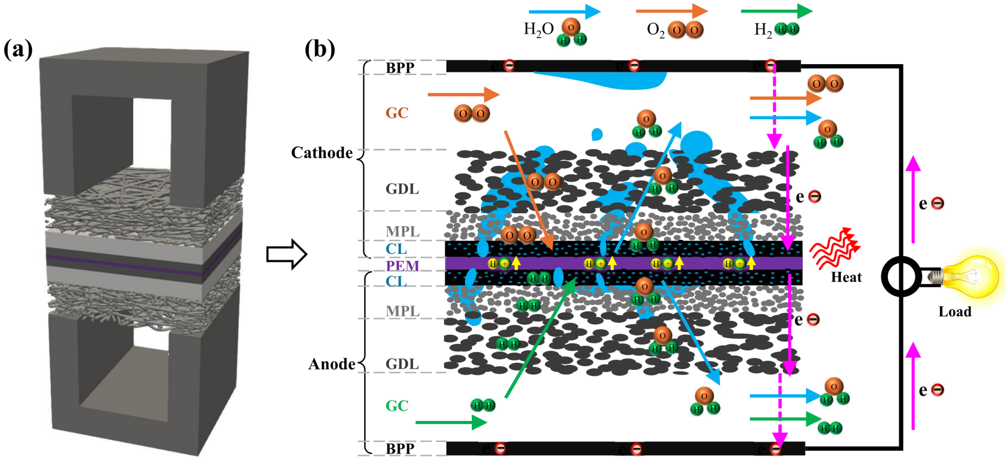

Figure 1.1: (a) A representative region of a PEMFC sandwich structure. (b) Schematic cross-sectional view of the internal structure of the PEMFC, showing reaction species transport, water (marked in blue), heat, and electricity transport across different components. BPP: bipolar plate; GC: gas channel; GDL: gas diffusion layer; MPL: microporous layer; CL: catalyst layer; PEM: proton exchange membrane.

$$\begin{aligned} \text{Anode HOR:} \quad & 2H_2 \rightarrow 4H^+ + 4e^- \\ \text{Cathode ORR:} \quad & O_2 + 4H^+ + 4e^- \rightarrow 2H_2O \\ \text{Net:} \quad & 2H_2 + O_2 \rightarrow 2H_2O \end{aligned} \tag{1.1}$$

As PEMFC operating temperatures are typically less than 100 °C, water product within the cathode region exists predominantly in the liquid state because of vapor condensation [8]. In addition, the liquid water at the cathode creates a chemical potential gradient across the membrane, where liquid water will diffuse across the PEM towards the anode side via back-diffusion. While suitable hydration is essential for maintaining membrane proton conductivity, excessive water can lead to flooding, where liquid water accumulates in the porous electrodes and channels, blocking reactant gas transport and reducing fuel cell performance, particularly under high-current-density conditions. Uneven water distribution can also cause localized oxygen starvation, leading to increased overpotential and efficiency loss. In cold conditions, unremoved water may freeze, which will obstruct channels and hinder startup, while membrane dehydration due to poor water distribution increases ohmic resistance and risks structural damage. To highlight the importance of water management in fuel cell performance, Fig. 1.2 shows the time-dependent cathode and anode pressure drops at various output voltages, based on the experimental results of Trabold *et al.* [9]. As the output voltage decreases from 0.7 V to 0.5 V, the resulting increase in current density enhances electrochemical reactions and liquid water production. This leads to rising pressure drops on both sides, with more substantial fluctuations observed at the cathode. Notably, the cathode pressure drop fluctuations correlate closely with voltage fluctuations in Fig. 1.2(a), underscoring the need for effective water management on both anode and cathode sides to reduce flooding risk and ensure stable performance.

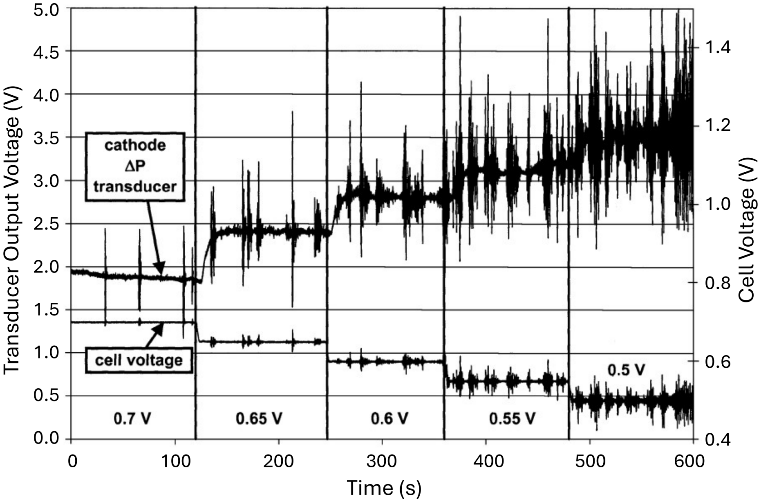

Figure 1.2: Experimental results by Trabold *et al.* [9] on the fluctuation in cathode ΔP signal and cell voltage. The transducer output voltage is positively correlated with the pressure. (Reprinted by the permission of the publisher)

1.2 Summary of knowledge gaps

An in-depth investigation into the two-phase flow behavior within PEMFC components is beneficial for informing the design of flow channels and electrode architectures, thereby enabling the optimization of water and gas transport properties and improving performance while reducing degradation in PEMFC systems. In the past decades, significant progress has been made in understanding various aspects of two-phase flow behavior in PEMFCs, which will be introduced in Chapter 2. Some knowledge gaps have been identified, motivating the work presented in this thesis. These gaps can be summarized as follows:

1. **No consensus wettability for GC surface**. The influence of channel wettability on fuel cell performance remains insufficiently characterized. Current research still remains controversial regarding the choice of hydrophobic and hydrophilic channels. Moreover, there is a lack of research investigating the changes in BPP channel wettability after prolonged utilization.

2. **Two-phase flow studies in isolated domains**. Many previous studies focus on individual regions, such as the MPL, GDL, and GC, and only a few studies con-

sider adjacent regions due to the high computational cost of interface-resolved two-phase flow simulations. In particular, the coupled liquid transport within GDL and GC assemblies and across their interface remains poorly understood.

3. **Unclear impact of GDL fiber structure.** Many studies have focused on the effects of various structural parameters of GDLs. However, carbon fiber has received relatively little attention. The impact of carbon fiber shapes, such as diameter and curvature, on the entire pore structure properties remains unclear. Moreover, the random algorithms for generating curved-fiber GDLs remain underdeveloped, and such structures are typically derived from experimental scans, limiting further research progress.

4. **Various water inlet configurations**. Due to the challenge of coupling electrochemical reactions with interface-resolved models like the VOF method, previous two-phase flow studies have introduced water flow by initializing water droplets within the simulation domain or by inputting water from one or several pores. However, there are no standardized criteria for determining the location, size, and number of water inlet holes. All the water injection configurations seem to be randomly decided in numerical and even ex-situ experimental studies. This may omit critical water transport features, leading to misleading conclusions. The resulting discrepancies warrant further investigation.

5. **Neglecting GDL gas outlets**. At the interface of two cathode components in a PEMFC, the processes of liquid removal and reactant transport coincide. However, only one study has been found to discuss the gas outlet boundary condition at the liquid injection surface using interface-resolved two-phase flow simulations. Since the gas outlet is neglected, the simultaneous countercurrent flow in actual fuel cell operation is not represented, resulting in a limited understanding of the liquid-gas dynamic interaction.

1.3 Research objectives

The overall goal of this study is to provide new insights into the two-phase flow behavior within the GDL and GC of PEMFCs, with particular focus on addressing the research gaps identified in Section 1.2. To achieve this, a series of high-fidelity numerical simulations are conducted using a VOF model implemented within the open-source computational fluid dynamics platform OpenFOAM (version 7). The specific objectives of this study are outlined as follows:

1. Two-phase flow in GCs:
    - Investigating the influence of BPP wettability transitions on the performance and durability of PEMFCs by experimental electrochemical characterization.
    - Elucidating the interaction mechanisms between liquid water transport and gas pressure drop in GCs, accounting for varying GC surface wettability and liquid water injection configurations.
2. Two-phase flow in the GDL/GC assemblies:
    - Developing a stochastic reconstruction algorithm capable of simulating the real GDL fiber structure, ensuring a reasonable representation of the morphological properties.
    - Analyzing the relationship between pore network (distribution and connectivity) and water distribution results by VOF simulations.
    - Studying the effect of carbon fiber diameter and curvature, and additive structure on the water behavior in GDLs and GCs as well as their interface, e.g., saturation, breakthrough, and capillary pressure.
    - Investigating the effect of simultaneous GDL liquid inlet and gas outlet boundary conditions on the interaction between liquid and gas in GDL and GC.

1.4 Thesis outline

This thesis is structured as follows. Chapter 2 provides a brief overview of the previous relevant two-phase flow studies in PEMFCs. Chapter 3 outlines the numerical methodology employed for the two-phase flow simulations in this thesis, including the governing equations, numerical schemes, boundary conditions, meshing strategies, and post-processing techniques. Chapter 4 presents the developed stochastic reconstruction of the fibrous GDL and the extraction of its pore network. Chapter 5 focuses on evaluating the reliability of the increased liquid velocity and VOF model, while also introducing the simulation cases to be studied. Chapter 6 synthesizes the key findings from the research papers included in this thesis, highlighting their contributions to the field. Finally, Chapter 7 concludes the thesis by summarizing the main insights and proposing potential directions for future research. The complete published papers and their author contributions are provided in the appendix for reference.

Chapter 2

Literature review on PEMFC two-phase flow

2.1 Two-phase flow investigation methods

Suitable water management requires an in-depth understanding of the PEMFC two-phase flow coupling transport mechanisms in multiple time scales (from microseconds to minutes) and length scales (molecular scale, mesoscale, microscale, cell scale, stack scale, or system scale) [10], which leads to the adoption of different numerical and experimental approaches depending on the specific research objectives.

2.1.1 Experimental visualization techniques

The opaque materials and inherent complexity of the fuel cell structure result in challenges to direct visualization experiments on two-phase flow. Several studies [11, 15–17] have employed transparent materials to replace parts of the structure, allowing the fluid flow behavior to be photographed and recorded by high-speed cameras through the transparent window. This method is relatively cheap and easy to implement for in situ observation. Many of these experiments can only provide a two-dimensional view of the water flow in the flow channel. Additionally, they may sometimes fail to match the actual structure in terms of surface wettability, roughness, and thermal and electrical conductivity properties. To avoid altering the structure while enabling high-resolution observation, various advanced visualization techniques have been employed. These include laser induced fluorescence [18], fluorescence microscopy [19], X-ray computed tomography [20, 21], synchrotron X-ray radiography [14, 22], neut-

General application scenarios in PEMFC	Popular visualization techniques	Spatial Resolution	Temporal Resolution	Cost: e.g., purchase and maintenance
Adopting transparent materials	High-speed camera	Low	Super high	e.g., \$50,00-\$50,000
	Laser-induced fluorescence	Medium	High	Typically, much higher than that of a high-speed camera.
	Fluorescence microscopy	Medium to High	High	
Keeping original opaque and closed components	(Synchrotron) X-ray computed tomography	High	Medium	
	Synchrotron X-ray radiography	Super high	High	
	Neutron radiography	Low to Medium	Low	
	Magnetic resonance imaging	Low to Medium	Low	
	Environmental scanning electron microscope	High	Low	

Spatial Resolution: “Super high” ”(<10 µm), “High”(1-10 µm), “Medium”(10-100 µm), “Low”(>100 µm)
Temporal Resolution: “Super high” ”(<10 µs), “High”(10 µs-1 ms), “Medium”(1 ms-1 s), “Low”(>1 s)

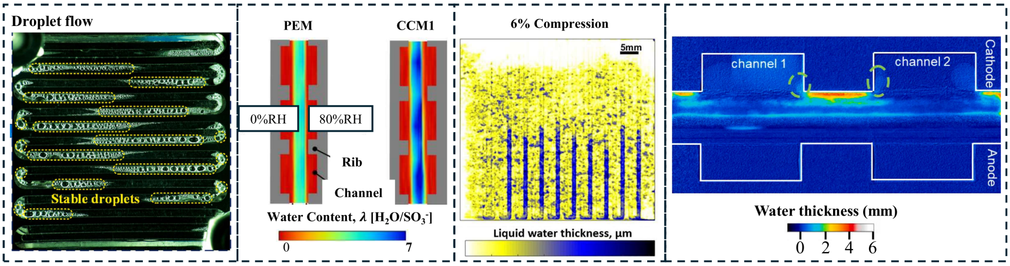

High-speed camera | Magnetic resonance imaging | X-ray computed tomography | Synchrotron X-ray radiography

Figure 2.1: Classification of two-phase flow experimental visualization techniques adopted in PEMFC research, including some results using high-speed cameras [11], neutron radiography [12], magnetic resonance imaging [13], and synchrotron X-ray radiography [14]. Figures are adapted separately from Li *et al.* (Renewable Energy, 2023) [11], Wu *et al.* (Energy Conversion and Management, 2021) [12], Suzuki *et al.* (International Journal of Hydrogen Energy, 2011) [13], and Kato *et al.* (International Journal of Hydrogen Energy, 2024) [14], with permission from Elsevier.

ron radiography [12, 23–25], and magnetic resonance imaging [13]. Most of these methods enable high-resolution imaging of structural components or two-dimensional flow patterns. Techniques like X-ray computed tomography and MRI further allow for three-dimensional structural or flow reconstruction under specific conditions. A simple comparison among them has been shown in Fig. 2.1. In general, these techniques involve a careful trade-off between temporal resolution, spatial resolution, scanning range, dimensionality, and observing duration, as well as time and money costs. For example, X-ray radiography cannot realize high temporal and spatial resolutions at the same time [26]. Moreover, access to advanced scanning technologies, i.e., neutron radiography and synchrotron radiation, is still limited and expensive. Advanced diagnostic techniques continue to evolve. For example, Ziesche *et al.* [27] introduced a four-dimensional high-speed neutron computed tomography method to capture transient water dynamics in fuel cells. This technique allows for quantifying the relationship between fuel cell performance and water transport across the anode and cathode channels, as well as within the membrane electrode assembly.

2.1.2 Numerical simulation models

In contrast, with reasonable model validation based on the experimental data, numerical simulation of two-phase flow offers a promising alternative to overcome the aforementioned experimental limitations. It enables detailed exploration of two-phase flow within fuel cells with enhanced flexibility and more physical field information, including steady or transient fluid distribution, pressure, velocity, temperature, and others. All of these factors make it an increasingly attractive approach in PEMFC research, as well as in other research areas. Several commonly used two-phase flow simulation methods are categorized according to different criteria, as shown in Fig. 2.2.

Generally applied scenarios in PEMFCs	Popular two-phase flow models	Capturing interface	Generally applied length scale	Computational unit
Multiphysics in an entire fuel cell unit or stack	(Two-phase) Darcy's law	No	Macro-scale	Mesh grid (Finite element、Finite volume、Finite difference methods)
	Mixture model			
	Eulerian-Eulerian model			
Liquid-gas fluid transport within channels and porous electrodes (GDL, MPL)	Volume of fluid method	Yes	Macro-/Micro-scale	
	Phase field method			
	Level-set method			
Liquid-gas transport in porous electrodes (GDL, MPL, and CL)	Lattice Boltzmann method	Yes	Micro-/Meso-scale	Lattice node
	Pore network model	No	Micro-/Meso-scale	Pore-throat network

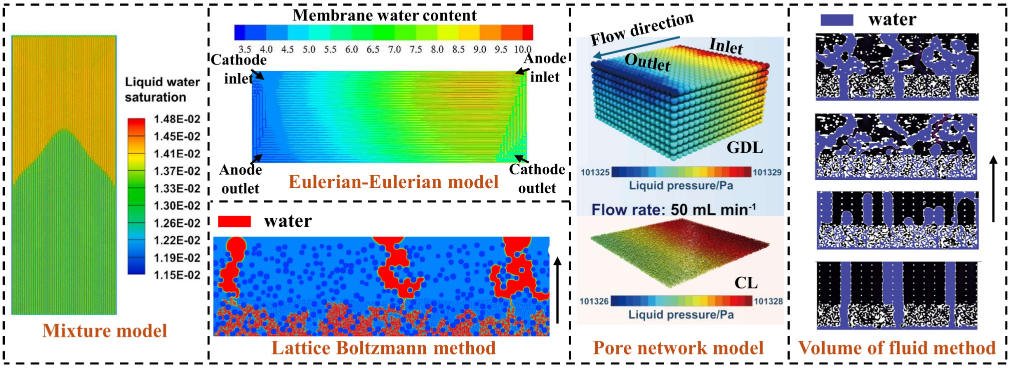

Figure 2.2: Classification of two-phase flow numerical simulation methods adopted in PEMFC research. Some previous results based on the Mixture model [28], Eulerian-Eulerian model [29], lattice Boltzmann method [30], pore network model [31], and the VOF model [32] are presented. Figures are adapted separately from Wang *et al.* (Journal of Power Sources, 2024) [28], Zhang *et al.* (International Journal of Heat and Mass Transfer, 2019) [29], Kim *et al.* (Journal of Power Sources, 2015) [30], Xu *et al.* (Energy Conversion and Management, 2024) [31], and Niblett *et al.* (Journal of Power Sources, 2020) [32], with permission from Elsevier.

It is essential to recognize that all models can be adjusted to achieve a balance between research goals, computational efficiency, and accuracy. Over recent decades, Darcy's Law [33–37], the mixture model [28, 38, 39], and Eulerian-Eulerian models [29, 40, 41] have been utilized to simulate multiphysics coupling problems in PEMFCs. Darcy's

Law simplifies fluid flow analysis in complex porous structures, such as GDLs and MPLs, by ignoring detailed local flow characteristics, including microscale effects. Instead, it relates the average flow velocity to the pressure gradient [42]. On the other hand, mixture models propose a shared velocity field for all phases and introduce slip velocity between phases through an additional equation [43]. This method accounts for relative motion between phases and is suitable for scenarios with limited local liquid water distribution in porous materials and minor relative movement between phases. Furthermore, Eulerian-Eulerian models treat each phase as a continuous medium and separately resolve the mass, momentum, and energy conservation equations for each phase, while accounting for phase-relative motion [44]. Although this technique offers more granularity, it is more computationally expensive than Darcy or mixture models. To decrease the computational load, the pore network model has been widely used for simulations of porous media, including those in porous electrodes in PEMFCs [31].

However, none of these aforementioned methods explicitly resolves the interface between liquid water and reactant gases (air/O_2 and H_2), which are inherently immiscible. Therefore, different interface-resolved models have been adopted to study the detailed liquid-gas interaction behavior, including the VOF method [45, 46], lattice Boltzmann method [47], Level-set model [48], and phase-field model [49]. All these methods have also been used to simulate two-phase flow problems in PEMFCs, which will be discussed in the next section. Among them, the VOF method has emerged as the dominant method in studying droplet dynamics in PEMFCs. Since its introduction by Hirt and Nichols [45], the VOF method has been widely used to track interfaces between immiscible fluids, such as gas and liquid. It has since been developed and commonly applied in fields such as chemical engineering, oil and gas, and aerospace. One of its main strengths is its ability to handle complex interface phenomena, such as bubble formation, merging, and breakup.

Despite the widespread usage of VOF models, ongoing development continues to aim for an improved balance between accuracy and efficiency. VOF method is generally categorized into three types: algebraic VOF [50], geometric VOF [51], and coupled level-set VOF [52]. Algebraic VOF estimates phase transport using numerical schemes without explicitly reconstructing the interface. In contrast, geometric VOF reconstructs the interface (e.g., via piecewise linear interface construction) and calculates volume fluxes using geometric operations. The coupled level-set VOF method combines the mass conservation of VOF with the smoother interface tracking of level-set methods. A detailed overview of these approaches is provided by Mirjalili *et al.* [53]. Some comparative studies have found that geometric VOF and coupled level-set VOF offer higher accuracy, but at a greater computational cost [54]. In geometric VOF, accuracy depends heavily on the choice of sub-algorithm. When it is used with unstructured three-dimensional meshes, data transfer between parallel processes can cause load imbalance [55, 56]. To address this, Roenby *et al.* [57] developed the isoAdvector algorithm, later improved with distance-based reconstruction [58]. A recent unsplit geometric VOF scheme combining isoAdvector and contour-based reconstruction shows good performance in both accuracy and efficiency [59]. Algebraic VOF methods, in contrast to geometric reconstruction techniques, update the volume fraction field using algebraic formulations, typically based on flux-limited advection schemes, without explicitly reconstructing the interface geometry. This approach simplifies implementation and enhances robustness, particularly when applied to three-dimensional unstructured meshes and complex geometries. Their simplicity, lower computational cost, and compatibility with existing solvers contribute to their widespread use in engineering applications. However, this comes at the expense of increased numerical diffusion and reduced interface sharpness compared to geometric methods. Selecting an appropriate VOF approach involves balancing accuracy, interface resolution, and computational efficiency in accordance with the simulation goals and practical constraints.

2.2 Microscale two-phase flow simulation

This section reviews previous microscale two-phase flow simulations, with a particular focus on those employing interface-resolved methods. These studies are categorized as follows: Section 2.2.1 shows the various simulation domains; Section 2.2.2 presents the representative approaches for incorporating the liquid phase; Sections 2.2.3 and 2.2.4 examine the effects of surface wettability and microstructural topology, respectively, on water transport in channels and porous electrodes.

2.2.1 Simulation domain

Currently, all the interface-resolved two-phase flow models are limited by expensive computation and thus cannot simulate the water flow inside the entire fuel cell but focus on certain components, which can be sorted into GC [60–72], GDL [73–81], MPL [80, 82, 83]. Some studies also consider coupled domains such as GDL-GC [32, 84, 85] and GDL-MPL [30, 81, 86, 87]. Most existing work focuses on water flow behavior within either the GDL or GC, leaving several limitations unresolved. For example, 1) The GC water inlets are arbitrarily determined, rather than being simulated as the flow originating from the GDLs. 2) The fluid interaction between the gas flow in the GC and the breakthrough liquid in the GDL is not considered, and the water dynamics at their interface are simplified. To capture the actual flow dynamics in GDL/GC assemblies, it is essential to model the natural development of liquid transport from connected GDLs, rather than prescribing artificial water injection points in the GC.

Such an approach eliminates uncertainty introduced by user-defined boundary conditions and provides a more physically accurate representation of interfacial dynamics. Some studies include GC domains when focusing on the GDL but treat the GC as a space without active airflow [88, 89]. A more comprehensive approach was taken by Niblett *et al.* [32], who used the VOF method to simulate two-dimensional and three-dimensional two-phase flow in an MPL-GDL-GC configuration. Their results aligned well with experimental observations, and the MPL was represented with a crack-like structure connecting the GDLs. However, their analysis mainly emphasized droplet deformation due to GC airflow, without further exploration of downstream phenomena such as droplet detachment or advection. In parallel, Beale *et al.* [84] developed a T-shaped GDL-GC geometry to investigate droplet behavior in more detail. Using a VOF model, they introduced a two-phase boundary condition at the GDL/MPL interface to allow gas outflow, an important physical feature that is often overlooked. However, a more detailed analysis of their study is not provided.

2.2.2 Liquid injection and initialization

These cell-scale simulations can involve liquid generation by coupling electrochemical reaction models, which mimic the real situation. However, the coupling between electrochemical reactions and interface-resolved two-phase simulations is still rare and remains challenging. One of the reasons is that decomposing the fuel cell domain for simulations typically decouples the water generation process in CLs. Hence, various simplified methods have been adopted to introduce liquid flow in these simulations. These simplified water sources, according to our investigation, include: liquid injection from holes or surfaces; water initialization within the domain, and phase change (e.g., ice melting [78], vapor condensation [79]). This section mainly focuses on studies using the former two methods, and a brief overview is shown in Fig. 2.3.

A popular approach to introducing liquid water is to inject it from the surface between adjacent components, which exhibit variability in both size and shape. These surfaces typically include the GDL/GC, GDL/MPL, and MPL/CL interfaces. Most two-phase flow simulations in GCs use either a single water inlet [60–64] or a cluster of inlets in a small region at the GDL/GC interface [65–67]. Some studies consider multiple inlets along the flow direction [68–72]. For two-phase flow simulations in a GDL or GDL/GC assembly, water injection at the GDL/MPL interface can be categorized into full-surface inlets [76, 77, 90–92] and localized inlets [73, 80, 81, 86]. It is worth mentioning that some ex-situ experiments on two-phase flow visualization also adopt localized injection [21, 32, 77, 93].

GDL two-phase flow simulations can be divided into two scenarios according to the treatment of the liquid inlet pattern: with or without employing MPL. Each scenario

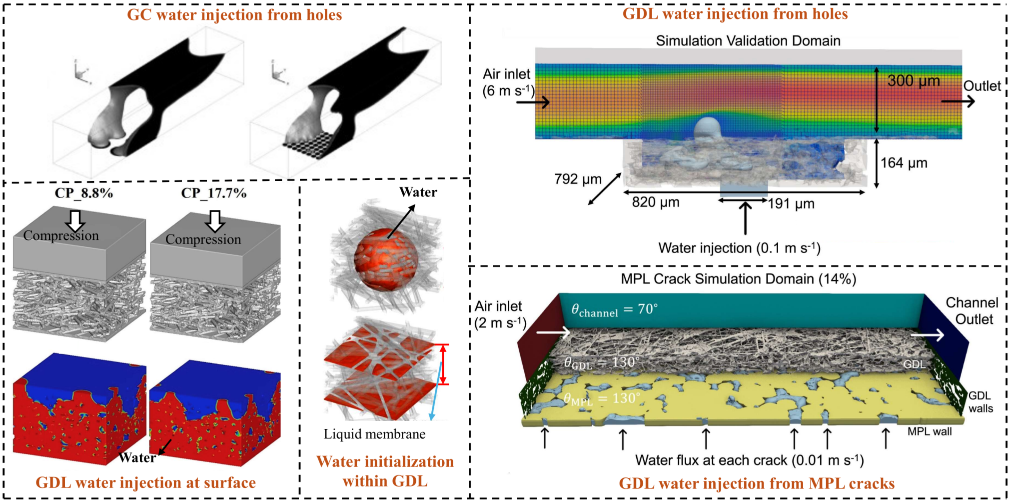

Figure 2.3: Some previous liquid water injection or initialization approaches, GC water injection from holes [65], GDL water injection from full surface [97], a hole and MPL cracks [86], as well as water initialization within GDLs [98]. Figures are adapted separately from Ding *et al.* (Journal of Power Sources, 2010) [65], Zhou *et al.* (Journal of Power Sources, 2019) [97], and Niblett *et al.* (Journal of Power Sources, 2023) [86], with permission from Elsevier, and Li *et al.* (Physics of Fluids, 2023) [98], with permission from AIP Publishing.

can then be further divided into partial injection (single or multiple holes) or full-area injection (the entire surface) of liquid, but the reason for choosing these two different injection methods is unclear yet. When the MPL structure is connected to GDL, the liquid inlet pattern in the GDL varies depending on the simulation methods used. The lattice Boltzmann method enables detailed observation of liquid flow within the MPL pores, which are smaller than those of the GDL [30, 80, 82, 83, 86, 87]. In this approach, water penetrates the MPL pore space and enters the connected GDL structure. In contrast, two-phase flow methods based on the Navier–Stokes equations, such as the VOF and level-set methods, have challenges in resolving the fine pore structure of the MPL during meshing. The typical pore size of MPLs is within the range of 20–500 nm [94]. Weber *et al.* [95, 96] experimentally observed that MPL cracks provide specific entry points into GDLs for liquid water. Thus, in some VOF simulations, only MPL large cracks are utilized as a localized water injection region. Niblett *et al.* [86] explored the effects of varying levels of cracks on water and oxygen transport using artificial microporous layer crack dilation. Similarly, Shi *et al.* [80] analyzed the influence of crack type, distance, and number on GDL water behavior under equivalent crack area conditions, while the latter two factors directly correlate with GDL water saturation. Their findings underscore the impact of differing crack areas on GDL water saturation levels due to capillary fingering, resulting in non-uniform water infiltration through MPLs. Furthermore, Yu *et al.* [81] investigated the effects of crack area, aspect ratio, width, and depth in GDLs on water behavior during the initial invasion.

Among these, GC two-phase flow simulations with water injection methods, some studies have involved the one-dimensional membrane electrode assembly electrochemical model and a species transport equation [67, 68, 99, 100] to enable the observation of the gas concentration and current density distribution. However, these methods still require liquid injection from holes. The water nucleation process is still simplified. The water inlet velocity at the holes either remains constant [99] or varies based on the gas consumption [67]. Besides, fuel cell polarization curves with large fluctuations are observed [99], which might be caused by the simplification.

In addition, some studies have initialized water within the simulated domain without adopting external inputs. These water initializations vary in different shapes (e.g., spherical and rectangular) and sizes, and locations in GC [101, 102] or GDL [98]. This approach allows for flexible analysis of water transport during gas purge under various distribution patterns, including differences in size, shape, and location [101], as well as droplet behavior under vibration [102]. Additionally, it facilitates the study of airflow rate and microstructure effects on water droplet dynamics [98].

In real PEMFC configurations, liquid water enters the channels from multiple random locations at the GC/GDL interface. The fixed inlet position and size inevitably limit the variability of two-phase flow conditions, potentially leading to occasional discrepancies. Moreover, restricting water inlets to a specific GC region may oversimplify water dynamics, omitting critical information such as water content, accumulation rate, and droplet interactions. While the effects of GC liquid inlet size and location have been studied [64, 65], the number of liquid inlets has been either overestimated [65] or underestimated [64]. Additionally, the influence of GDL liquid inlet selection has received less attention. Therefore, a deeper understanding of water behavior in GCs with multiple inlets remains essential.

2.2.3 Surface wettability

Wettability usually refers to the tendency of a liquid to spread over a solid surface, characterized by the contact angle, which quantifies the extent of wetting on the surface. Static contact angle, θ, (also called the equilibrium contact angle) is defined by Young's equation, $cos(\theta) = (\gamma_{sa} - \gamma_{sw})/\gamma_{wa}$. Where γ_{sa} and γ_{wa} are the surface tensions of solid and liquid to air, and γ_{sw} is the interfacial tension between solid and liquid. Three typical wetting behavior diagrams of water droplets in air are shown in Fig. 2.4. A surface is typically considered hydrophilic if θ is less than 90 ° and hydrophobic if θ is greater than 90 °. In addition, superhydrophilic and superhydrophobic surfaces are also defined by static contact angles less than 10 ° and greater than 150 °, respectively [103], as shown in Fig. 2.4(d-e). Some research gives a more strict definition for the superhydrophilic feature by $\theta < 5$ ° [104]. Besides, the dynamic contact angle

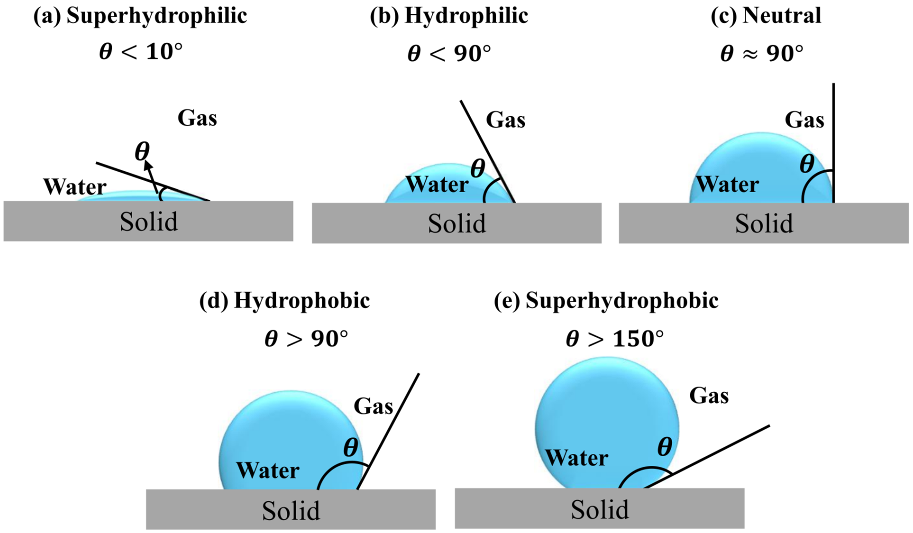

Figure 2.4: Three wetting behavior diagrams of water droplets in air. (a) Superhydrophilic surface; (b) Hydrophilic surface; (c) Neutral surface; (d) Hydrophobic surface; (e) Superhydrophobic surface.

has been proposed to study the dynamic water droplet behavior accurately. However, dynamic contact angle models are still being developed in simulations, and advancing and receding contact angles are challenging to measure in porous structures. This topic falls beyond the scope of the present thesis and will not be discussed in detail. The static contact angle has been widely used to observe the general trend of water behavior in relation to wettability variation. In the studies by Andersson *et al.* [105], the effect of the static contact angle of the GDL/GC surface on droplet detachment in GCs was explored using VOF simulations. Reasonable results were validated using experimental results from synchrotron-based X-ray radiography and tomography imaging.

Surface wettability plays a vital role in two-phase flow behavior within different components of PEMFCs. Most of the components have graphite surfaces that are inherently hydrophilic with a static contact angle of about 75-86 ° [106]. Hydrophobic agents, such as PolyTetraFluoroEthylene (PTFE), are generally coated to improve drainage. The interplay between hydrophobic and hydrophilic properties in different regions of the PEMFC determines how liquid water is distributed, accumulated, and removed, making wettability a key parameter in two-phase flow simulations.

Despite significant research efforts on GC surface wettability, no consensus has been reached on whether a hydrophobic or hydrophilic GC surface is preferential for optimal PEMFC performance and durability. Tang *et al.* [107] found that both superhydrophobic and superhydrophilic treatment of the GC surfaces were able to improve the removal of liquid water from the channel. However, fuel cell performance testing was not performed to study their effects in an operating PEMFC environment. Tao *et al.*

[108] developed a nature-inspired bionic multifunctional graphitic BPP surface consisting of a superhydrophobic coating and superhydrophilic grooves. Their experiment results showed that fuel cell peak power density was improved by 26.3% using the designed surface. Hou *et al.* [109] simulated a U-shaped GC and found that hydrophilic side walls generally hinder droplet removal due to strong adhesion. However, extreme hydrophilicity can mitigate this effect by breaking droplets into smaller ones at the bend, enhancing both removal and evaporation. Based on an assessment of water removal time and GDL surface coverage in straight channels with varying cross-sections, Liao *et al.* [110] found that different wettability properties are optimal for various geometries. A superhydrophobic GDL/GC interface is better suited for channels without curved sections, while medium hydrophobicity is more effective in configurations with corners. Subsequently, an optimal contact angle of 140 ° was proposed for both GDL and GC surfaces. Bao *et al.* [111] found that hydrophobicity in metal foam flow fields prevents flow blockage and reduces water accumulation.

Conversely, other studies have pointed to the advantages of employing hydrophilic channels. Lu *et al.* [112] demonstrated that hydrophilic GCs, compared to uncoated or slightly hydrophobic ones, promote a uniform distribution of water and gas flow and encourage film flow, which is the most desirable two-phase flow pattern in PEMFC GCs. Liu *et al.* [68] investigated the two-phase reactive transport in multiple GCs, and their results indicated that hydrophobic GC surfaces are not desirable in practice due to poor flow uniformity and low current density caused by difficult droplet detachment from the GDL. Ding *et al.* [65] conducted VOF simulations within GCs and found that hydrophilic channel walls can promote liquid droplet removal from the GDL surface. Gutierrez *et al.* [69] performed VOF simulations in a single straight channel. They proposed that combining hydrophilic channel walls with a hydrophobic GDL can balance the liquid removal rate against GDL water coverage and two-phase pressure drop. It was also found that a hydrophilic trapezoidal channel with a cross-section shape can enhance water film flow near the top of the channel wall. This result aligns with the previous experimental results [113].

To enhance the drainage capacity of porous GDL and MPL electrodes, one of the most critical steps in their fabrication process is to increase surface hydrophobicity by coating (e.g., PTFE material). A higher hydrophobicity is realized with a larger coating mass fraction. Based on lattice Boltzmann simulations in a two-dimensional GDL/MPL domain, Guo *et al.* [83] present that enhancing the GDL's hydrophobicity accelerates liquid water breakthrough and reduces overall saturation within the GDL. Increasing hydrophobicity near the GDL/MPL interface further decreases local liquid water saturation, leading to higher current density. Similar results are also observed in the VOF simulations by Zhang *et al.* [89]. A new surface wettability scheme with a more hydrophobic under-channel GDL and a less hydrophilic under-land GDL is also preferred for effective reactant gas transport. Besides, a two-dimensional lattice Boltzmann simulation by Shakerinejad *et al.* [114] suggests that inserting a hydrophilic layer near the GDL/GC interface can improve fuel cell performance. This conclusion is further confirmed by Sun *et al.* [88]. They have adopted a phase-field model, consisting of the Cahn-Hilliard and Navier-Stokes equations, to investigate the effects of contact angle on GDL water breakthrough. The results showed that when GDL hydrophilicity decreased from the CL side toward the GC, water tended to accumulate within the porous structure due to increased liquid retention. Conversely, a wettability gradient with a hydrophilic region near the GC and a hydrophobic region near the CL facilitates water transport toward the channel, enhancing liquid water removal from the GDL.

Yin *et al.* [115] conduct VOF simulations in a three-dimensional GDL domain with variable contact angles. The results indicate that in a GDL with varying contact angles, water transport characteristics at different cross-sections along the through-plane direction (along the thickness direction) resemble those in sections with fixed contact angles. Overall, the water intrusion process in a GDL with variable contact angles is similar to that in a GDL with a uniform (average) contact angle. It has been found that decreasing GDL hydrophobicity accelerates water intrusion [115]. In fact, a real GDL has mixed wettability due to coating processes, aging, or temperature effects [116], as well as drying methods (vacuum- and air-drying) [92]. By randomly changing the fraction of hydrophilic pores and throats in a GDL pore network, pore network model simulations show that the capillary pressure–water saturation curve becomes independent of the fraction of hydrophilic elements once this fraction exceeds a certain threshold [116]. Compared with a purely hydrophobic GDL, a mixed-wettability GDL has a capillary pressure–water saturation correlation curve that aligns more closely with experimental data [92].

2.2.4 Microstructure analysis

Flow fields in PEMFCs are constructed through various arrangements of GCs. Their design is essential for ensuring uniform reactant distribution, minimizing ohmic losses, improving water management, and maintaining a balanced pressure drop across the fuel cell. A wide array of flow fields have been extensively proposed and studied, including parallel [117], serpentine [118], interdigitated [119, 120], cascade [121], metal foam [111], three-dimensional fine mesh [122], porous [123], and bio-inspired [124] designs, as shown in Fig. 2.5(a). Accordingly, diverse GC geometries, such as straight, wave-like, bio-inspired, and gyroid-structured forms, have been developed. These structures also exhibit a variety of cross-sectional shapes, including trapezoidal, rectangular, and triangular profiles, as shown in Fig. 2.5(b). The impact of these geometric features on water drainage and distribution has attracted substantial attention in numerical studies.

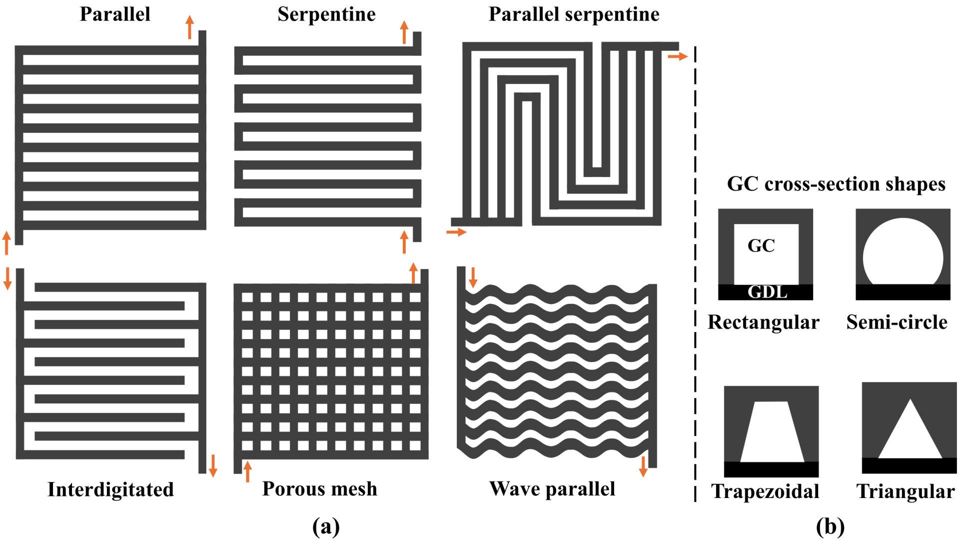

Figure 2.5: (a) Schematic diagram of the basic flow field in PEMFCs, including parallel, serpentine, parallel serpentine, interdigitated, and porous mesh flow fields. (b) Cross-sectional shapes of flow channels.

Chen *et al.* [125] substantiated the influence of the GDL/GC surface microstructure on the transport of water droplets through the application of a VOF simulation. It has been found that the oriented distribution of carbon fibers in the flow direction could facilitate the separation of droplets from the GDL surface and reduce flooding in the GC. Zhang *et al.* [72] determined that rectangular GCs achieve superior flow distribution uniformity, whereas Liu *et al.* [68] advocated for a specific type of tapered GC. Lv *et al.* [126] investigated the fluid dynamics of two-phase flow in a straight trapezoidal GC employing a lattice Boltzmann simulation. Their findings suggested that setting the opening angle of a trapezoidal flow channel to 55 ° enhances gas diffusion into the porous electrode and facilitates efficient water drainage, thereby improving overall performance. This design reduces the requisite pumping power for gas injection and mitigates the risk of liquid water blockage within the GC.

In addition, some studies have considered the roughness feature of the GDL/GC interface [127–129], as most GC two-phase flow simulations simplify it as a plane surface [68, 72, 125, 126]. It has been reported that surface roughness is significant for channels with small hydraulic diameters (0.62–1.067 mm), as the pressure drop and heat transfer can be increased with increased surface roughness [130]. A two-dimensional VOF simulation result obtained by He *et al.* [127] has shown that an increase in the triangle roughness element can help water removal for hydrophilic surfaces. Bao *et al.* [128] conducted a two-dimensional VOF model to investigate the influence of GDL/GC interface roughness on droplet detachment and removal. Their results indicate that increased surface roughness promotes the formation of a Cassie–Baxter state [131], which facilitates droplet detachment. Moreover, a higher root mean square roughness was found to significantly enhance water drainage efficiency, as illustrated in Fig. 2.6. In a related study, Yang *et al.* [129] simulated the dynamic behavior of droplets on a reconstructed fibrous GDL using an improved pseudopotential multiphase lattice Boltzmann method, which can realize thermodynamic consistency and tunable surface tension. The findings reveal that droplet inertia can drive the liquid back into the GDL structure, with stronger inertial forces resulting in deeper penetration into the porous medium.

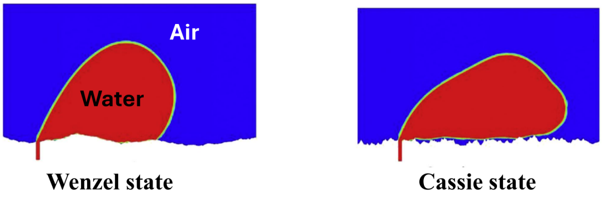

Figure 2.6: Typical Cassie[1] and Wenzel[2] states of a droplet on rough GDL surfaces. Figures are adapted from Bao *et al.* (International Journal of Hydrogen Energy, 2020) [128], with permission from Elsevier.

Many studies bypassed the consideration of the MPL and explored two-phase flow in GDL from different aspects, e.g., GDL types [132, 133], compression and deformation [74, 75], porosity [83], perforation [90], and thickness [77].

Park *et al.* [132] investigated the unsteady liquid water accumulation/removal process in carbon cloth and carbon paper GDLs using two-dimensional lattice Boltzmann simulations under a strong ambient convective flow in a porous medium. The results show that the carbon paper GDL has more dispersed water retention after water breakthrough. Aquah *et al.* [133] conducted single- and two-phase flow simulations to characterize hydraulic properties of several commercial GDLs (Toray TGP-H 060, SGL 25 BA, AvCarb 370 MGL, and a woven carbon cloth, named CeTech W1S1011) with multiple samples under different compression ratios. They found that, except for the SGL type, other GDLs show higher through-plane permeability than the in-plane one and similar end-point relative permeability. Permeability is a property of porous materials that quantifies how easily fluids (liquids or gases) can flow through them under a pressure gradient. A higher permeability corresponds to reduced resistance to fluid flow through the porous medium. In a multiple fluid system, relative permeability is a dimensionless parameter that expresses the effective permeability of a given phase relative to its value in single-phase flow.

---

[1] Cassie state: the droplet partially contacts the solid surface, resting on the roughness peaks while air pockets remain trapped in the grooves beneath.

[2] Wenzel state: the droplet fully conforms to the surface topography, penetrating into the valleys and completely wetting the rough structure.

Furthermore, to prevent gas leakage and minimize gaps between adjacent layers, a compressive force is applied to both ends of the PEMFC stack. This compression, however, induces deformation or damage to the fibrous porous structure to varying degrees. Such structural alterations significantly affect the transport properties, potentially impairing the fuel cell performance. It has been concluded that compression reduces oxygen diffusivity and intrinsic permeability while it improves thermal and electrical conductivity [74]. Further interest also combined the compression with two-phase flow transport. Chen *et al.* [75] developed a multi-physics and two-phase mixture model to investigate the variation of GDL non-uniform deformation, species transport properties, and fuel cell performance under different compression ratios. Zhou *et al.* [97] utilized the VOF method to simulate the two-phase flow inside several digitally reconstructed GDLs under various compressions. The correlations between capillary pressure and water saturation under five compression ratios are provided for future large-scale calculations. In addition, the results show a decreasing water saturation due to the decreased porosity. Apart from the bulk porosity, gradient porosity in GDLs has received much attention. Guo *et al.* [83] presented a novel pore-scale simulation in GDLs and found that increasing porosity from bottom to top is more desirable for water drainage and fuel cell performance.

In order to ensure the stability of the GDL structure, especially for carbon paper-type GDL (e.g., Toray TGP-H series), resin binder materials are usually added to the fabricated structure, and then heated, carbonized, and cooled. Subsequent thermal curing and cooling precede immersion in a hydrophobic agent (e.g., PTFE), which forms a surface coating to enhance water removal capacity. Several previous studies have studied the effect of additives, e.g., binder and PTFE, on liquid transport within additive-treated GDLs [98, 134–137]. Mo *et al.* [137] have utilized pore network simulations to study the influence of binder in a Toray TGP-H-60 GDL. Results show that the addition of binder modifies the pore structure by filling small pores, increasing large pores, and inducing a bimodal throat size distribution. This structural change alters two-phase flow regimes, shifting from viscous to capillary fingering at higher capillary numbers. Additionally, it enhances water permeability while maintaining air permeability, suggesting that optimizing binder content can help mitigate water flooding in fuel cells.

There are some explorations about optimizing the current GDL structure to get better water drainage performance. It is found that a hydrophilic perforation located in the breakthrough points can considerably reduce the liquid water level and reduce the oxygen diffusion resistance inside a GDL [90]. Niblett *et al.* [32] have performed VOF two-phase flow simulations in OpenFOAM to evaluate the water distribution in ordered and disordered two-dimensional GDLs. They found that ordered GDLs have better drainage properties. Nevertheless, fabricating these purely ordered fibrous GDLs remains challenging. Based on simulations conducted in stochastically reconstructed

GDLs using pore-scale modeling and the lattice Boltzmann method, Min *et al.* [136] demonstrated that an optimal binder content suggests that a binder content of 20% achieves a well-balanced trade-off between electrical and thermal conductivities and water drainage performance, optimizing overall GDL functionality.

2.3 Reconstruction of fibrous GDL

GDL reconstruction is necessary before conducting a numerical study on its internal water transport mechanisms. Figure 2.7 displays the three-dimensional GDL renderings of three commercialized GDL types, SGL, Toray, and Freudenberg, obtained from X-ray tomographic microscopy [138]. Distinct differences among them are highlighted, particularly regarding fiber geometry (straight vs. curved), random fiber distribution, and the presence of additive treatment. Reconstructing a GDL should involve these observed features. It seems impossible to obtain the specific shape and orientation information of each fiber inside a real GDL and then apply it to a computer-aided design procedure to draw them. Therefore, experimental (image-based) and numerical (geometry-based) methods have been investigated in recent decades.

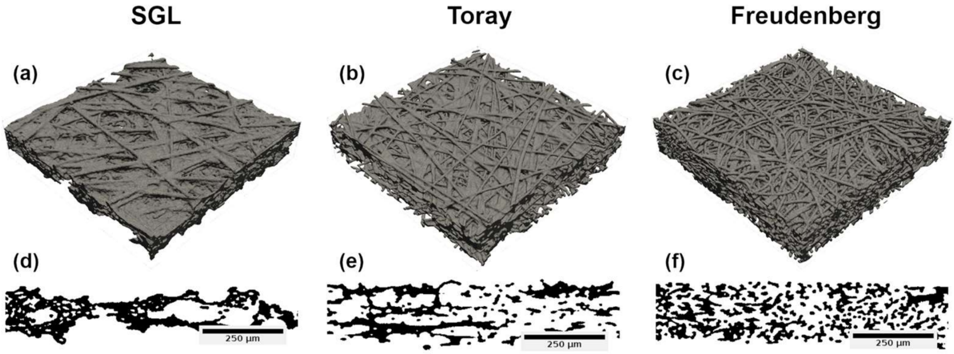

Figure 2.7: X-ray tomographic microscopy of three GDLs [138]: (a)–(c) three-dimensional renderings of the binarized dry GDL structures; (d)–(f) cross-sectional tomographic slices for each substrate, with respective image thicknesses of 136.8, 180.0, and 176.4 μm. Figures are adopted from Tranter *et al.* (Journal of The Electrochemical Society, 2020) [138], with permission from The Electrochemical Society.

Image-based reconstruction relies on an image sequence, which can be obtained by applying X-ray computed tomography or scanning electron microscopy techniques [139–143]. Subsequently, image-processing approaches are used to segment the images and reconstruct them into a three-dimensional structure. In contrast, stochastic reconstruction utilizes stochastic algorithms to generate cylindrical virtual fibers while considering real fiber diameter and length. These fibers are then stacked into three-dimensional

GDL structures according to predefined rules, incorporating key parameters such as porosity and orientation [85, 144–146].

Although image-based approaches can reconstruct the real GDL structure with high precision, it is not hard to imagine that such an approach involves expensive equipment and complex procedures. Conversely, geometry-based stochastic algorithms offer a cost-effective alternative within acceptable error tolerances [146]. Given the efficiency and flexibility of geometry-based stochastic methods, they have become increasingly popular and are adopted in a lot of research [147]. This approach enables large-scale parametric studies, such as thickness [148], compression ratio [149], fiber diameter [150], and curvature [85], and additive percentage [151, 152], while maintaining structural fidelity, making it a promising tool for advancing our understanding of water management in GDLs.

Recent studies have focused on stochastic reconstructions of straight-fiber GDLs, such as Toray-type GDLs, while research on curved-fiber GDLs, including Freudenberg-type structures, remains limited [8, 138, 143, 153]. Increasing fiber curvature within a fixed bulk porosity often reduces the fiber count, which is expected to alter pore structures and transport properties significantly. Several studies have investigated the curved-fiber GDL reconstructions by using random walk algorithms [154] and periodic surface models [155, 156]. Comparisons between the reconstructed GDLs and the reference real GDL have been conducted based on tortuosity, in-plane and through-plane permeability, and pore size distributions [150, 154]. However, while previous studies have examined the impact of fiber geometry on gas transport, liquid water transport in curved-fiber GDLs remains unexplored, and the distinction between straight-fiber and curved-fiber GDLs is not well understood, highlighting the need for further investigation. Finally, apart from the description of reconstruction algorithms for these methods, there is no published code available for use, which becomes the first barrier to be addressed at the beginning of this thesis work.

Chapter 3

Numerical methodology

The previous chapter has introduced how two-phase interactions between water and gas in PEMFCs can be modeled using different approaches, depending on the specific problem of interest. In this thesis, the VOF method is adopted to explicitly track the water-gas interface, ensuring immiscibility and enabling clear visualization of flow patterns and phase interactions. This chapter presents the significant steps of VOF simulations for GDL and GC domains, including governing equations, discretization schemes, and post-processing approaches to analyze the results.

The following assumptions are made for the simulations in this thesis:

- The liquid and gas flow within the GCs and GDLs is considered to be laminar and incompressible. This assumption is based on the relatively low Reynolds number (Re$\approx$ $666 < 1000$) and Mach number (Ma$\approx$ $0.0296 < 0.3$). These values are estimated by taking into account a group of representative two-phase properties in GCs under a temperature of 60 °C, as shown in Table 3.1.
- The simulation domain is assumed to be isothermal, thereby phase change is neglected to eliminate its potential effect on the other studied parameters, as it can introduce additional complexities and uncertainties that may interfere with the accurate analysis and understanding of the key parameters under investigation;
- The water generation process from electrochemical reactions is not considered. Instead, the liquid velocity inlet boundary condition is set directly. In addition, in our simulation, the water inlet velocity is artificially increased compared to the actual in situ liquid velocity. This strategy is commonly used to facilitate two-phase flow simulations while maintaining a similar two-phase flow pattern [65, 157].

Table 3.1: Constant two-phase properties under a temperature of 60 °C.

Parameter	Symbol	Value	Unit
Water(Liquid) density	ρ_l	983	kg/m^3
Air(Gas) density	ρ_g	1.06	kg/m^3
Water dynamic viscosity	μ_l	466×10^{-6}	Pa·s
Air dynamic viscosity	μ_g	20×10^{-6}	Pa·s
Square channel width	W	1×10^{-3}	m
Hydraulic diameter	D_h	1×10^{-3}	m
Estimated air velocity	u_g	10	m/s
Estimated water velocity	u_l	0.1	m/s
Sound speed in air	a_g	343	m/s
Sound speed in water	a_l	1480	m/s

3.1 Governing equations

In this thesis, an algebraic VOF solver, *interFoam*, implemented in the open-source software OpenFOAM v7, is applied to solve the liquid-gas two-phase flow problem in PEMFCs. The general governing conservation equations for unsteady, incompressible, Newtonian, isothermal, two-phase flow can be mathematically formulated by the following expressions.

Mass conservation equation:

$$\nabla \cdot \mathbf{u} = 0 \tag{3.1}$$

Momentum conservation equation:

$$\frac{\partial(\rho\mathbf{u})}{\partial t} + \nabla \cdot (\rho\mathbf{u}\mathbf{u}) = -\nabla p + \nabla \cdot \left[\mu\left(\nabla\mathbf{u} + (\nabla\mathbf{u})^T\right)\right] + \rho\mathbf{g} + \mathbf{f}_\sigma \tag{3.2}$$

Phase volume-fraction advection equation:

$$\frac{\partial\alpha_l}{\partial t} + \mathbf{u} \cdot \nabla\alpha_l = 0 \tag{3.3}$$

Where $\mathbf{u}$ is the velocity vector, and p, ρ, and μ represent the mixture pressure, density, and dynamic viscosity, respectively. $\mathbf{g}$ denotes gravitational acceleration. $\mathbf{f}_\sigma$ is the surface tension force. α_l is the liquid phase volume fraction, varying between 0 and 1. $\alpha_l = 1$ and $\alpha_l = 0$ signify fully liquid-filled and gas-filled cells, respectively. Volume fraction gradients exist at the phase interface. In a two-phase flow system, the gas volume fraction can be calculated by $\alpha_g = 1 - \alpha_l$. Hence, the mixture properties can be calculated as follows,

$$\begin{aligned} \rho &= \alpha_l \rho_l + \alpha_g \rho_g \\ \mu &= \alpha_l \mu_l + \alpha_g \mu_g \end{aligned} \tag{3.4}$$

Where ρ_l and ρ_g are the constant density values of the liquid and gas phases, respectively, and μ_l and μ_g denote their dynamic viscosity values. It is noteworthy that the mixture density and dynamic viscosity are spatially dependent on the fluid volume fraction. Furthermore, in the numerical solver framework, it actually reads the kinematic viscosity of each phase, i.e., ν_l and ν_g, and derives the dynamic viscosity according to $\mu = \nu\rho$.

In the *interFoam* solver, a modified pressure variable, p_{rgh}, is utilized,

$$p_{rgh} = p - \rho \mathbf{g} \cdot \mathbf{h} \tag{3.5}$$

In this formula, p refers to the static pressure. $\rho \mathbf{g} \cdot \mathbf{h}$ is the hydrostatic pressure contribution, while $\mathbf{h}$ denotes the gradient of the mesh cell centers, which equates to the tensor $\mathbf{I}$. Specifically, to obtain the pressure gradient, the gradient operator is applied to both sides of Eq. 3.5, namely,

$$\nabla p_{rgh} = \nabla p - \nabla(\rho \mathbf{g} \cdot \mathbf{h}) = \nabla p - \rho \mathbf{g} \cdot \nabla \mathbf{h} - \mathbf{h} \cdot \nabla(\rho \mathbf{g}) = \nabla p - \rho \mathbf{g} - \mathbf{g} \cdot \mathbf{h} \nabla \rho \tag{3.6}$$

Based on Eq. 3.1 and Eq. 3.6, Eq. 3.2 can be further rewritten as [158]:

$$\frac{\partial(\rho \mathbf{u})}{\partial t} + \nabla \cdot (\rho \mathbf{u}\mathbf{u}) = -\nabla p_{rgh} - \mathbf{g} \cdot \mathbf{h} \nabla \rho + \nabla \cdot (\mu \nabla \mathbf{u}) + \nabla \mathbf{u} \cdot \nabla \mu + \mathbf{f}_\sigma \tag{3.7}$$

With the use of Eq. 3.1, Eq. 3.3 can be reformulated into a conservative form as,

$$\frac{\partial \alpha_l}{\partial t} + \nabla \cdot (\alpha_l \mathbf{u}) = 0 \tag{3.8}$$

When solving Eq. 3.8, overshoots and undershoots can occur, i.e., the liquid volume fraction can lie outside the interval [0, 1]. Thus, the Multidimensional Universal Limiter with Explicit Solution (MULES) algorithm is implemented to avoid the serious numerical diffusion issues by utilizing the principles of flux correction transport. Moreover, a supplementary limiter is applied to restrict the surface flux when the variable α_l reaches the values of 0 or 1, thereby ensuring the boundedness of the equation.

The surface tension force $\mathbf{f}_\sigma$, in Eq. 3.2, refers to the continuum surface force model [159].

$$\mathbf{f}_\sigma = \sigma \kappa \nabla \alpha_l \tag{3.9}$$

Here, σ is the surface tension coefficient between water and gas, which is 0.0644 N/m. κ denotes the mean curvature of the interface. κ can be calculated by,

$$\kappa = -\nabla \cdot \hat{n}_c \tag{3.10}$$

$\hat{n}_c$ is a unit vector normal to the liquid-gas interface, which is calculated from the fluid fraction field,

$$\hat{n}_c = \frac{\nabla \alpha_l}{|\nabla \alpha_l|} \tag{3.11}$$

In addition, the interaction between the fluids and the solid surface (wall adhesion) is included as a boundary condition on the surface normal vector at the solid wall.

$$\hat{n}_c = \hat{n}_s \cos\theta + \hat{t}_s \sin\theta \tag{3.12}$$

Where $\hat{n}_s$ and $\hat{t}_s$ are the unit vectors normal and tangential to the solid boundary, respectively; θ is the equilibrium or static contact angle. The surface normal vector is corrected at the contact line to satisfy the specified static contact angle boundary condition. Linear interpolation is utilized to interpolate the cell values to obtain the cell face values.

3.2 Numerical scheme and solver

In the OpenFOAM framework, the finite volume method is used to discretize the above equations 3.1, 3.7, and 3.8 into discrete equations based on the cell-centered values. Specific discretization schemes are employed for temporal and spatial terms, providing mixed first-order and second-order accuracy while considering the trade-off between optimal computational speed and simulation accuracy. Both temporal and spatial integration are applied to both sides of the three equations. The Gauss theorem is employed to convert volume integrals into surface integrals [160]. Firstly, the transient terms are discretized using an implicit *Euler* scheme with first-order accuracy. It is robust and computationally cost-effective for the relatively small time steps (with the simulation time step on the order of 10^{-8} s). Secondly, the convection and diffusion terms in the momentum conservation equation will be implicitly expressed by the face-centered fluxes. To close the discretization, both convective and diffusive fluxes must be reconstructed from the cell-centered values based on various interpolation schemes. In this thesis, the convective and diffusive fluxes are separately reconstructed based on the *linearUpwind grad(U)* and *linear* schemes, both with second-order accuracy. In addition, there is an implicitly treated convection flux in the integrated fluid advection equation. Generally, high-order interpolations can lead to nonphysical oscillations, especially near discontinuities of the volume fraction. Thus, a bounded total variation diminishing scheme with the *vanLeer* limiter is utilized within the Multidimensional Universal Limiter for Explicit Solution (MULES) framework. This method ensures boundedness and numerical stability while retaining second-order accuracy in smooth regions. Next, point-to-point *linear* interpolation is used for the velocities on the mesh cell surfaces.

In addition, the PIMPLE algorithm [161] implemented in OpenFOAM is used to solve the velocity-pressure coupled discrete equations. It represents a hybrid integration of the Semi-Implicit Method of Pressure-Linked Equations (SIMPLE) and Pressure-Implicit with Split Operator (PISO) algorithms, merging the stability characteristics intrinsic to SIMPLE with the accuracy offered by PISO. This algorithm consists of an outer loop devoted to resolving the momentum equation for the prediction of velocity. Subsequently, an inner loop is employed to solve the Poisson pressure equation, enabling the derivation of pressure and the subsequent correction of the velocity field accordingly. In this study, after a thorough assessment of mesh quality, computational efficiency, and stability, a strategy comprising one outer PIMPLE loop and three inner loops is adopted, which resembles PISO. This setting is based on the constraint of the Courant number. An adjustable time option is activated to generate the new time step by constraining the Courant number to always be less than 0.5. Only Paper II adopts the non-orthogonal correction due to the introduction of skewed mesh cells. In other papers, the non-orthogonal correction is not applied, given the dominance of the structured orthogonal hexahedral mesh.

The following semi-discretized equations are obtained using the finite volume method based on the Gauss theorem.

$$\sum_f \mathbf{u}_f^{n+1} \cdot \mathbf{S}_f = 0 \tag{3.13}$$

$$V_P \frac{\alpha_{l,P}^{n+1} - \alpha_{l,P}^{n}}{\Delta t} + \sum_f \alpha_{l,f}^{n+1}\, \phi_f^n = 0 \tag{3.14}$$

$$\begin{aligned} V_P \frac{\rho_P^{n+1}\mathbf{u}_P^{n+1} - (\rho\mathbf{u})_P^n}{\Delta t} &+ \sum_f (\rho_f \phi_f)^n \mathbf{u}_f^{n+1} - \sum_f \mu_f^{n+1} (\nabla \mathbf{u})_f^{n+1} \cdot \mathbf{S}_f \\ &= \int_V (-\nabla p_{rgh} - \mathbf{g} \cdot \mathbf{h} \nabla \rho + \mathbf{f}_\sigma) dV + \nabla \mathbf{u}_P^n \cdot \nabla \mu_P^{n+1} V_P \end{aligned} \tag{3.15}$$

where $\Delta t = t^{n+1} - t^n$. $\mathbf{S}_f$ is an outward face normal vector whose magnitude is the area of the cell face, f. The superscripts n and $n+1$ represent the current and next time steps, respectively. The subscript P denotes the "owner" cell, and N will be used to represent the "neighbor" cells sharing the given face f. V_P is the volume of the P mesh cell. The volumetric flux through face f at time level n is defined as $\phi_f^n = \mathbf{u}_f^n \cdot \mathbf{S}_f$. The choice of the cell center value at the old and new time depends on the implicit and explicit treatment of each term. This is determined by the use of `fvm::` (finite volume matrix) and `fvc::` (finite volume calculus) operators in OpenFOAM [1]. $\mathbf{u}_f^{n+1}$, μ_f^{n+1}, ρ_f^{n+1} are face-centered fields that need further interpolation operations.

The following illustrates the solution process for the semi-discretized equations presented above.

(1). Field initialization.

All face and cell fields are initialized from boundary conditions, including p_{rgh}^0, $\mathbf{u}^0$, α_l^0, and their face values $p_{rgh,f}^0$, $\mathbf{u}_f^0$, $\alpha_{l,f}^0$, with explicit bounding by $\min(\max(\alpha_l, 0), 1)$ and $\min(\max(\alpha_{l,f}, 0), 1)$. The pressure p^0 is updated via Eq. 3.5, while mixture properties μ^0, μ_f^0, ρ^0, and ρ_f^0 are computed using Eq. 3.4. Interpolations then yield the initial face values and fluxes: $p_{rgh,f}^0$, $\mathbf{u}_f^0$, α_f^0, ϕ_f^0, and $(\rho_f\phi_f)^0$.

(2). Transient solver iteration from t^n to t^{n+1}

(2.1). Time step calculation.

After completing the iterations at each time step, n, an adjustable time step strategy is employed to calculate $(\Delta t)^{n+1}$ automatically. The actual maximum Courant number Co_{max}^n is calculated as,

$$Co_{max}^n = \frac{1}{2}\max_i\left(\frac{(|\sum_f \phi_f^n|_i)}{V_i}(\Delta t)^n\right) \tag{3.16}$$

where i is the cell label. Then a damping factor is calculated,

$$\tau_{\Delta t}^n = \frac{Co_{max,fixed}}{Co_{max}^n + 10^{-6}} \tag{3.17}$$

The new time step $(\Delta t)^{n+1}$ will be,

$$(\Delta t)^{n+1} = \min\Big(\min\{\tau_{\Delta t}^n,\ 1 + 0.1\,\tau_{\Delta t}^n,\ 1.2\}\,(\Delta t)^n,\ (\Delta t)_{\max}\Big) \tag{3.18}$$

This thesis always ensures $Co_{max,fixed} = 0.5$, and $(\Delta t)_{max} = 10^{-5}$ s.

(2.2). Solving volume fraction α_l^{n+1} and updating mixture properties.

Addressing Eq. 3.14 within one overall sub-cycle by the following procedure. First, the preliminary flux $(\alpha_{l,f})^{n+1,\text{upwind}}\phi_f^n$ is constructed using an *upwind* scheme. Next, the

---

[1] Terms treated by `fvm::` are added to the coefficient matrix using unknowns at the new time level, whereas `fvc::` terms are evaluated from known field values and placed in the right-hand side of the equation.

interface sharpening and boundedness are achieved via the MULES algorithm, combined with a *vanLeer* flux limiter, and two correction iterations are performed to compute an updated flux $(\alpha_{l,f})^{n+1,\star}\phi_f^n$. Before each correction step, the difference between the current and previous fluxes is evaluated and used as an input to guide the limiting process. After the iteration, α_l^{n+1} is solved. The mixture properties, like ρ_f^{n+1}, μ_f^{n+1}, and interface properties, like $\sigma\kappa_f^{n+1}\nabla\alpha_{l,f}^{n+1}$, κ_f^{n+1}, and $(\hat{n}_c)_f^{n+1}$, are subsequently updated. The final $(\alpha_{l,f})^{n+1}\phi_f^n$ is calculated with $(\alpha_{l,f})^{n+1}\phi_f^n)(\rho_{l,f}^{n+1} - \rho_{g,f}^{n+1}) + \phi_f^n\rho_{g,f}^{n+1}$.

(2.3). Momentum prediction.

Employing Eq. 3.15 to formulate a momentum matrix while disregarding the pressure gradient, hydrostatic pressure, and surface tension force, and substituting the face value with the approximation mentioned above. An explicit expression for the predicted velocity field $\mathbf{u}_P^r$ is obtained, as follows,

$$\begin{aligned}\rho_P^{n+1}V_P\frac{\mathbf{u}_P^r}{\Delta t} - \rho_P^n V_P\frac{\mathbf{u}_P^n}{\Delta t} + \sum_f(\rho_f\phi_f)^n\mathbf{u}_f^r - \sum_f \mu_f^{n+1}(\nabla_f^\perp\mathbf{u})^r \cdot |\mathbf{S}_f| + \\ \nabla\mathbf{u}_P^n \cdot \nabla\mu_P^{n+1}V_P = 0\end{aligned} \tag{3.19}$$

where $\nabla_f^\perp$ is the surface-normal gradient operator, e.g., $(\nabla\mathbf{u})_f^r \cdot \mathbf{S}_f = \nabla_f^\perp(\mathbf{u})^r|\mathbf{S}_f|$.

Applying the various interpolations to Eq. 3.19 yields the following expression,

$$a_P\mathbf{u}_P^r + \sum a_N\mathbf{u}_N^r = S_P^n \tag{3.20}$$

Carrying out the momentum prediction using the old pressure data,

$$\begin{aligned}\mathbf{u}_P^* = \frac{1}{a_P}(-\sum a_N\mathbf{u}_N^r + S_P^n) \\ -\frac{1}{a_P}\sum_f\left(-(\nabla_f^\perp p_{rgh})^n - \mathbf{g}\cdot\mathbf{h}\nabla_f^\perp\rho^{n+1} + \sigma\kappa_f^{n+1}\nabla_f^\perp\alpha_l^{n+1}\right)|\mathbf{S}_f|\end{aligned} \tag{3.21}$$

(2.4). PISO loop for pressure prediction and correction, as well as velocity correction.

Defining the following terms based on Eq. 3.20.

$$rAU = \frac{1}{a_P}, \mathbf{HbyA}_P^* = (rAU)(-\sum_f a_N\mathbf{u}_N^{r,*} + S_p^n) \tag{3.22}$$

Calculating the flux, $\phi_f^{\mathbf{HbyA}^*}$, and updating it with the surface tension and hydrostatic pressure term,

$$\phi_f^{\mathbf{HbyA}^{**}} = \phi_f^{\mathbf{HbyA}^*} + rAU_f\left(\sigma\kappa_f^{n+1}\nabla_f^\perp\alpha_l{}^{n+1} - \mathbf{g}\cdot\mathbf{h}(\nabla_f^\perp\rho^{n+1})\right)|\mathbf{S}_f| \tag{3.23}$$

Considering the pressure contribution, we have the new mass flux,

$$\phi_f^* = \phi_f^{\mathbf{HbyA}^{**}} - rAU_f(\nabla_f^{\perp} p_{rgh}^*)|\mathbf{S}_f| \tag{3.24}$$

Based on Eq. 3.13, we have $\sum_f \phi_f^* = 0$, thus, the pressure-Poisson equation is derived,

$$\sum_f (rAU_f(\nabla_f^{\perp} p_{rgh}^*))|\mathbf{S}_f| = \sum_f \phi_f^{\mathbf{HbyA}^{**}} \tag{3.25}$$

The pressure $p_{rgh,P}^*$ is obtained by solving the above equation based on interpolated fields. The velocity $\mathbf{u}^{**}$ is then corrected based on $p_{rgh,P}^*$, following a similar procedure as in Eq. 3.21. If PISO iterations are incomplete, step 2.4 is revisited to continue the cycle. Upon convergence, $p_{rgh,P}^{n+1}$, $\mathbf{u}_P^{n+1}$, and ϕ_f^{n+1} are obtained, and the updated pressure p^{n+1} is computed. The loop restarts from step (2) until the end time is reached, after which the simulation terminates.

3.3 Boundary conditions

During the solution of the aforementioned equations, boundary conditions play a crucial role in imposing constraints on the variables at the boundary surface of the simulation domain. The purpose is to ensure that the problem is well-posed and that the physical behavior is accurately represented. The boundary conditions used for the different cases in this thesis are presented in the tables below. Table 3.2 and Table 3.3 display the main boundary conditions for two-phase flow simulations within single straight GCs (Paper I) and T-shaped GC and GDL assemblies (Paper II, III, IV, V), respectively. Table 3.4 further shows the liquid water inlet velocity under different conditions in Paper IV. Note that all boundary condition names are from OpenFOAM. As we have discussed in the section 2.2.3, the surface wettability is determined by applying a contact angle, θ. This thesis employs the static contact angle strategy, which remains a widely used approach in previous VOF simulations, yielding reasonable results compared to experiments [32, 64, 74, 89, 92, 105].

It should be mentioned that the liquid inlet velocity has been accelerated compared to that in actual operation, around 2×10^{-5} m/s [32, 162]. It can be roughly calculated that if such a physical GDL liquid invasion velocity is adopted, it will take several months just to simulate the liquid breakthrough. Fortunately, it was found that scaling up the liquid velocity makes a minor change to the GDL capillary fingering dominated flow type and dramatically accelerates the simulation to observe longer water behavior [163]. The feasibility of such an acceleration method has also been proved by comparing numerical and experimental results [32, 92, 105]. In previous studies, GDL liquid inlet velocity values of 0.054 m/s [41] and 0.1 m/s [32, 164] were utilized. In this thesis, liquid water is input into a single straight channel with a velocity of 0.1 m/s, due to the relatively long-time simulation requirement, 108 ms. For two-phase flow simulations in T-shaped GC and GDL assemblies, the liquid velocity is mainly set at 0.02 m/s. However, to study the effect of liquid inlet/gas outlet conditions, a constant water inlet mass flow rate, $\dot{m}$, which is calculated by Eq. 3.26, is utilized for all liquid injection configurations. ρ and A are the liquid density and cross-sectional injection area. Correspondingly, various liquid input velocity values are obtained, as shown in Table 3.4.

$$\mathbf{u}_{l,in} = \frac{\dot{m}}{\rho A} \tag{3.26}$$

Table 3.2: Boundary conditions for straight GCs in Paper I.

Boundaries	Volume fraction, α_l	Velocity, $\mathbf{u}$(m/s)	Pressure, p_{rgh}(Pa)
GC inlet	0	(0, 10, 0)	fixedFluxPressure
GC Outlet	zeroGradient	zeroGradient	totalPressure
GC side walls	$\theta = 30/90/150°$	noSlip	fixedFluxPressure
GC top walls	$\theta = 30/90/150°$	noSlip	fixedFluxPressure
GC/GDL interface	$\theta = 145°$	noSlip	fixedFluxPressure
GC water injection	1	(0, 0, 0.1)	fixedFluxPressure
Water injection sides	$\theta = 145°$	noSlip	fixedFluxPressure

Table 3.3: Boundary conditions for T-shaped GC and GDL assemblies in Papers II, III, IV, V.

Boundaries	Volume fraction, α_l	Velocity, $\mathbf{u}$(m/s)	Pressure, p_{rgh}(Pa)
GC inlet	0	(0, 10, 0)	fixedFluxPressure
GC Outlet	zeroGradient	zeroGradient	totalPressure
GC side walls	$\theta = 45°$	noSlip	fixedFluxPressure
GC top walls	$\theta = 45°$	noSlip	fixedFluxPressure
GC/GDL interface	$\theta = 150°$	noSlip	fixedFluxPressure
GDL surface	$\theta = 150°$	noSlip	fixedFluxPressure
GDL side surfaces	symmetry	symmetry	symmetry
GDL water injection	1	(0, 0, 0.02)	fixedFluxPressure

Table 3.4: Liquid injection velocity utilized for studying the GDL liquid inlet/gas outlet in Paper IV.

GDL water injection type	Velocity value	Unit
Type A	(0 0 0.02)	m/s
Type B	(0 0 0.5)	m/s
Type C	(0 0 0.1)	m/s
Type D	(0 0 0.1)	m/s
Type E	(0 0 0.1)	m/s
Type F	(0 0 0.5)	m/s

3.4 Mesh generation

Mesh generation is fundamental in the OpenFOAM simulations, as it provides the spatial framework for solving discretized governing equations. Both cell volume and face information, such as surface normal vectors and interpolation weights, play a crucial role in ensuring accurate flux calculations and maintaining numerical stability. A well-constructed mesh has a direct influence on solution accuracy, convergence behavior, and computational efficiency. Various mesh strategies have been developed for selection, e.g., structured, unstructured, and hybrid meshes. A critical mesh quality metric, including skewness, aspect ratio, and non-orthogonality, should be considered to enhance both simulation accuracy and computational efficiency.

When it comes to the simulations for GDL and GC of PEMFCs, a regular square GC geometry can be efficiently meshed using a structured grid; however, the fibrous GDL structure presents significant meshing challenges due to two factors as follows:

1. **Multi-scale pore structure**: The GDL exhibits a broad distribution of pore sizes, ranging from approximately 4 μm to 100 μm. Accurately resolving both large and small pores necessitates varying mesh resolutions. Fine grids are required to capture small pores, which drastically increases the total mesh cells and, consequently, the computational cost.
2. **High-curvature and sharp surface features**: The cylindrical fibers in the GDL form intricate structures, with some regions featuring sharp intersections that create highly irregular pore geometries characterized by steep curvatures and acute angles. These geometric features complicate mesh generation and increase the likelihood of producing highly distorted cells, particularly during the refinement process.

This combination of multi-scale and high-curvature geometries makes meshing the GDL a challenging task, necessitating effective meshing strategies to strike a balance between accuracy and computational efficiency.

Meshing such complex GDL structures mainly relies on the automatic generation and iterative optimization of an unstructured mesh. Additionally, having access to more adjustable parameters can provide better control over the mesh generation process and its results. The *SnappyHexMesh* utility in the open-source software OpenFOAM offers this possibility. *SnappyHexMesh* operates on the principle of successive refinement and snapping to approximate complex geometries while generating a predominantly hexahedral mesh. The core algorithm follows a multi-step approach that transforms a simple initial background mesh into a conformal mesh that closely matches the geometry of interest. The mesh generation process is illustrated in Fig. 3.1, based on a representative porous domain. Castellated mesh generation begins with a uniform hexahedral background mesh, refining it locally near the geometry by subdividing cells that intersect the geometry surface. It typically requires another hexahedral structured mesh utility *blockMesh*. This process yields a blocky mesh structure, with cells that roughly approximate the target geometry. Snapping enhances mesh conformity by adjusting vertices to the precise surface, guided by surface normals to ensure alignment and non-penetration constraints, thereby maintaining mesh quality.

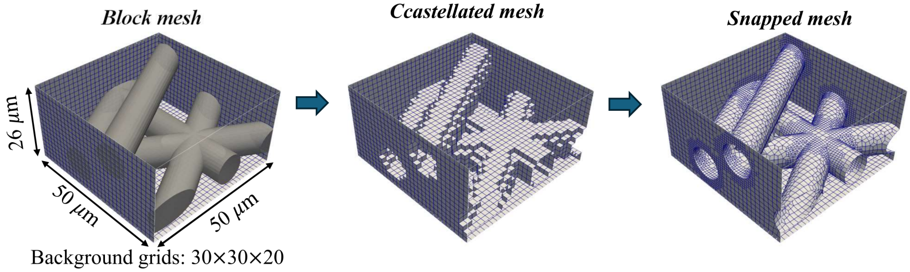

Figure 3.1: Illustration of the meshing process utilizing the *SnappyHexMesh* utility within OpenFOAM. To enhance visualization clarity, the internal mesh is omitted, and several meshed patches are instead demonstrated.

Mesh quality assessment is included in *SnappyHexMesh*, including metrics such as aspect ratio, skewness, and non-orthogonality [161]. In this investigation, the maximum allowable non-orthogonality is constrained to be below 80 °, while the maximum permissible internal and boundary skewness is constrained to be below 4 and 20, respectively. Additionally, the maximum aspect ratio is maintained below 5. However, it has been noted that regardless of the grid or surface refinement level of the castellated mesh, the snapped mesh consistently fails to meet these key mesh quality criteria. Furthermore, during the mesh snapping process, a larger number of small, irregular tetrahedral cells are generated, particularly when surface refinement is employed. This leads to challenges in controlling the minimum mesh resolution, subsequently resulting in extended computational time at a constant Courant number.

While checking the mesh quality, problematic cells have been identified and stored in a separate directory. Thus, the manual removal of defective mesh cells has been attempted. Nevertheless, it has been observed that, without additional vertex manipulation, achieving high mesh quality remains challenging with snapped meshes. Consequently, a castellated mesh with sufficiently refined grids is employed in the VOF simulations to ensure a high-quality mesh, albeit at the expense of altering the surface topology of the porous structure, particularly regarding the surface of the cylindrical fibers. This strategy has also been adopted in some previous studies analyzing three-dimensional GDLs [79, 92, 165].

3.5 Post-processing methods

Numerical two-phase flow studies enable detailed observation and analysis of water distribution patterns, offering greater flexibility, improved resolution, and comprehensive information compared to experiments. These simulations allow investigations from various perspectives, including different temporal moments, viewing angles, spatial locations, and dimensional scales, facilitating an in-depth understanding of flow dynamics that would be challenging to obtain experimentally. Both qualitative and quantitative analyses have been performed to evaluate the simulation results above, utilizing Paraview and MATLAB software, as well as in-house Python codes. The two-phase flow behavior has been analyzed from the following perspectives.

Post-processing error effects

Considering the diffusion of the interface in the VOF simulations, most of the following analyses are carried out based on a scalar threshold of $\alpha_l = 0.5$. This value has been widely adopted to distinguish between the two phases [86, 166, 167]. Additionally, this value was also selected for the reconstruction of the interface during the development of the VOF method [168]. We must admit that some uncertainty errors may be induced by the selection of this value (as the interface is diffusive) or by the functions in the post-processing software, such as point interpolation. However, since this study does not aim to replicate real-world two-phase flow scenarios precisely, but rather to investigate the underlying transport dynamics, such as flow patterns, all quantitative analyses presented herein primarily serve to elucidate the trends and variations arising from different parameters under consistent conditions. It is hypothesized that the selection of the isosurface value of α will merely affect the magnitudes, but not the trend.

Water distribution

In the ParaView software, the water distribution has been analyzed based on the scalar field, α_l. The *Slice* function generates a two-dimensional visualization of the water distribution in any chosen plane, using built-in interpolation functions to smoothly represent the data stored initially in cell centers. A three-dimensional representation of the water distribution is obtained by either clipping the α_l field at an isovalue of $\alpha_l = 0.5$ or extracting the corresponding isosurface ($\alpha_l = 0.5$) using the *Contour* function.

Water saturation

To quantify the water volume fraction in the GDL and GC domain over time, a quantity called total water saturation, S_Ω (Ω = GDL, GC), is calculated,

$$S_\Omega = \frac{V_{w,\Omega}}{V_{p,\Omega}} \tag{3.27}$$

$V_{w,\Omega}$ and $V_{p,\Omega}$ are the water phase volume and pore volume in the corresponding Ω region.

The water fraction within the plane is quantified by the local water saturation S_l of the GDL.

$$S_l = \frac{A_{w,S}}{A_{p,S}} \tag{3.28}$$

A_w and A_p are the water area and pore area in any plane.

Water coverage ratio

The water coverage ratio is frequently used as a parameter to evaluate water behavior within the GC. It effectively characterizes both water flow patterns and breakthrough conditions. For instance, a high water coverage ratio on a given surface typically indicates a large amount of water attached to this surface. Furthermore, a sustained high water coverage ratio suggests a predominant water flow pathway along that surface. Specifically, when this phenomenon occurs at the GDL/GC interface, it implies a reduction in the available diffusion area for reactant gases due to blockage by water. The calculation is similar to Eq. 3.28 while the plane is the GC surface.

Pressure drop

The pressure drop of the gas phase in the GC is calculated simply by the difference between the average pressure at the channel input and outlet.

$$P_{GC} = P_{in,GC} - P_{out,GC} = \frac{\sum_{i=1}^{n} P_{in,i} A_i}{\sum_{i=1}^{n} A_i} - \frac{\sum_{i=1}^{m} P_{out,j} A_j}{\sum_{j=1}^{m} A_j} \tag{3.29}$$

$P_{in,GC}$ and $P_{out,GC}$ are the area-averaged pressure at GC inlet and outlet. m and n are the number of mesh cells in those two patches. This method has been adopted in other VOF simulation studies in PEMFC channels [72].

Capillary pressure

Capillary pressure, P_c, is the pressure difference between the two phases at the interface, which is considerably related to the evolution of the GDL capillary fingering flow of water [169, 170] due to the small number of capillaries ($Ca = \mu U/\sigma$). In addition, the Young-Laplace equation is also widely used to estimate capillary pressure, defined by $P_c = 2\sigma cos(\theta)/R$, where R is the effective mean radius of the pores. Different approaches to obtaining this parameter have been reviewed in Paper IV. The capillary pressure is approximated by the area-weighted average pressure at the isosurface of $\alpha = 0.5$. Compared to the other methods, the values calculated by this method are closer to the experimental and numerical results in the GDL, varying approximately from 3300 Pa to 6500 Pa [32, 96, 170–172].

Relative thickness

Relative thickness usually refers to a dimensionless parameter used to characterize the thickness at a specific plane location relative to the GDL thickness.

Statistically stable state

In the following discussion, a statistically stabilized state refers to a condition in which instantaneous properties, such as water volume fraction and gas pressure, become stable, allowing small fluctuations in a certain range [173].

Chapter 4

Stochastic reconstruction of fibrous GDL

To obtain the GDL structure for simulations, a geometry-based GDL reconstruction approach is developed, which includes two common steps: single-fiber structure generation and multiple-fiber stacking in a specific domain, and additive structure (i.e., binder and PTFE) generation for some types of GDL. The following reasonable assumptions have been made,

1. Each carbon fiber is represented by a straight or curved cylinder with a random length. All cylinders in a GDL have the same diameter.
2. Each cylinder is first randomly placed toward an arbitrary in-plane direction following a uniform distribution function. Then the through-plane orientation can be adjusted based on a Gaussian distribution function.
3. All cylinders are allowed to partially overlap each other as it makes less impact on the pore, especially under high porosity conditions [174]. Note that it may not be possible to ignore fiber overlapping when analyzing compression, as it changes the contact area between the cylinders.
4. The additive structure includes both PTFE and binder components, and mainly accumulates at the fiber intersection regions [165, 175].

4.1 Fiber generation

Two methods have been developed to reconstruct carbon fibers using in-house MATLAB codes. Initially, a method based on the generating function of a straight cylinder was developed specifically for straight fibers. The fundamental concept is that the coordinates of any two points in a three-dimensional Cartesian coordinate system can define a linear central axis of a cylinder. Then, based on this centerline of the cylinder and the specified cylinder diameter, a series of coordinates of points located on the side surface can be calculated. Finally, these discrete points are formed into a cylindrical mesh surface using the *surf* function.

However, some commercialized GDLs, such as the Freudenberg H23 series, contain carbon fibers with noticeable curvature. Previous studies have primarily focused on straight-fiber GDLs, usually referencing Toray-based GDLs. Reconstruction methods for curved-fiber structures remain limited in the literature. To address this gap, a new methodology was developed to generate curved cylindrical fibers. The approach builds upon the straight-fiber generation technique, where a space curve is defined as the central axis (or skeleton). A surface at a constant radial distance from the axis is constructed to form the fiber geometry. This concept aligns with the rod periodic surface model proposed by Wang [156], which was adopted here as a foundation for implementing a generator capable of producing both straight and curved fibers. The mathematical formulation of the periodic surface model is presented below,

$$\begin{aligned} f(\mathbf{r}) = 4cos(2\pi(\mathbf{RT}P_1)^T\mathbf{r} + bcos(2\pi f_r(\mathbf{RT}Q_1)^T\mathbf{r})) + 4cos(2\pi(\mathbf{RT}P_2)^T\mathbf{r})+ \\ 4cos(2\pi(\mathbf{RT}P_2)^T\mathbf{r}) + 3cos(2\pi(\mathbf{RT}P_3)^T\mathbf{r}) - 4cos(\pi(1-S_r)) + 1 \end{aligned} \tag{4.1}$$

Here, $f(\mathbf{r})$ represents the rod periodic surface model. The vector $\mathbf{r} = [x, y, z, 1]$, where $[x, y, z]$ is the location vector within the unit space $\mathbb{R}^3 \in [0,1]^3$. Thus, it can be seen that the structure generated by the periodic surface model is dimensionless and confined within a cubic domain with x, y, $z \in [0,1]$. Therefore, a parameter S_r is utilized for subsequent full-dimensional scaling. S_r signifies the ratio between the desired fiber diameter, d, and the largest dimension, D, of the expected GDL domain.

Matrices $[P_1, P_2, P_3, P_4]$ and Q_1 represent fiber spatial orientation and bending direction, respectively. Vectors $\mathbf{R} = [R_1, R_2, R_3, R_4]$ and $\mathbf{T} = [T_1, T_2, T_3, T_4]$ are translation and rotation matrices. Detailed descriptions are provided in Eq. 4.2. Thus, $\mathbf{R}$ and $\mathbf{T}$ are functions of (φ, θ, w) and (t_1, t_2, t_3), respectively. φ, θ, and w are the axis rotation angles aligned with the x, y, and z axes. t_1, t_2, and t_3 are translation scalars aligned with the x-y, y-z, and x-z planes. Moreover, b and f_r are used to control the magnitude of fiber curvature and wave frequency, respectively.

$$\begin{aligned}
R_1 &= [cos(\theta)cos(w) - sin(\theta)sin(\varphi)sin(w), cos(\theta)sin(w) \\
&\quad + cos(w)sin(\varphi)sin(\theta), -cos(\varphi)sin(\theta), 0]^T \\
R_2 &= [-cos(\varphi)sin(w), cos(\varphi)cos(w), sin(\varphi), 0]^T \\
R_3 &= [cos(w)sin(\theta) + cos(\theta)sin(\varphi)sin(w), \\
&\quad sin(\theta)sin(w) - cos(\theta)cos(w)sin(\varphi), 0]^T \\
R_4 &= [0, 0, 0, 1]^T \\
T_1 &= [1, 0, 0, -t_1]^T, T_2 = [0, 1, 0, -t_2]^T \\
T_3 &= [0, 0, 1, -t_3]^T, T_4 = [0, 0, 0, 1]^T
\end{aligned} \tag{4.2}$$

To incorporate the characteristic of fiber anisotropy, the generated fibers are adjusted towards a through-plane orientation. The probability distribution function, $P(\theta)$, proposed by Stoyan *et al.* [176] is adopted and combined with Eq. 4.1 to regulate the likelihood of the rotation angle θ, as shown below,

$$P(\theta) = \frac{1}{2}\frac{\beta cos(\theta)}{(1 + (\beta^2 - 1)sin^2\theta)^(3/2)} \tag{4.3}$$

Here, β is referred to as the anisotropy parameter. When $\beta = 0$, it indicates that all the carbon fibers are parallel to the through-plane direction. As β increases, a larger fraction of fibers are aligned along the in-plane direction. Key parameters and their respective value (range) in the above model have been given in Table 4.1.

Table 4.1: Key parameters used in the periodic surface model.

Parameters	Value/range
φ	0
θ	[-π/2,π/2]
w	[-π,π]
t_1	[0,1]
t_2	[0,1]
t_3	[-0.491,-0.216]
b	[0,0.6]
f	[0,2.7]
$[P_1, P_2, P_3, Q_1]$	[[0,1,0,0]^T,[0,0,1,0]^T,[0,0,0,0]^T,[1,0,0,0]^T]

It is necessary to clarify that Paper II utilized the straight cylinder generation method, and Papers III and V utilized the periodic surface model for both straight and curved fiber generation. Stochastic GDLs are not used in Paper IV; instead, it adopts an image-based GDL sample.

4.2 Fiber stacking strategy

Following the digital generation of fibers, the next step is to stack a series of straight or curved cylindrical fibers within a specified domain. This procedure mimics the free sedimentation process in producing GDLs, where the cut carbon fibers are sequentially dropped into a particular solution. In the actual process, the random distribution, which is usually achieved through stirring, is achieved by randomly adjusting the orientation of the fibers in our reconstruction. Two distinct stacking strategies, namely random stacking and layer-by-layer stacking, are utilized in this thesis.

Figure 4.1 shows the random stacking strategy based on the stochastic translation of each generated fiber in the given domain. Target porosity $P_{bulk,goal}$, fiber diameter, and bulk porosity tolerance, $\epsilon = 1.5\%$, are provided. At the beginning, the real bulk porosity P_{bulk} is initialized to 1, as there are no solid fibers in the given domain, which will decrease as fibers are generated. Upon the translation of the x_{th} fiber, the proportion of its occupied volume ϕ_x within the defined region is calculated. The actual bulk porosity will be updated with $P_{bulk,new} = P_{bulk,old} - \phi_x$. This iterative process continues until the discrepancy between P_{bulk} and $P_{bulk,goal}$ is minimized to fall within an acceptable tolerance range ϵ. This methodology has been widely applied in prior GDL reconstructions [74, 97, 155, 177]. Paper II utilizes this strategy, and the resulting reconstruction is shown in Fig. 4.2.

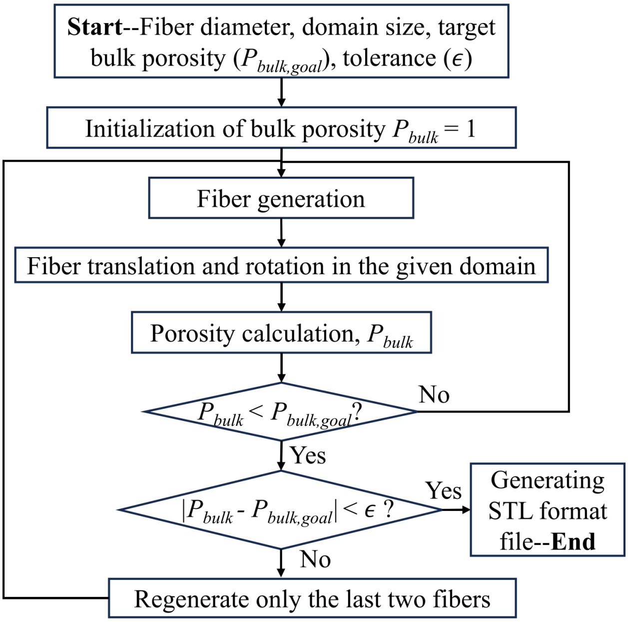

Figure 4.1: Stochastic GDL reconstruction flow chart with random stacking strategy.

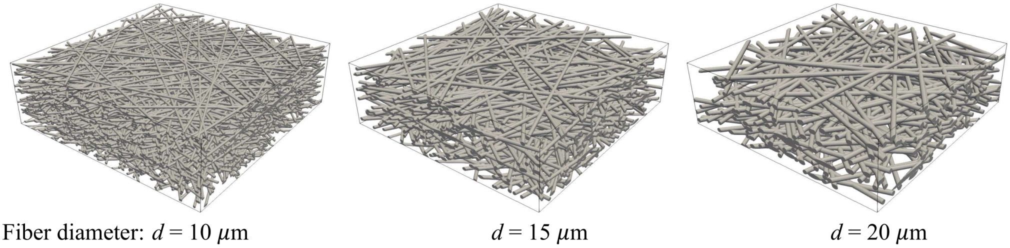

Figure 4.2: Reconstruction using straight cylindrical fibers with diameters of 10 μm, 15 μm, and 20 μm, generated in MATLAB and randomly stacked within a 1000 μm × 1000 μm × 300 μm volume to achieve a target porosity of $P_{bulk,goal}$ = 0.81.

However, upon our investigation, it has been observed that the random stacking strategy inadequately reflects the variations in through-plane local porosity trends, resulting in notable discrepancies in parameters such as pore size distribution among reconstructed GDLs, even with a consistent desired porosity [150]. This issue is scarcely reported in existing literature. Thus, a layer-by-layer stacking approach is developed to achieve a desired layer porosity distribution along the through-plane direction during reconstructions. The reconstruction flow chart has been shown in Fig. 4.3. Compared with the random stacking strategy, the through-plane layer porosity information is required.

This stacking process aims to achieve a target through-plane porosity distribution $P_{goal,i}$ for each layer $i = 1, 2, 3, \ldots, N$, where N is the total number of layers. Each layer has a thickness equal to the fiber diameter. Initially, the porosity of each layer $P_{layer,i}$ is set to 1. As fibers are generated, the volume fraction $\phi_{layer,i}$ within the i_{th} layer is calculated (will be explained in the subsequent), allowing the porosity to be updated as $P_{layer,i} = 1 - \phi_{layer,i}$. This value typically decreases as fibers are added. When the actual porosity $P_{layer,i}$ drops below the target $P_{goal,i}$, subsequent fibers are placed in the next layer. This process repeats until all layers are reconstructed. A stochastic GDL is then reconstructed by stacking the completed layers. Maintaining the target bulk porosity across all layers presents a challenge. To address this, a tolerance of $\varepsilon = 1.5\%$ is applied between the achieved bulk porosity P_{bulk} and the desired value $P_{\text{bulk,goal}}$. If this threshold is exceeded, the fiber layer with the largest deviation between $P_{\text{layer},i}$ and $P_{\text{goal},i}$ is removed and regenerated.

Both stacking strategies require the fiber volume percentage $\phi_{layer,i}$, which can be calculated by V_{fiber}/V_{bulk}. V_{bulk} is obtained by multiplying the length, width, and thickness of the expected region, e.g., total GDL domain or single layer. Nevertheless, the calculation of V_{fiber} varies with the fiber generation method. For straight fiber generated by two coordinates, $M_1(x_1, y_1, z_1)$ and $M_2(x_2, y_2, z_2)$, the V_{fiber} is calculated by the cylinder volume formula, $V_{fiber} = (\pi d^2 ||M_1 - M_2||_2)/4$. $||\mathbf{x}||_2$ represents the Euclidean norm of vector $\mathbf{x}$. On the other hand, for the fiber generated with the periodic surface model, it is complex to calculate the length of the central curves in three-dimensional space with the above cylinder volume formula. Thus, the fiber volume is approximated by the sum of voxels occupied by the fiber, and each voxel resolution is fixed to 1 μm, which is a trade-off between computational time and accuracy.

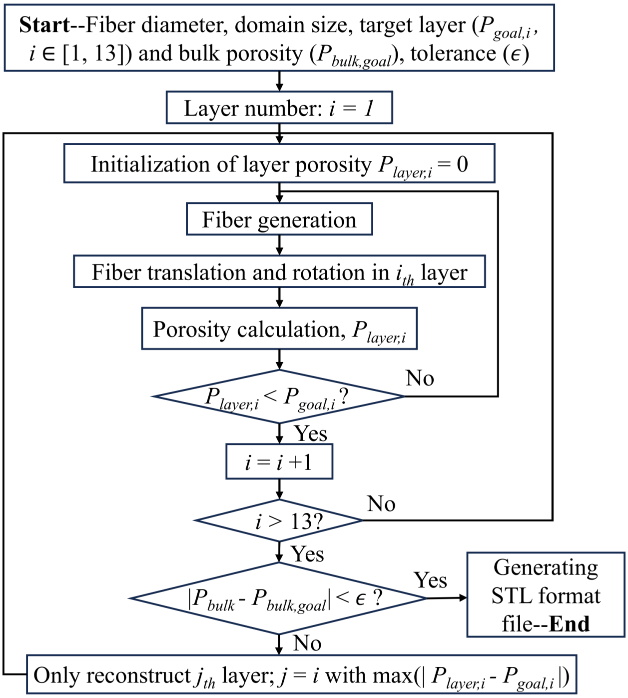

Figure 4.3: Stochastic GDL reconstruction flow chart with layer-by-layer stacking strategy.

In the fiber stacking approach described above, the necessary GDL fiber diameter, domain dimensions, and bulk and through-plane local porosity are obtained from an image-based reconstruction of a Freudenberg H2315 GDL sample [84], as shown in Fig. 4.4. The experimental GDL structure is analyzed using Paraview software following a very fine mesh, with a domain size of 500 μm $\times$ 500 μm $\times$ 117 μm and a bulk porosity of approximately 0.7. This value aligns closely with the same type of GDL, featuring a bulk porosity of 0.69, reported in a previous study [153]. The resulting slice sequence is processed in ImageJ, where the through-plane porosity distribution and fiber diameter were extracted, as shown in Fig. 4.4(c) and Fig. 4.4(d). Based on 178 randomly sampled fibers, the average fiber diameter is calculated, being approximately 9 μm. Additionally, the average porosity, calculated from the through-plane local porosity distribution, is around 0.698, which closely matches the bulk porosity.

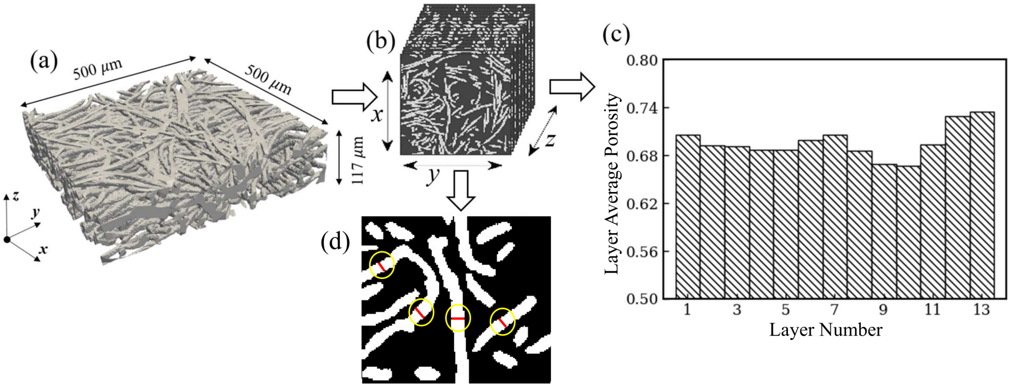

Figure 4.4: (a) Side views of experimental image-based reconstruction of the Freudenberg H2315 GDL. (b) In-plane cross-section slice sequence of the GDL along the through-plane direction with a slicing resolution of 1 μm. (c) through-plane local porosity distribution along the through-plane direction (thickness direction). (d) The determination of GDL fiber diameter through the utilization of pixel measurements in a series of binary images, where the white shade indicates the fiber slice.

Due to the inherent randomness in GDL manufacturing, particularly in fiber orientation, achieving a perfectly ordered structure remains a challenge with current techniques [164]. In light of this, the present study preserves the stochastic nature of fiber orientation rather than imposing an artificially ordered configuration. Three distinct GDL structures have been reconstructed, each characterized by different fiber curvatures: $b = 0, f_r = 0$; $b = 0.2, f_r = 2.5$; and $b = 0.4, f_r = 2.5$. To minimize potential biases introduced by this randomness, four independent samples were generated for each type using a standardized procedure. The reconstruction was carried out through a sequential layer-by-layer stacking technique. Table 4.2 presents the bulk porosity and five-layer porosity values for both experimentally fabricated and virtually modeled GDLs. In this framework, Layer 1 is positioned at the base of the GDL, while Layer 13 is located near the GDL/GC interface. The notations S, C1, and C2 correspond to straight, moderately curved, and highly curved fiber structures, respectively. Across all reconstructions, the deviation in bulk porosity relative to the reference H2315 GDL remains under 1%, meeting the tolerance criterion, while variations in layer porosity do not exceed 2%. These deviations are deemed acceptable within the scope of this study. Further reducing tolerance levels would necessitate stricter constraints, significantly increasing computational time. Additionally, the similarity observed in bulk and layer porosity across different reconstructions highlights the reliability of the layer-by-layer stacking strategy, demonstrating its potential for future controlled fabrication of GDLs. Representative visualizations of the first sample from each category are shown in Fig. 4.5(a-c), illustrating an increasing presence of curved fibers from S-GDL1 to C2-GDL1.

Table 4.2: Structural bulk and layer porosity in GDLs with varied fiber curvatures (S, C1, and C2).

GDL name	Fiber curvature	Bulk porosity	Layer 1 porosity	Layer 4 porosity	Layer 7 porosity	Layer 10 porosity	Layer 13 porosity
H2315 GDL	-	0.6985	0.7165	0.6897	0.7075	0.6688	0.7350
S-GDL1	$b = 0, f_r = 0$	0.7039	0.7282	0.6967	0.7100	0.6780	0.7404
S-GDL2		0.7012	0.7189	0.6908	0.7080	0.6757	0.7418
S-GDL3		0.7027	0.7264	0.6870	0.7107	0.6759	0.7435
S-GDL4		0.7019	0.7246	0.6911	0.7116	0.6769	0.7382
C1-GDL1	$b = 0.2, f_r = 2.5$	0.7006	0.7268	0.6915	0.7049	0.6691	0.7366
C1-GDL2		0.7010	0.7168	0.6957	0.7138	0.6729	0.7395
C1-GDL3		0.7021	0.7268	0.6914	0.7099	0.6686	0.7444
C1-GDL4		0.7021	0.7263	0.6909	0.7166	0.6703	0.7436
C2-GDL1	$b = 0.4, f_r = 2.5$	0.6990	0.7246	0.6867	0.7081	0.6729	0.7404
C2-GDL2		0.6995	0.7148	0.6926	0.7110	0.6701	0.7435
C2-GDL3		0.6989	0.7253	0.6891	0.7078	0.6685	0.7401
C2-GDL4		0.6997	0.7169	0.6866	0.7025	0.6716	0.7364
Maximum deviation	Absolute value	0.0055	0.0135	0.0101	0.0075	0.0095	0.0054
	Percentage	0.78%	1.85%	1.45%	1.05%	1.40%	0.70%

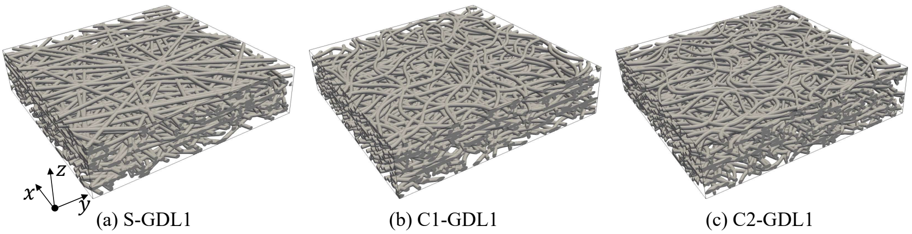

(a) S-GDL1 (b) C1-GDL1 (c) C2-GDL1

Figure 4.5: Three representative GDL configurations with different fiber curvature, reconstructed with the rod periodic surface model and layer-by-layer stacking strategy. (a) S-GDL1 (straight fibers with $b = 0, f_r = 0$); (b) C1-GDL1 (curved fibers with $b = 0.2, f_r = 2.5$); (c) C2-GDL1 (curved fibers with $b = 0.4, f_r = 2.5$).

4.3 Additive structure generation

In the GDL reconstruction process described above, the resulting structures only consist of fiber skeletons without including additive structures. Since adding PTFE and binders introduces non-uniform modifications to the original pore network, Papers II and **III** focus exclusively on the fiber skeletons. This approach allows for isolating and analyzing the specific effects of fiber geometry, without the complicating influence of multiple variables. The surface wettability property, determined by the PTFE distribution and content, is modeled by attributing a fixed contact angle to fiber surfaces, consistent with the method presented in previous GDL research [32, 78, 79, 86, 92].

The influence of binder and PTFE is investigated separately in Paper V. Image-based morphological processing techniques are employed to generate additive structures, following approaches commonly used in previous studies [98, 136, 137, 147, 175, 178]. However, the distinction between reconstructed binder and PTFE structures has not been established. As illustrated in Fig. 4.6, PTFE typically forms a thin coating over fibers and binders. While recent developments in image segmentation enable the identification of binder regions [179], methods for PTFE-targeted segmentation remain limited.

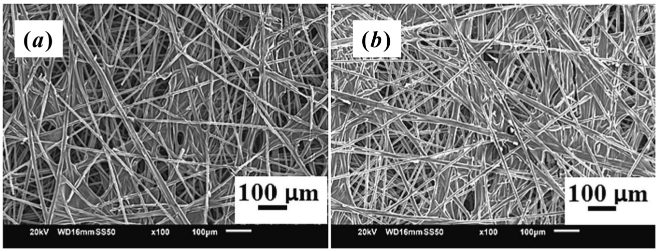

Figure 4.6: Scanning electron microscopy images [180], (a) a binder-treated GDL region without PTFE treatment and (b) a GDL region treated with binder and PTFE. The brightness in PTFE-treated regions is due to fluorine atoms having a higher atomic number than carbon, leading to more backscattered electrons under a scanning electron microscopy beam. Figures are adopted from Calili *et al.* (Chemical Engineering Journal, 2024) [180], with permission from Elsevier.

Due to the lack of detailed understanding of PTFE morphology and the computational cost of resolving such thin coatings with high-resolution meshes, the binder and PTFE phases are not reconstructed separately in this work. Instead, their combined topological impact on the GDL is represented through a unified additive structure. Wettability variations caused by PTFE content are modeled by adjusting the contact angle assigned to the solid surface, providing an effective way to reflect changes in PTFE fraction without explicitly resolving the coating.

Figure 4.7 displays the flow chart for additive generation. The result of solving the periodic surface model is a three-dimensional matrix/voxel labeled either negative or positive floats, which serves as the base of this iterative process. Note that negative values indicate that the corresponding points are located inside the cylinder, and the isosurface with a value of 0 is the cylinder surface. This matrix can be divided into in-plane (along x and y directions) or through-plane (along z direction) two-dimensional slice (image) sequences. They are binarized based on the positivity of the value to enable the use of two-dimensional morphological processing on them. Furthermore, opening or closing processing can be conducted on all in-plane and through-plane binary images based on

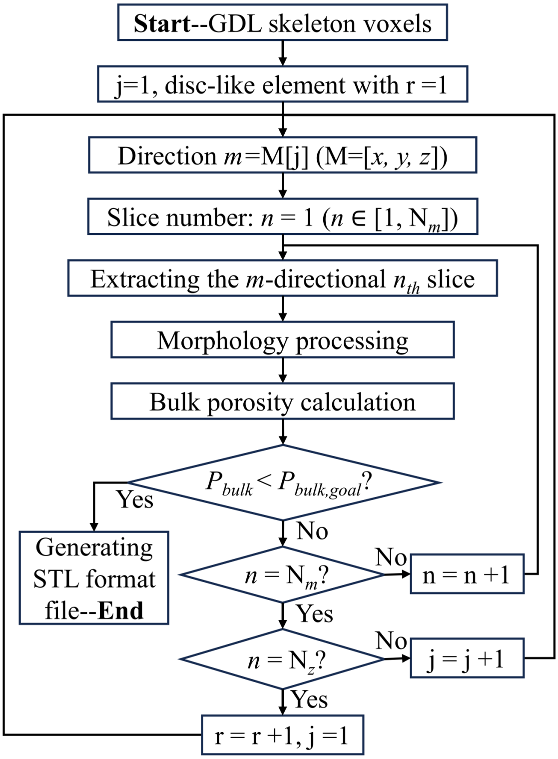

Figure 4.7: Flow chart for additive generation in GDL skeletons.

a disc element with a certain radius r. The selection of a disc-shaped component significantly influences the GDL morphological topology, inducing localized alterations predominantly near fiber intersection regions. This phenomenon aligns with experimental findings wherein binder materials preferentially concentrate at fiber junctions, thereby occluding smaller pores within the GDL microstructure. The compositional percentage of additive structures within the GDL can be modulated by adjusting the disc radius and regulating the number of input images, N_m ($m = x, y, z$), in each direction. The real porosity P_{bulk} is derived from a reduced fiber volume fraction, calculated via voxel-based analysis of the microstructure, which we have discussed in section 4.2. Once the target porosity $P_{bulk,goal}$ is reached, an isosurface extraction algorithm is applied with a threshold value of 0 to the final three-dimensional voxel matrix, yielding a reconstructed surface model of the GDL microstructure.

A series of GDL configurations have been reconstructed in this work, as shown in Fig. 4.8, and the corresponding parameters are summarized in Table 4.3. Specifically, GDL1 is constructed from GDL2 by adding fiber structures, and similarly, GDL2 is derived from GDL3, following a hierarchical reconstruction process until the desired

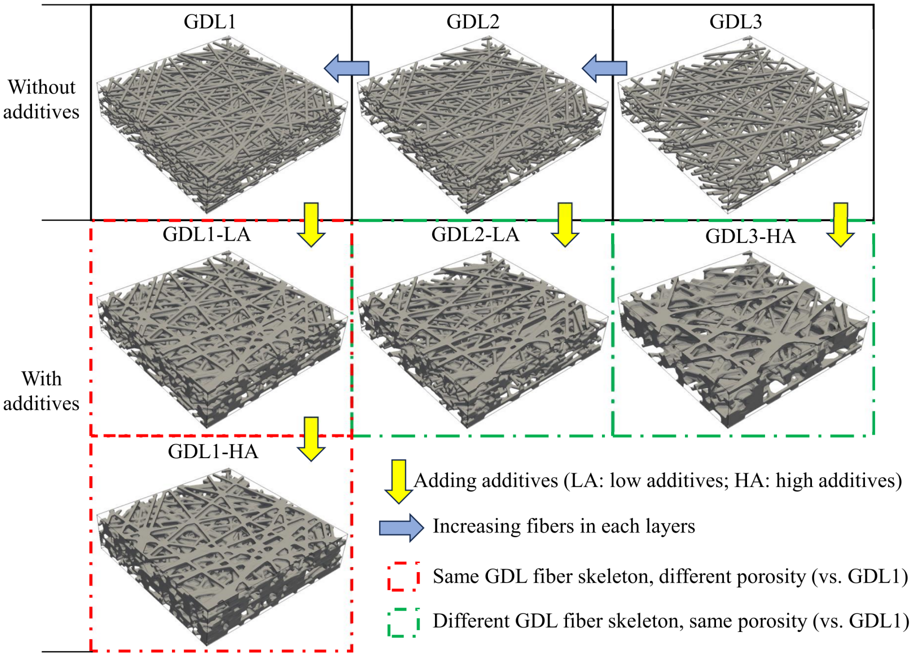

Figure 4.8: A comparison of GDL structures with varying levels of additive incorporation. GDL1-LA and GDL1-HA represent gradually increasing additive content in GDL1, while GDL2-LA and GDL3-HA signify the integration of additives into GDL2 and GDL3, respectively, maintaining a porosity comparable to that of GDL1.

porosity is achieved. This approach ensures that three GDL skeletons share a significant portion of fibers, approximately 50% (0.14/0.3). This type of control has been rarely seen in previous studies. Still, it does reduce the impact of the fiber randomness factor when comparing different samples. It provides a better basis for studying the effects of adjusting additive content and fiber amount.

Table 4.3: The GDL structural properties. Expected and actual values are shown outside and inside the brackets, respectively. (LA: Low Additives, and HA: High Additives.)

Studied GDLs	Fiber volume fraction	Additive volume fraction	Bulk porosity	Additive/Solid
GDL1	0.30 (0.297)	0(0)	0.70 (0.703)	0 (0)
GDL2	0.22 (0.217)	0 (0)	0.78 (0.783)	0 (0)
GDL3	0.14 (0.139)	0 (0)	0.86 (0.861)	0 (0)
GDL2-LA	0.22 (0.217)	0.08 (0.084)	0.70 (0.699)	26.67 % (27.91 %)
GDL3-HA	0.14 (0.139)	0.16 (0.165)	0.70 (0.696)	53.33 % (54.28 %)
GDL1-LA	0.30 (0.297)	0.08 (0.082)	0.62 (0.621)	21.05 % (21.64 %)
GDL1-HA	0.30 (0.297)	0.16 (0.166)	0.54 (0.537)	34.78 % (35.85 %)

Two additive strategies are subsequently examined: (i) incorporating additives while maintaining constant porosity, and (ii) incorporating additives with a concurrent decrease in porosity. While the latter approach aligns more closely with actual GDL manufacturing processes, the former is essential for evaluating the isolated impact of additives, such as binder structures, under controlled porosity conditions. To achieve this, GDL2 and GDL3 are modified with low and high additive volume fractions (0.08 and 0.16, respectively), yielding GDL2-LA and GDL3-HA, both adjusted to match the porosity of GDL1. In parallel, GDL1 is also processed with similar additive fractions (i.e., 0.08 and 0.16), resulting in GDL1-LA and GDL1-HA.

4.4 Pore network extraction

As reflected by the Young-Laplace equation, $P_c = 2\sigma cos(\theta)/R$, under conditions of a consistent contact angle and surface tension coefficient, capillary pressure demonstrates an inversely proportional relationship with pore size. Therefore, for porous media, the pore features (e.g., size and location) serve as a crucial intermediary connecting the complex GDL structure with its internal water dynamics. Pore network extraction is a technique that simplifies complex pore-scale geometries into discrete, topologically representative network structures, consisting of pores and throats [181]. It has been proposed for several decades and is widely used to characterize pore structures and features [182].

The complex geometry of the GDL pore structure poses significant challenges for visualizing its internal morphology. Extracting the corresponding pore network is beneficial for understanding water transport behavior simulated using the VOF model. In this thesis, two open-source Python-based tools, PoreSpy [183] and OpenPNM [181], are combined to generate pore networks from reconstructed GDL geometries. The processing flow chart is shown in Fig. 4.9. First, the reconstructed GDL voxels, processed voxels, can be binarized to an image sequence. Note that each voxel size corresponds to a resolution of 1 μm in real size, which is the same value we adopted in the periodic surface model. With this three-dimensional voxel, a general method to investigate the pore size distribution is using a sphere-filling filter, *local_thickness*, which is based on the maximal inscribed sphere diameter at each voxel in the pore space. Nevertheless, this approach permits the overlap of pores of varying sizes, which poses challenges in visualizing the locations and connections of the pores. Consequently, a marker-based watershed segmentation technique is employed to clearly delineate the pore region and its connections, facilitating the further extraction of the pore-throat network. To achieve this, filtering methods are used to remove overlapped pores and extremely small pores based on a distance map, which is obtained by calculating the minimal Euclidean distance between each voxel and the nearest fiber solid surface. For further details, please refer to the respective websites of these two tools.

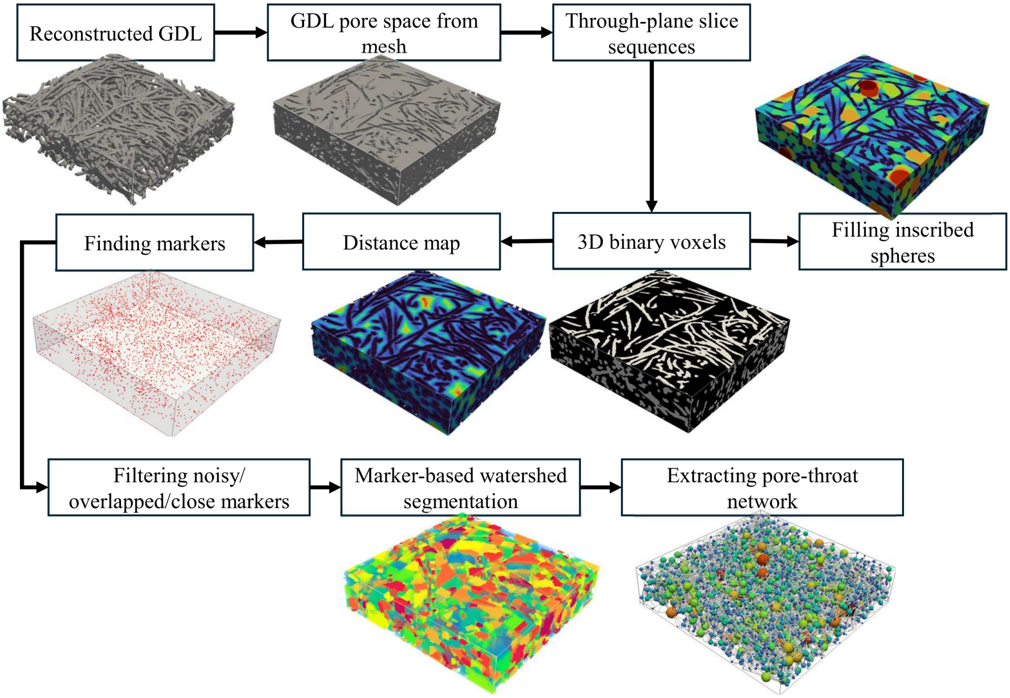

Figure 4.9: Flow chart of a GDL pore network extraction (Note that the GDL used here is only for demonstration purposes).

The watershed indicates throats, denoting the proximity between two adjoining pores. The pores and throats in actual GDL structures are of arbitrary shapes. To enhance clarity, pores are illustrated as spherical balls, and throats are shown as cylinders. The maximal inscribed diameter represents the pore and throat diameter values. The coordination number is introduced in a pore network to describe the number of neighbors of each pore; in other words, a bigger value means more connected pores. Additional significant characteristics of the network, such as pore volume, centroid coordinates, inscribed sphere diameter, throat area, perimeter, centroid, and length, are beyond the scope of this work but are comprehensively introduced in a previous study [184].

Chapter 5

Model evaluation and case setup

5.1 Evaluation of selected liquid velocity

After water is produced in the CL region via electrochemical reaction, it moves very slowly towards the GCs, approximately in a velocity range of 1×10^{-5} to 1×10^{-3} m/s [32, 70, 112, 185], which can be estimated from the reaction rate at different operating conditions. However, using such small values in VOF two-phase flow simulations of GDLs and GCs can result in extremely long computational times to observe the water breakthrough from GDLs or the outflow from GCs. An adequate fine mesh and a small time step are good for decreasing numerical diffusion of the two-phase flow interface. Thus, following an extensive examination of flow regime maps within porous media [186] and microchannels [185, 187], a feasible strategy has been proposed, which is to directly increase the liquid inlet velocity by a certain multiple without changing the flow pattern/dominant force. For example, it has been found that the water in GDLs follows a capillary fingering dominated pattern [188, 189], and the water flow in the GC involves annular flow, droplet flow, and slug flow [187].

This computation acceleration approach has been widely adopted in previous fuel cell two-phase flow studies. The existing maximum multiple is found to be 1000 [32], which still ensures surface tension forces are larger than viscous forces. As a result, the utilized liquid velocity ranges from 0.01 to 1 m/s [73, 92]. Although in this thesis the liquid inlet velocities, i.e., 0.02 m/s for GDLs and 0.1 m/s for GCs, have been comparable with those in the previous studies, the effect of accelerating liquid velocity within the GDL remains insufficiently explored in this specific field. Most of them are based on force analysis using dimensionless numbers, and only a few visual results are available. A more detailed analysis is required to illustrate how the acceleration influences liquid transport dynamics. Understanding this aspect is crucial for improving model reliability and further optimizing GDL design for enhanced water management in fuel cells.

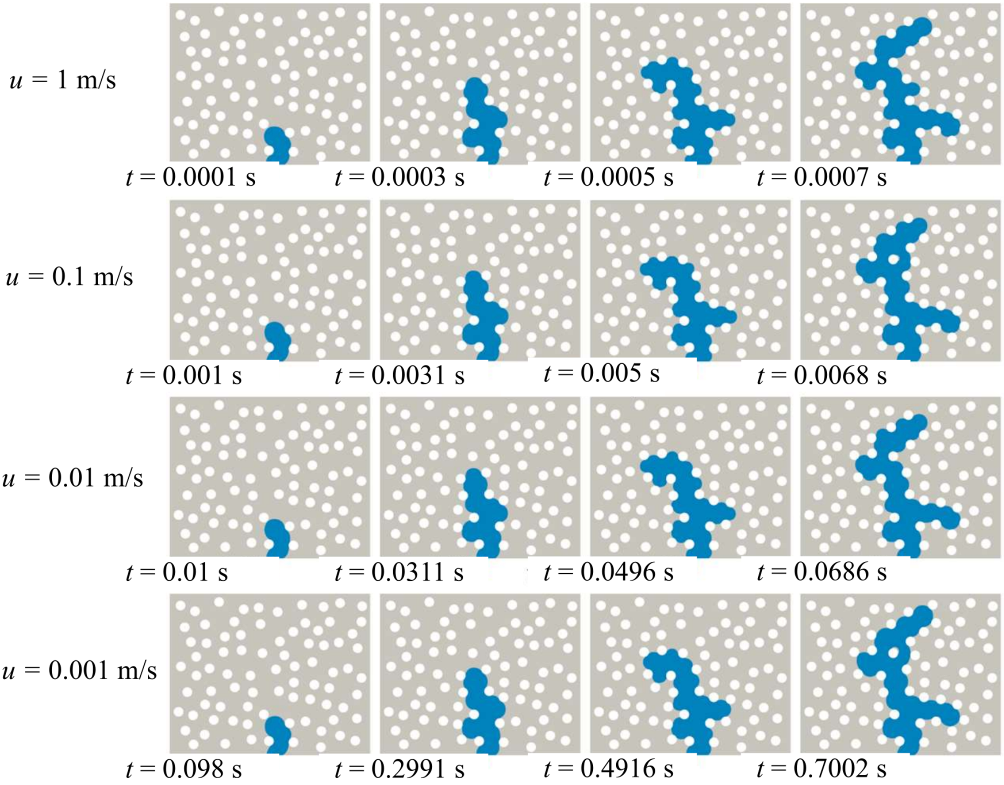

Figure 5.1: The liquid (blue color) evolution in a 2-dimensional porous geometry with different velocities, i.e., 1 m/s, 0.1 m/s, 0.01 m/s, and 0.001 m/s.

Thus, four two-phase flow scenarios with water velocities of 0.001 m/s, 0.01 m/s, 0.1 m/s, and 1 m/s are simulated. Considering the high computational cost with the lowest water velocity, all test simulations utilize a two-dimensional rectangular domain (206 μm in length, 178 μm in height, and a porosity of 0.76) to establish fundamental insights before extending to more complex three-dimensional cases. The liquid evolution for each scenario is displayed in four timesteps, as shown in Fig. 5.1. For any two scenarios, comparable liquid distributions are observed when the time step ratio is similar to the velocity ratio. Figure 5.2 compares their water saturation changes over time, and only a minor difference is found among the three scenarios using 0.1 m/s, 0.01 m/s, and 0.001 m/s, which mainly occur during the water breakthrough period. In the 1 m/s scenario, water accumulation is similar before the first breakthrough, but its changes are slower afterward compared with the other cases. This suggests that increasing the liquid injection velocity to 0.1 m/s results in a slight difference in liquid distribution and evolution, with reduced simulation time and computational cost, demonstrating the feasibility of the adopted liquid injection acceleration.

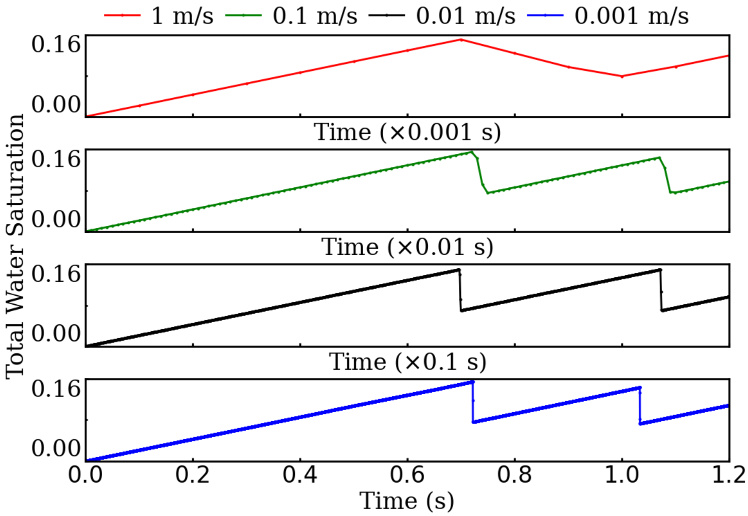

Figure 5.2: The liquid water saturation over time with different velocities, i.e., 1 m/s, 0.1 m/s, 0.01 m/s, and 0.001 m/s.

5.2 Mesh independence study

It is found that mesh independence studies for two-phase flow numerical simulations in the GDL are rarely presented in previous research. Possible reasons can be the high computational cost associated with mesh refinement. To establish a valuable reference for future studies and ensure the reliability of the simulation results analyzed, three different meshes (Mesh 1, 2, and 3) are designed, as shown in Table 5.1. Mesh 1 serves as the base mesh, while Mesh 2 and Mesh 3 are successively refined by a factor of 1.3 in each of the GC and GDL dimensions. The resolution of Mesh 1 in the GC and GDL is already comparable with those in previous studies [32, 64, 190]. Figure 5.3(a-b) presents the total water saturation over time and through-plane local water saturation at 4 ms, showing similar trends across all three meshes. However, as seen in Fig. 5.3(c), the water accumulation in the upper corners of Mesh 1 differs significantly from the other two meshes, with an additional flow path emerging near the right corner. Considering both accuracy and computational cost, Mesh 2 is selected for subsequent studies. In this mesh independence analysis, water was injected from the bottom of the thin region beneath the GDL, which explains the initial delay in water accumulation, as shown in Fig. 5.3(a).

Table 5.1: Mesh comparison with different grid resolutions.

	Mesh cells	Mesh resolution (μm$\times\mu$m$\times\mu$m)	
		GC	GDL
Mesh 1	3.4 Million	10.87 × 10.87 × 10.87	2.72 × 2.72 × 1.72
Mesh 2	7.2 Million	8.3 × 8.3 × 8.3	2.08 × 2.08 × 1.46
Mesh 3	15 Million	6.4 × 6.4 × 6.4	1.6 × 1.6 × 1.05
Ref. [32]	-	≈ 13 × 13 × 13	≈ 6.8 × 6.8 × 6.8
Ref. [64]	-	≈ 25 × 25 × 25	-
Ref. [190]	-	-	≈ 3 × 3 × 1.47

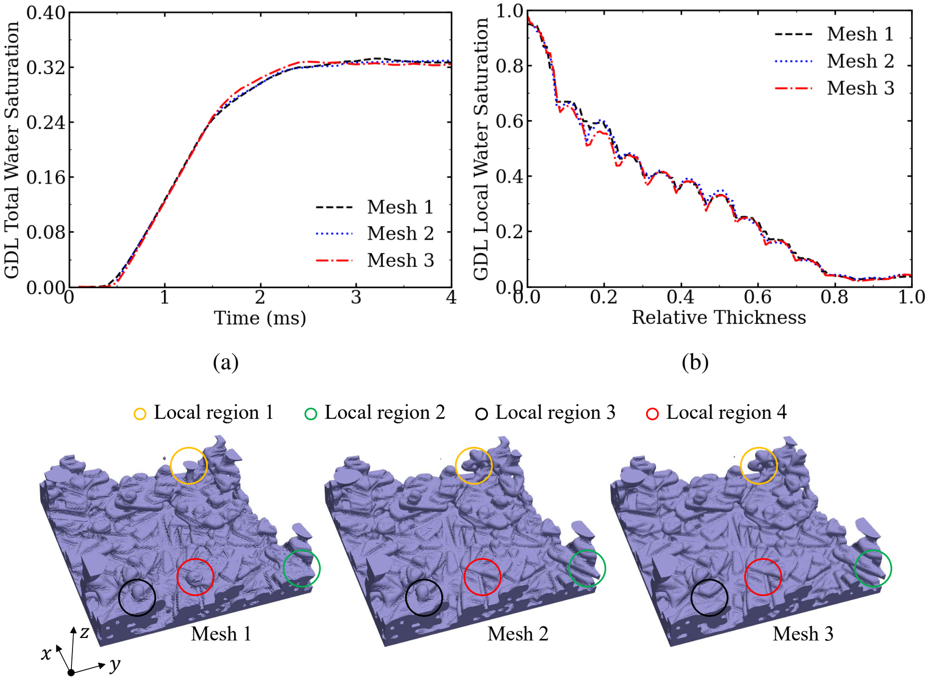

(a)

(b)

(c)

Figure 5.3: Mesh sensitivity analysis results, (a) Time-dependent total water saturation in GDL. (b) Through-plane local water saturation at $t = 4$ ms. (c) Water distribution in the GDL at $t = 4$ ms. Mesh 1: based mesh; Mesh 2: middle mesh; Mesh 3: finer mesh.

5.3 Model evaluation

The VOF method, implemented in OpenFOAM, has been validated in various situations, such as bubble rise [166, 191], dam break [192, 193], and multi-scale channel flow [105, 194]. To guarantee the reasonableness of the results in this thesis, several model evaluation cases have been conducted.

Case 1

The simulation of a two-dimensional rising bubble is conducted utilizing the *interFoam* solver as well as the associated schemes described in the previous chapter of this thesis.

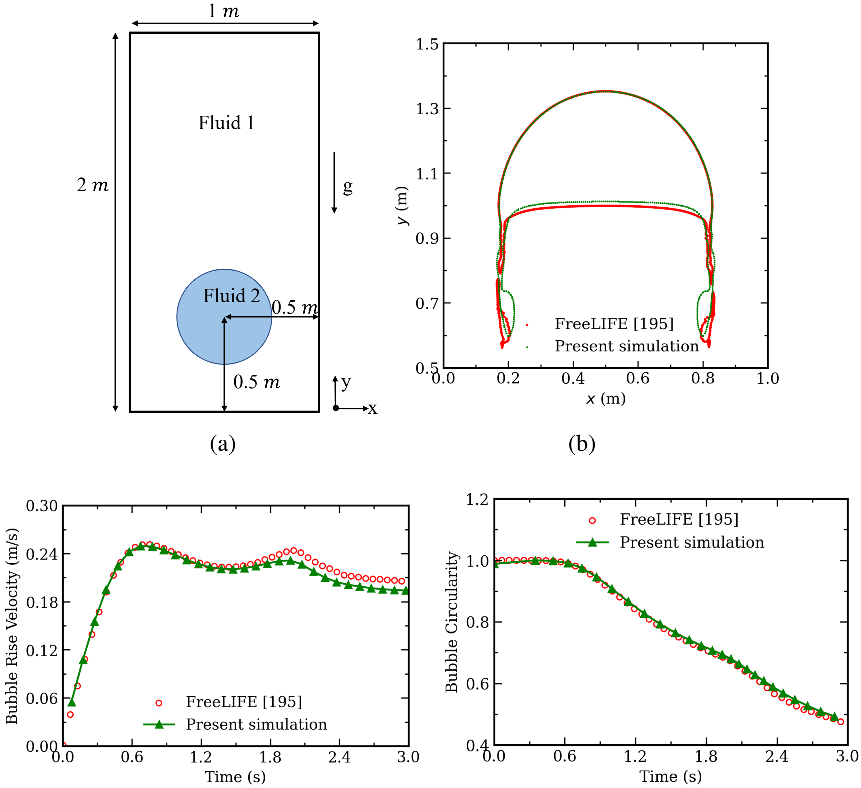

(a) (b)

(c) (d)

Figure 5.4: (a) The geometry for simulation model comparison on a rising bubble. (b-d) Comparison of the bubble shape, bubble rise velocity, and circularity of a single rising bubble simulation between the VOF in OpenFOAM and the LS simulation method, FreeLIFE [195].

Figure 5.4(a) shows the simulation geometry. Figure 5.4(b-d) illustrates the bubble shape at 3 s, and the bubble rise velocity and circularity within 3 s. These results are compared with those in a previous work [195], which utilized a FreeLIFE solver based on the level-set method. Both simulations demonstrate a reasonable level of similarity. Nevertheless, it is difficult to ascertain the superiority of one solver over the other in the absence of comparative experimental results. A difference in bubble shape is observed around the trailing edge of the bubble, which relates to the difference in Fig. 5.4(c-d) between the two simulations. This difference can be attributed to various possible reasons, such as mesh resolution and discretization schemes, as well as water-gas interface reconstruction schemes, as thoroughly examined in a comparative study by Esteban *et al.* [59]. However, for the purpose of this thesis, the observed similarities provide initial credibility for adopting the VOF approach.

Case 2

To validate the numerical method for two-phase flow in GCs, droplet emergence in a microchannel is simulated and qualitatively compared to observed experimental images [196].

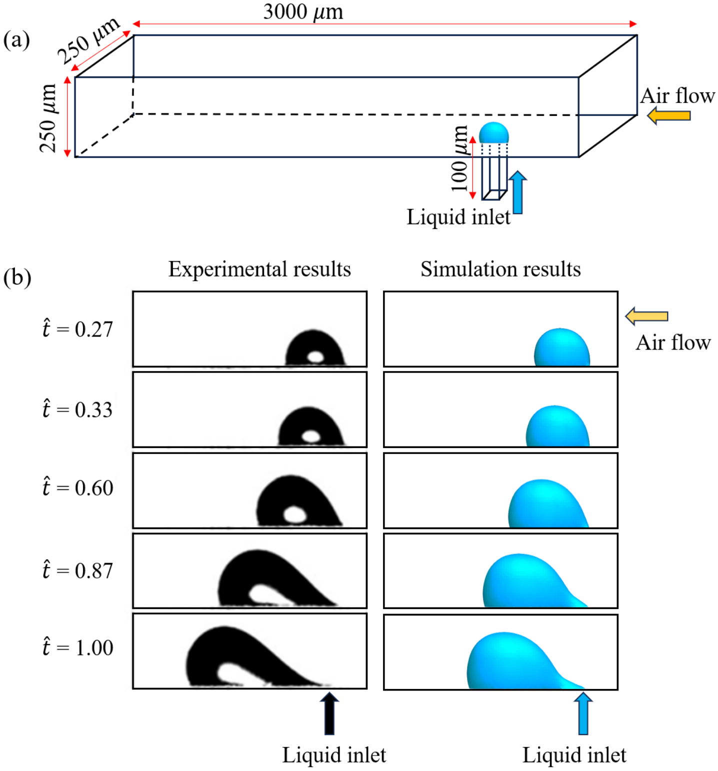

Figure 5.5: (a) Schematic diagram of the simulation validation geometry, where the GC and liquid inlet have the same cross-sectional dimensions as the experimental configuration. (b) Comparison between the present numerical results and the experimental images observed by Wu *et al.* [196] at the same $\hat{t}$. $\hat{t}$ is the ratio of the selected time to the droplet detachment time in the experiment and simulation, respectively.

The simulation geometry consists of a long cuboid channel measuring 250 μm × 250 μm × 3000 μm, incorporating a small cuboid hole with dimensions of 50 μm × 50 μm × 100 μm, as shown in Fig. 5.5(a). These dimensions match the microchannel in a comparison experiment, except for the channel length. According to the experimental measurements, a static contact angle of 110 ° is set at the channel bottom surface. Both experiments and simulations utilize the same air and liquid inlet flow velocity, 10 m/s and 0.04 m/s, respectively. In Figure 5.5(b), it can be seen that the VOF method we adopted in this work can simulate water dynamics similar to those observed in previous experiments. For example, it accumulates in an almost symmetrical hemispherical shape above the liquid inlet. After accumulating to a certain size, it gradually moves toward the GC outlet and forms a slender ”tail”. The slight difference may stem from the absence of surface roughness and interface reconstruction, as well as the method used to represent wettability in the VOF method (e.g., static or dynamic contact angle).

Case 3

Furthermore, the VOF method has been used to validate the two-phase flow simulation in the porous GDLs. An initial comparison between experimental and our numerical results has been presented. The local liquid water saturation of the reconstructed GDLs in the through-plane direction is compared with the X-ray tomographic experimental data in [140] and previous study results [90]. However, there are challenges in utilizing identical GDL structures as those employed in the referenced experimental and numerical investigations.

A GDL structure with 10 μm fiber diameter, utilized in Paper II, has been selected to simulate alone without the GC. Most of the conditions have been set to match those in the literature [90], which are similar to the experimental conditions. The GDL surface contact angle is θ = 109 °, and a pressure difference Δp = 1000 Pa is applied between the GDL inlet (bottom side) and outlet (top side). The fiber diameter and porosity of the experimental GDL are 10 μm and 0.78, and the referring literature [90] has the value of 8 μm and 0.73. These values are close to those in this case. The pressure difference drives the water to rise. Essentially, the pressure difference of 1000 Pa is smaller than the liquid breakthrough capillary pressure, which is approximately 5000 Pa [90]. Therefore, the liquid water stops rising at a finite height lower than the GDL thickness once the two forces reach equilibrium. According to Fig. 5.6, the simulated local water saturation qualitatively exhibits a similar trend to both compared results, showing a rapid decrease in water saturation near the GDL inlet and reaching zero at a specific relative thickness position. Specifically, the results are closer to those in [90], and both of them are lower than the experimental results. The liquid water stops rising at a relative thickness of around 0.2 for both studies. However, the experimental case has a higher water saturation and larger thickness. There are several reasons that can account for the differences between this study and the compared studies. Firstly, the contact angle of real GDL fibers is not evenly distributed. Additionally, the porosity distribution of the GDL in numerical and experimental studies differs.

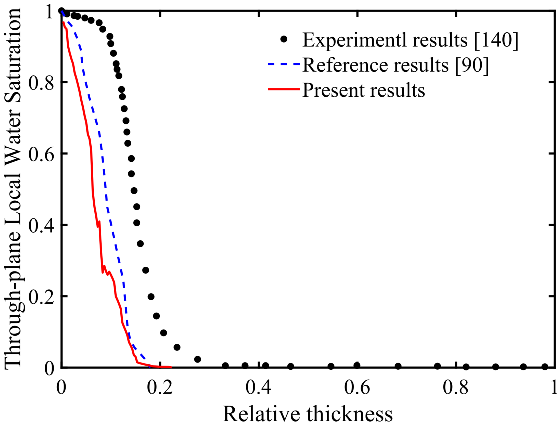

Figure 5.6: Comparison of the local liquid water saturation in the through-plane direction of GDLs between the present results and X-ray tomographic experiment data [140] as well as previous study results [90]. Operation conditions: contact angle of carbon fiber is θ = 109 °, and a pressure difference Δp = 1000 Pa is applied between the GDL inlet and outlet side.

An ideal comparison should guarantee the same topology in experiments and simulations. Nevertheless, unlike the relatively regular GC domain, the mentioned geometry consistency is usually hard to achieve or is not stated clearly for such a complex and random porous microstructure in previous investigations. Considering the trade-off among cost, flexibility, and experimental conditions, the utilization of Stochastic GDL reconstructions in two-phase flow simulations is more widespread [106]. However, relevant experimental data related to the GDL water behavior are still crucial. The demand for publicly accessible experimental results, essential for model validation, is increasing in significance. Niblett *et al.* [32] have used the same GDL geometry for both experimental and numerical studies, as exhibited in Fig. 5.7(b). Both methods show a similar GDL through-plane water saturation trend, starting to decline from around 0.32. However, it can be seen that there is still some difference between the experiment and simulation despite keeping the same geometry. This may be because both experimental image-based porous structure reconstructions and water saturation measurements are highly based on high-resolution scanning techniques and image processing approaches, where inherent errors increase the difficulty of providing precise results. However, the results are still reasonable and acceptable. In the present research, we stochastically reconstruct a GDL and run a two-phase flow simulation by utilizing some of the same key parameters as those used in the [32] experiments. Our simulation results are compared with their experimental and numerical results. The simulation geometry shown can be found in Paper III, and vital parameters have been listed in Table 5.2. The present simulation shows reasonable results compared to the previous results. Acceptable differences may come from different GDL structures, simulation schemes, and GDL randomness, which will be discussed further.

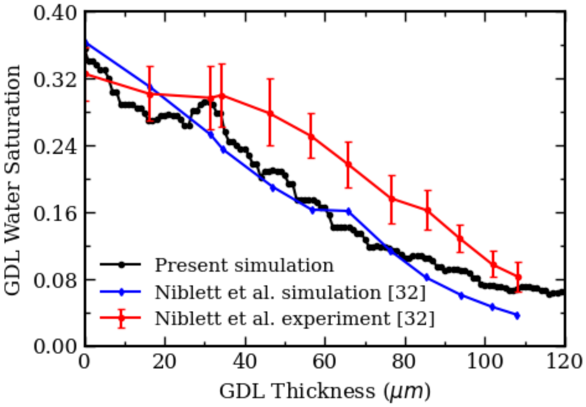

Figure 5.7: In a GDL/GC system, comparison of the GDL through-plane water local saturation in the present work with both experimental and numerical results in [32]. The simulation results in both studies are all extracted from the same simulation time step, $t = 4.5\ ms$.

Table 5.2: Parameter comparison between present study and previous study [32].

Parameters	Niblett *et al.*[32]	Present validation study
GDL Size	786 μm × 848 μm × 165 μm	800 μm × 800 μm × 165 μm
GC Size	800 μm × - μm × 300 μm	800 μm × 800 μm × 300 μm
GDL inlet	500 μm diameter, 50 μm thickness	Same
GDL fiber contact angle	139 °	Same
GC wall contact angle	56 °	Same
Operation temperature	80 °C	Same
Porosity	-	0.88^{a*}
Fiber diameter	-	9 μm [178]
Water inlet velocity	0.0287 m/s	Same
Air inlet velocity	15 m/s	Same

^{a*}: https://www.fuelcellstore.com/spec-sheets/SGL-GDL_24-25.pdf

5.4 Simulation case setup

For numerical simulations in the continuum domain, an appropriate virtual geometry needs to be constructed to constrain the flow. Depending on the purpose of the study and the available computational resources, this geometry can be similar in scale to the actual simulation object or reasonably simplified. Due to the high computational cost, it is impractical to simulate the interface-resolved two-phase flow in a complete PEMFC. In particular, water production involves the multi-scale and multi-physics coupling of electrochemical reactions, mass transfer, heat transfer, and fluid dynamics. Incorporating all of them into simulations, such as VOF, remains challenging. Therefore, two-phase flow simulations are distributed to different components of the fuel cell, including GC, GDL, MPL, CL, and membrane. Thus, the water injection process in each simulation domain is also simplified. This thesis first focuses on the water behavior in a straight GC and then extends its interest to the T-shaped GDL and GC components.

5.4.1 Two-phase flow in straight GC

A straight rectangular GC with multiple small rectangular water injection channels is built, as shown in Fig. 5.8(a). Fig. 5.8(b) displays three types of water inlet configurations and some key dimensions. Due to the randomness of GDL water breakthrough, there are different possibilities for arranging liquid inlets when studying the two-phase flow in GCs. Previous studies have demonstrated that the behavior of water is influenced by the size, shape, and position of a single liquid inlet [64, 105]. However, the single water inlet is not enough to reflect the water dynamics within GCs, as water is found to randomly break through from different locations at the GDL/GC interface [70–72, 99, 197]. Therefore, this study considered three water inlet configurations with the same number of water inlets, whose water inlet ratios from near sidewall 1 to the centerline of the GDL/GC interface and then near sidewall 2 were 10:20:10 (Type I), 0:40:0 (Type II), and 20:0:20 (Type III), respectively. Type I was considered as a base type to study the effect of surface wettability, and Types II and III are two extreme types for comparison. Furthermore, previous research has shown that perforations in the GDL can facilitate liquid breakthrough at these sites [198], suggesting the potential for designing different liquid inlet configurations for practical applications. The size of the water inlets is standardized to 80 μm in width, 80 μm in length, and 100 μm in thickness. Compared with previous studies that used square water inlets ranging from 35 to 200 μm [60, 61, 64], and cylindrical or circular inlets with diameters between 50 to 400 μm [62, 70, 71, 99], this water inlet dimension aligns with prior research. Finally, given the random nature and difficulty in determining the distance between breakthrough locations, this study selected the distance between the two inlets from 500 μm to 2000 μm. Previous studies have reported even larger distances [68, 72].

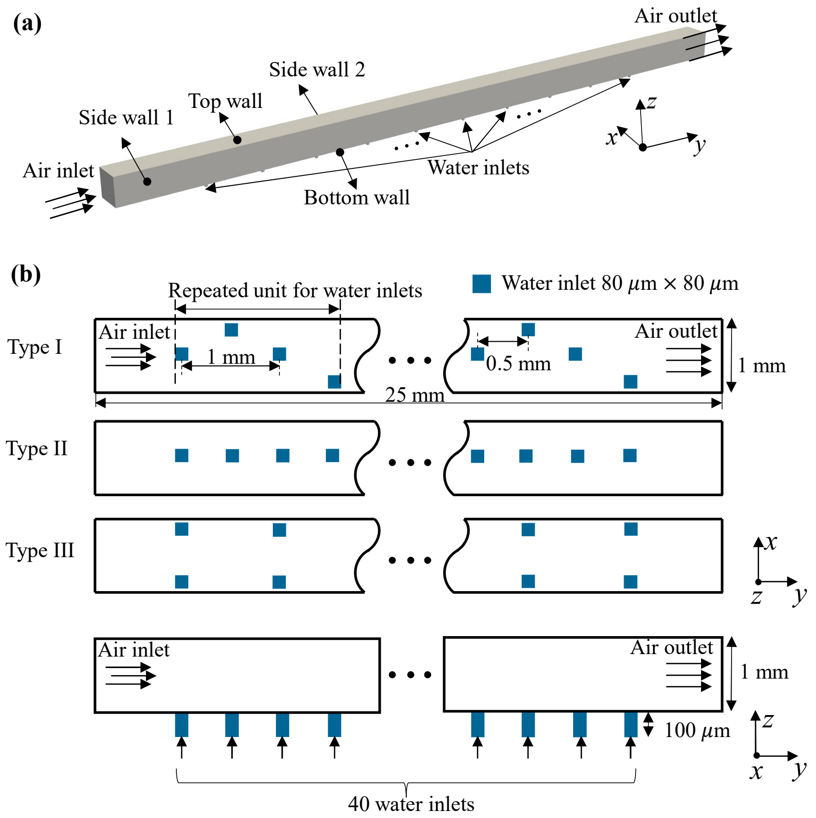

Figure 5.8: (a) Single straight three-dimensional simulation GC geometry scheme. (b) Three water inlet configurations at the GC bottom with separate x-y side views and common and y-z side views. Their water inlet ratios, from near sidewall 1 to the centerline of the GDL/GC interface and then near sidewall 2, were 10:20:10 (Type I), 0:40:0 (Type II), and 20:0:20 (Type III), respectively.

5.4.2 Two-phase flow in GDL and GC assembly

To investigate the water flow behavior within the GDL and GC and eliminate the assumption of artificial GC liquid injection, a T-shaped GDL/GC assembly structure was designed with a small fibrous GDL domain located below the central region of a long GC, as shown in Fig. 5.9(a). This special design balances the research goal and computational cost, as resolving the GDL pore space introduces a significant number of fine mesh cells, which occupy approximately 80% of the total mesh cells. The former section of the GC ensures that the input gas flow is fully developed, and the section that follows is used to observe the removal of liquid water in the GC. The GDL provides a fibrous, porous region for studying the water flow behavior within it, enabling a more realistic water flow breakthrough at the GDL/GC interface.

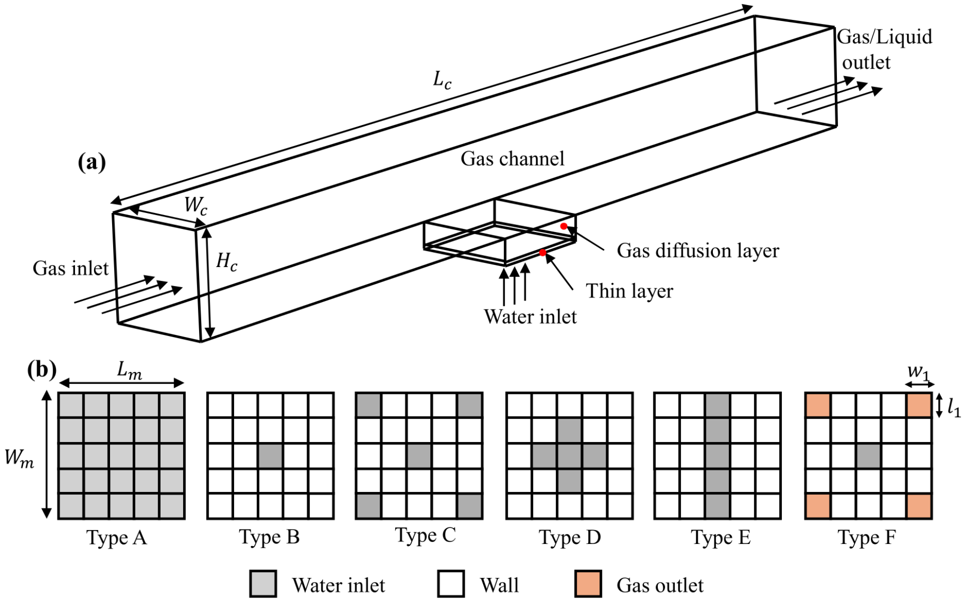

Figure 5.9: (a) A T-shaped GDL/GC assembly geometry. (b) Five different GDL water inlet configurations (Type A-E) and a water inlet/air outlet configuration (Type F).

Papers II, III, IV, and V all employ a T-shaped simulation domain, but there are key differences that need clarification. As shown in Table 5.3, Paper II uses the exact GC cross-sectional dimensions as Paper I but features a significantly shorter GC length to reduce computational cost. However, this configuration still resulted in high computational demands. Therefore, in Papers III, IV, and V, the entire domain was further reduced by approximately half in each spatial direction compared to Paper II, achieving a better balance between computational efficiency and geometric representation in GC and GDL. Besides, there is no thin layer in Paper II, which has been added in later studies to eliminate the effect of GDL surface porous features on water injection, such as mass flow rate.

Water flow is input from a thin region beneath the GDL, with various checkerboard-patterned water inlet configurations designed by adjusting the size and location, as illustrated in Figure 5.9(b). In this figure, white regions indicate walls, while gray regions denote water injection points. A full-area inlet configuration (Type A) is employed in Papers II, III, and V. At the same time, Paper IV evaluates the effects of five inlet patterns (Types A–E) on drainage behavior using the Freudenberg H2315 GDL sample. Additionally, while most prior studies of two-phase flow in GDLs have focused solely on water transport, they often neglect gas transport. To address this gap, a new inlet configuration (Type F) is introduced, based on Type B, which replaces the four corner walls with gas outlet holes (marked in orange) to facilitate gas movement.

Table 5.3: Dimensions of the reconstructed ”T-shape” geometry in different studies.

Parameters	Symbol	Value in Paper II	Value in Papers III, IV, and V	Unit
Channel length	L_c	7	4.5	mm
Channel width	W_c	1	0.5	mm
Channel height	H_c	1	0.5	mm
GDL length	L_p	1	0.5	mm
GDL width	W_p	1	0.5	mm
GDL thickness	H_p	300	117	μm
Thin layer length	L_m	-	0.5	mm
Thin layer width	W_m	-	0.5	mm
Thin layer thickness	H_m	-	10	μm
Thin layer unit cell length	l_1	-	100	μm
Thin layer unit cell width	l_1	-	100	μm
GDL fiber diameters	d	10/15/20	9	μm

Chapter 6

Results and discussion

This chapter synthesizes the main results and discussion in the appended papers. The discussion begins with two-phase flow simulations within GCs and then extends to simulations involving combined GC and GDL assemblies. For more details, please refer to the respective publication.

6.1 Two-phase flow in GCs

6.1.1 Experimental characterization

As outlined in Section 2.2.3, one of the key research gaps is the lack of a unified understanding of wettability in fuel cell flow channels. This section presents insight into this issue by examining the performance and durability of two identical single-cell fuel cells through experimental characterization (in collaboration with SINTEF) and two-phase flow simulations, as detailed in Paper I. Both fuel cells feature 25 cm^2 serpentine graphitic flow fields sourced from BalticFuelCells GmbH. The first cell, acquired in 2017, has undergone extensive use, whereas the second, purchased in 2023, was minimally used before this study.

Figure 6.1 displays the differences in BPP wettability between the two graphitic BPP flow fields using droplet-dropping experiments. The lightly utilized BPP shows enhanced hydrophobicity, as indicated by water droplets forming discrete beads on its surface. In contrast, the extensively utilized BPP demonstrates increased hydrophilicity, characterized by the spreading of water along its flow field channels. This contrast suggests underlying variations in surface properties, likely resulting from material aging or prolonged operational exposure, which may impact water management efficiency and overall cell performance.

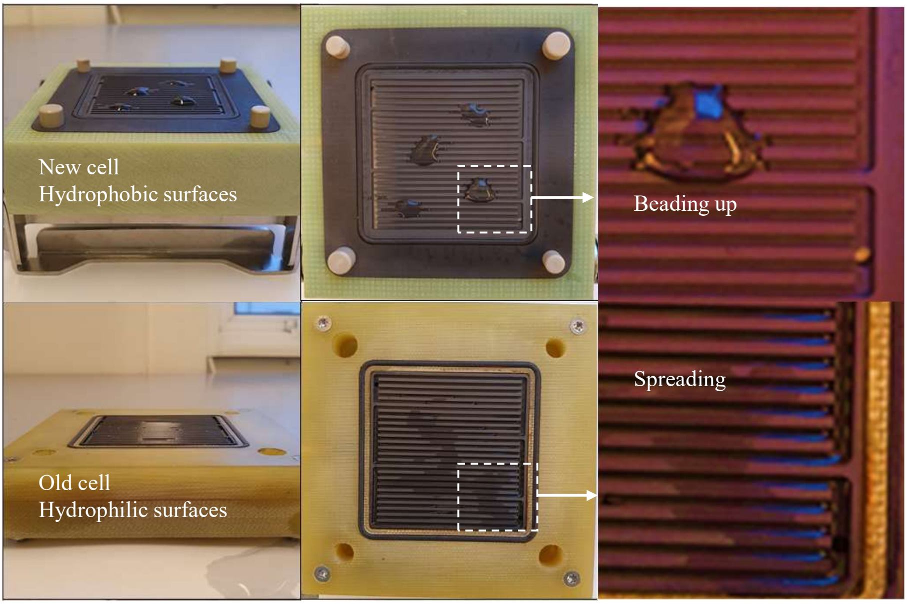

Figure 6.1: Water deposition on graphite BPPs from New and Old Cells, highlighting wettability differences. (Our collaborator from SINTEF conducts this experiment.)

To further investigate the influence of wettability transition on fuel cell performance, two PEMFCs were assembled using identical MEA components, while retaining BPPs of different aging states, one relatively new and hydrophobic (referred to as the ”New Cell”) and the other aged and more hydrophilic (”Old Cell”). Both cells were operated continuously at a constant current density of 1000 mA/cm^2 for 500 hours, with electrochemical characterization conducted at 125-hour intervals to systematically assess performance evolution and degradation trends.

Figures 6.2(a-b) present the fuel cell potential and ohmic resistance curves against current density at five operational stages for New and Old Cells, respectively. At the beginning of the operation, Old Cell shows lower performance compared to New Cell, indicating pre-existing degradation effects. With extended operation, both the potential and maximum current density of Old Cell drop significantly, highlighting the challenge of long-term stability. In contrast, New Cell maintains a maximum current density of 2000 mA/cm^2 even after 500 hours, indicating its superior durability and stability. Moreover, New Cell shows lower Ohmic resistance than Old Cell in the medium-to-high current density regions, where water generation is most pronounced. This observed trend in Ohmic resistance further supports cathode flooding as a plausible explanation for the differences in polarization behavior. Liquid water accumulation at the cathode enhances membrane hydration via back diffusion [199], improving proton conductivity. However, the excess water also blocks catalyst sites and increases mass transport resistance, ultimately offsetting the hydration benefits.

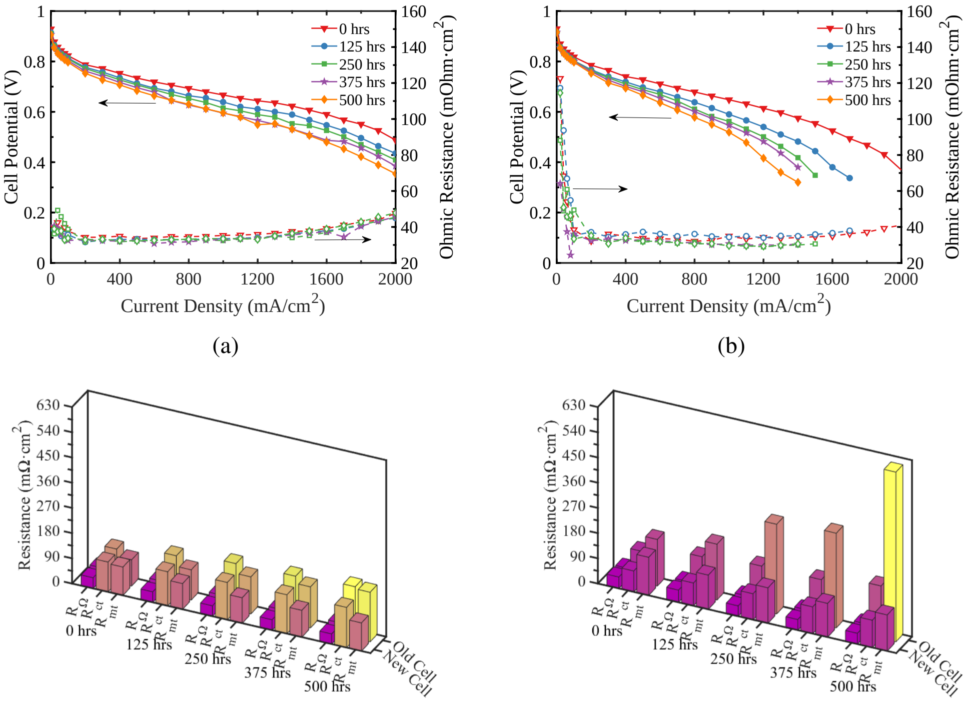

(a) (b)

(c) (d)

Figure 6.2: (a-b): Polarization curves over 500 hours for New and Old cells, illustrating performance degradation. (c-d): Comparison of ohmic resistance (R_Ω), charge transfer resistance (R_{ct}), and mass transport resistance (R_{mt}) at 600 mA/cm^2 and 1200 mA/cm^2, respectively. (Our collaborator from SINTEF conducts this experiment.)

Electrochemical impedance spectroscopy was conducted at current densities of 600 and 1200 mA/cm^2 to evaluate Ohmic (R_Ω), charge transfer (R_{ct}), and mass transport (R_{mt}) resistances in the New and Old Cells, as shown in Fig. 6.2(c–d). The resistance values were obtained from Nyquist plots using equivalent circuit fitting. At the beginning of operation, both cells showed comparable R_{mt} values, in agreement with the corresponding polarization curves. As the test progressed, R_{mt} in the Old Cell rose sharply, from 167 to 606 mΩ·cm^2, whereas the New Cell maintained relatively stable values in the range of 121-136 mΩ·cm^2. A similar trend was observed for R_{ct}, which increased by 53% and 68% in the Old Cell at 600 and 1200 mA/cm^2, respectively, while the New Cell presented smaller increases of 35% and 31%. These variations strongly suggest that performance degradation in the Old Cell is mainly associated with increased charge and mass transport resistances, likely driven by progressive water accumulation. Additional electrochemically active surface area and hydrogen crossover measurements have been analyzed in Paper I, indicating that catalyst and membrane degradation may contribute indirectly to the observed resistance trends.

To further investigate the causes of hypothesized flooding at the cell scale, particular attention is directed toward local water distribution within the BPP channels. Two-phase flow behavior in GCs was simulated by conducting VOF simulations. Surface wettability effects were modeled through static contact angles of 30 °, 90 °, and 150 °, representing hydrophilic, neutral, and hydrophobic conditions, respectively.

6.1.2 BPP channel wettability

Figure 6.3 shows water saturation, spatial distribution, and gas pressure drop in a straight GC under three different surface wettability conditions. All cases employ the Type I liquid inlet configuration shown in Fig. 5.8. Static contact angles of 30 ° (hydrophilic), 90 ° (neutral), and 150 ° (hydrophobic) are used to represent the wettability variety.

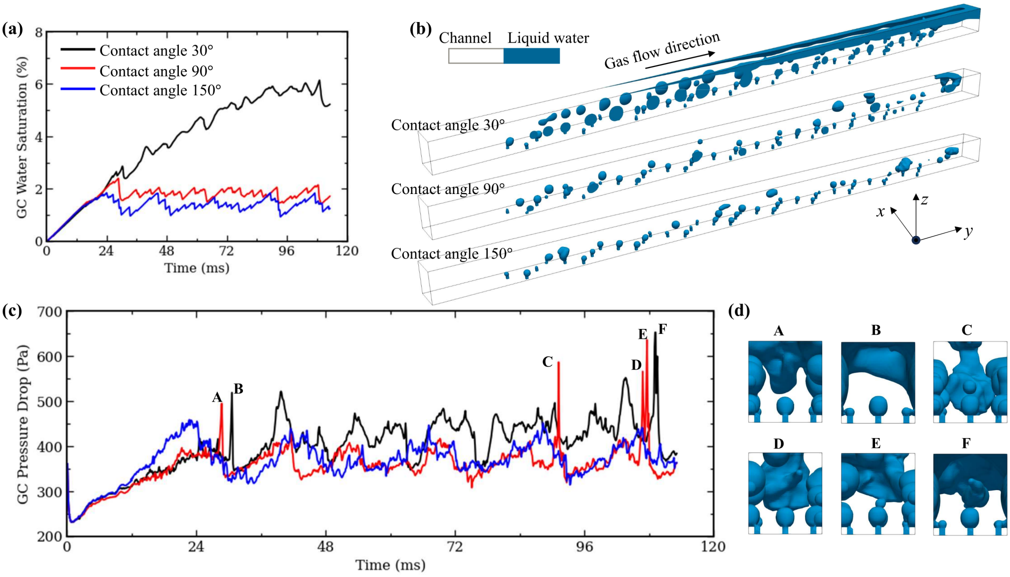

Figure 6.3: (a) Liquid flow evolution in GCs with three different contact angles (30°, 90°, and 150°). (a) Time-dependent total GC water saturation. (b) Water distribution at 108 ms. (c) Time-dependent total GC gas pressure drop. (d) Water distribution viewed from the GC inlet at various time points (A, B, C, D, E, F) corresponding to those in subfigure (c).

In Fig. 6.3(a), the hydrophilic GC shows the largest amount of water accumulation and the longest time (around 108 ms) for statistical stabilization. The difference between hydrophobic and neutral GCs is slight. Both show rapid statistical stabilization at low water saturation, around 24 ms, indicating enhanced water removal efficiency with increasing channel surface hydrophobicity. Figure 6.3(b) shows three GC water distributions at 108 ms. The hydrophilic channel finally forms slug flow along the two GC corners, resulting from the prolonged water retention. Another two GCs still show discrete droplet flow. In the hydrophilic GC, the inertial effect on water transport is negligible. Water movement is primarily governed by surface tension force and gas-induced drag force. Surface tension force promotes liquid adhesion to the channel walls, stabilizing the flow and suppressing rapid displacement. Meanwhile, the shear stress induced by the gas flow is not strong enough to quickly detach or move the attached liquid.

To further illustrate the two-phase interactions, the gas pressure drop across the GC is presented in Fig. 6.3(c). Unlike the water saturation evolution, all three pressure profiles show a rising trend, e.g., the first 24 ms, followed by varying degrees of fluctuation. The initial increase is primarily driven by the formation and growth of pinned droplets on the GC bottom walls (i.e., the GDL/GC interface). The subsequent fluctuations are associated with dynamic interfacial phenomena, including droplet detachment, attachment, merging, collision, separation, and discharge. Among the three cases, the hydrophobic channel shows the fastest pressure rise, peaking at approximately 450 Pa. This behavior is linked to delayed droplet detachment, particularly near the side walls, where droplets tend to accumulate into larger clusters due to weak wall adhesion. These clusters intermittently obstruct the channel, accelerating the pressure build-up. However, as detached droplets are removed more efficiently, the pressure drop subsequently declines earlier, indicating improved water removal. In contrast, the hydrophilic channel shows higher average pressure and more substantial fluctuations, which are caused by slug flow that reduces the adequate gas flow space and increases the likelihood of droplet merging and blockage. The transient pressure peaks observed in Fig. 6.3(c) correspond to sudden water bridge formations during droplet interactions. Representative water morphologies at selected time points (A–F) are illustrated in Fig. 6.3(d).

The two-phase flow simulation results further support the experimental observations. A transition in GC surface wettability from hydrophobic to hydrophilic leads to increased water accumulation and a higher risk of flooding, which may extend into adjacent porous electrodes. In the hydrophilic GC, the pressure drop decreases local gas pressure along the GC, which can potentially hinder reactant gas diffusion driven by pressure and concentration gradients. Furthermore, large fluctuations in pressure drop can cause uneven reactant distribution, thus affecting performance stability and accelerating PEMFC degradation.

6.1.3 GC water injection location

Based on the analysis in Section 6.1.2, two additional questions are considered:
(1) How do different liquid inlet configurations affect the water transport in GCs?
(2) Beyond replacing aged BPP, what alternative strategies can be employed to mitigate the performance decline caused by the BPP wettability transition?

We try to address these two questions from the perspective of water inlets. Three GC liquid inlet configurations, shown in Fig. 5.8, are investigated. Their inlet distributions from one side to the center and then to the opposite side are 10:20:10 (Type I), 0:40:0 (Type II), and 20:0:20 (Type III), respectively. Only hydrophilic GC is taken into account for different liquid inlets.

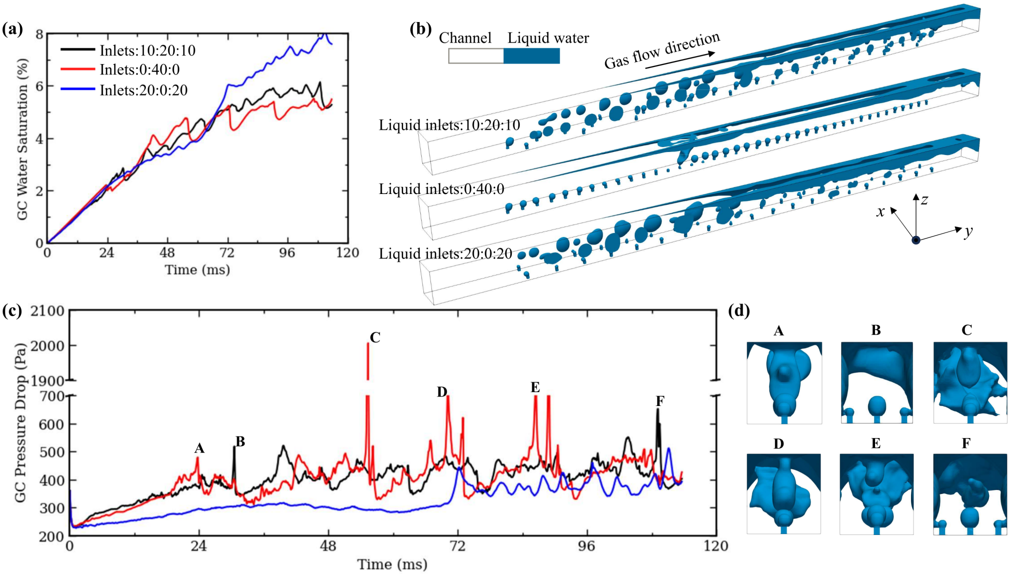

Figure 6.4: (a) Liquid flow evolution in GCs with three different liquid inlet configurations (With the number of inlets varying sequentially from one side to the middle and then to the other side, following the distributions 10:20:10, 0:40:0, and 20:0:20). (a) Time-dependent total GC water saturation. (b) Water distribution at 108 ms. (c) Time-dependent total GC gas pressure drop. (d) Water distribution viewed from the GC inlet at various time points (A, B, C, D, E, F) corresponding to those in subfigure (c).

Figure 6.4(a) shows comparable water saturation variation in the three GCs following the water injection. After a certain time, the difference among them becomes larger. Type I leads to a moderate saturation level. On the other hand, the GC with Type III inlets shows ongoing water accumulation at the end of the simulation. Although statistical stabilization has not yet been reached, it is expected to occur within an extended simulation time. According to Fig. 6.4(b), all three cases form slug flows at 108 ms. Due to the narrow and linear shape of the Type II inlets, detached droplets near the channel entrance easily merge with unseparated droplets, promoting their separation from the bottom surface. Once initiated, this forced detachment mechanism repeats until the merged droplets reach a critical size. At this point, they either adhere to the top wall and contribute to slug formation or pass over smaller downstream droplets and are discharged. Conversely, Type III inlet design promotes droplet adhesion to the side walls, where spherical droplets slowly move along the side walls. Over time, these droplets coalesce, eventually forming a slug flow near the channel outlet. This design leads to more water accumulation in the GC, increasing the flood risk. Nevertheless, this design shows a considerably small pressure drop without strong fluctuations, as shown in Fig. 6.4(c). In comparison, the Type II inlet configuration shows a larger pressure drop from the initial drainage, accompanied by huge transient pressure drop peaks.

In response to question (1), the liquid inlet configuration significantly influences water saturation and transport behavior, thereby strongly affecting gas pressure drop. At the same time, specific fundamental trends remain unchanged. For example, hydrophilic GCs consistently show higher water saturation and slug flow formation, regardless of the inlet type. Moreover, the comparison between the two extreme configurations, Type II and Type III, indicates that water transport characteristics can be regulated by shifting the liquid breakthrough positions within the GDLs. This adjustment can be achieved through techniques such as laser perforation, which has been explored experimentally [200, 201] and numerically [202, 203] to enable more precise control of water management in GDLs.

To more clearly illustrate the possibility of adjusting the GC inlets, a numerical study has been performed on the perforation of the GDL connected to the GC. Figures 6.5(a-b) present the water distribution and breakthrough locations in GDLs with and without perforation. It is shown that the introduction of perforations noticeably influences water transport within the GDL. In the original GDL, water breakthrough primarily occurs near the central region. By contrast, in the perforated GDL, breakthrough is localized at the perforation locations, indicating that liquid inlet distribution can be spatially controlled. This suggests a promising strategy for directing water flow and managing breakthrough locations to improve water removal in fuel cells. Notably, it was found that the water breakthrough frequency among the five perforations was different. This finding aligns with the previous results that, even under simultaneous water injection from multiple inlets, two-phase flow interactions in the GC introduce increasing randomness in breakthrough and droplet detachment over time [68, 70–72, 99]. As a result, the initial differences in breakthrough frequency across perforations may impact long-term flow behavior. Further investigation is needed to assess the implications of these findings for water transport stability and drainage efficiency in practical fuel cell operations.

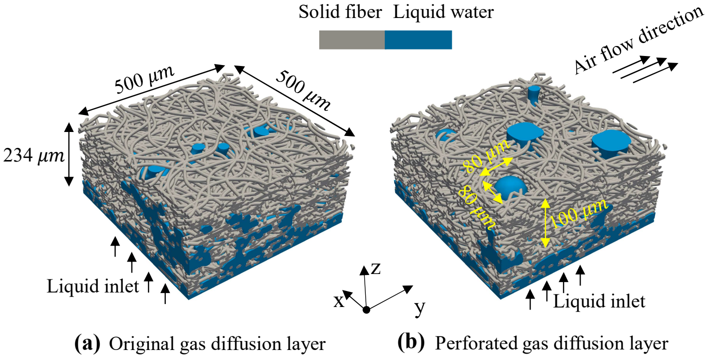

(a) Original gas diffusion layer **(b)** Perforated gas diffusion layer

Figure 6.5: Water breakthrough in GDLs with and without perforation at 3.5 ms. A numerically reconstructed GDL with dimensions of 500 μm × 500 μm × 234 μm and a porosity of 0.7 is modified by adding five 80 μm × 80 μm × 100 μm cuboid holes. These holes match the liquid inlet dimensions used in the previously discussed VOF simulations.

6.2 Two-phase flow in GDL and GC assembly

This section summarizes the main findings from Papers II, III, IV, and V, focusing on two-phase flow behavior in the combined GDL and GC domains. It begins with examining GDL liquid injection strategies, followed by parametric studies that address the effects of fiber diameter, fiber curvature, and additive content on water behavior. It concludes with investigating water-gas interaction under conditions with and without GDL gas outlets.

6.2.1 Evaluation of GDL liquid injection

Two-phase flow simulations in GDLs or GDL/GC assemblies typically require liquid injection from the GDL surface. Building on the classification of inlet configurations introduced in Chapter I, I first evaluate the impact of five representative designs on water transport behavior, ranging from full-area to localized inlets with varying shapes and sizes, as shown in Fig. 6.1.3, named from Type A to Type E. Figure 6.6 presents an overhead visualization of the three-dimensional water flow evolution within the image-based reconstruction of a Freudenberg H2315 GDL, utilizing the five inlet types. To ensure consistency across all cases, the mass flow rate remains constant, with the liquid injection velocity adjusted according to Equation 3.26. Several observed water transport stages in GDLs are concluded: invading, in-plane and through-plane advancing, and breaking through. During the breakthrough, water inside GDLs shows a slight receding behavior, which will be discussed later.

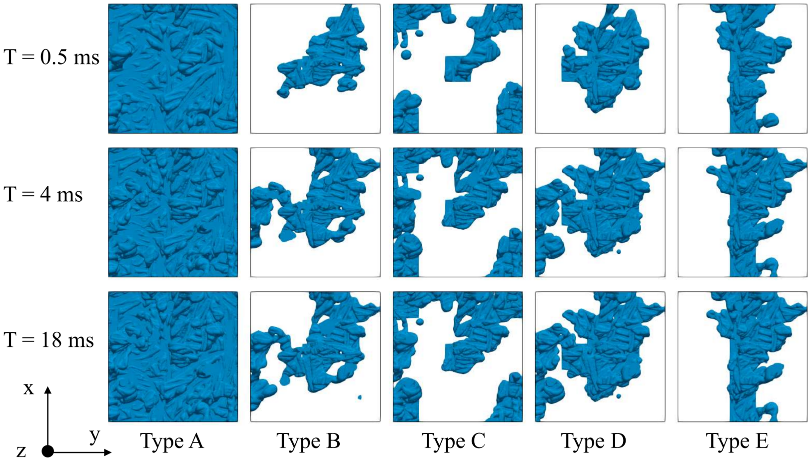

Figure 6.6: Overhead visualization of the three-dimensional water flow evolution (blue color), projected onto the x-y plane, for various liquid inlet configurations at 0.5 ms, 4 ms, and 18 ms. The inlet configurations are defined as follows, Type A: a fully open liquid inlet; Type B: a single central inlet block; Type C: five inlet blocks arranged with one at the center and four at the corners; Type D: a cross-shaped arrangement with five inlet blocks centered; and Type E: a linear arrangement of five inlet blocks along the x-direction.

The results in Fig. 6.6 indicate that liquid transport and distribution strongly depend on the selection of liquid inlet configuration. Among all cases, water initially covers the entire invading region and then preferentially flows through large pores, demonstrating an irregular concave-convex distribution. As it continues to rise, the water content tends to decrease. All these features suggest that the water transport in GDLs is dominated by the capillary fingering pattern, aligning with the previous findings by Zhang *et al.* [188]. Under localized liquid inlets, water primarily propagates around the invading region. Notably, the GDL with Type B injection demonstrates a slightly broader spreading pattern compared with that with Type C. This difference is likely attributed to the increased liquid velocity. However, the water distribution in GDLs with localized inlets shows concave–convex features similar to those observed with full inlets in local regions. This suggests that accelerating the liquid velocity has only a limited effect on the two-phase flow transport pattern.

Figures 6.7(a-b) show the time evolution of total water saturation and capillary pressure in the GDLs with five different inlet configurations. In all cases, both quantities rise rapidly at early times and gradually stabilize, with varying degrees of fluctuation. The maximum differences in steady-state water saturation and capillary pressure across the cases are approximately 33% and 16%, respectively. Among them, the Type A inlet leads to the highest water saturation and the lowest capillary pressure, which is attributed to a greater probability of water penetrating through larger pores with reduced flow resistance. Although the Type C, D, and E inlets share the same injection area and mass flow rate, notable differences are observed among them exclusively due to the variation in inlet location.

Figure 6.7(c) shows the through-plane local water saturation at the end of the simulation (18 ms). For the Type A injection, water saturation drops sharply from 1 in the invasion region, followed by a more gradual decline. In contrast, the saturation profiles of Types C, D, and E show varying trends between the injection and breakthrough regions, reflecting the influence of the heterogeneous pore structure. Additionally, as shown in Fig. 6.6, the more pronounced lateral spreading behavior associated with Type B injection results in an initial increase in through-plane saturation before it follows a similar declining trend to that observed with Type C.

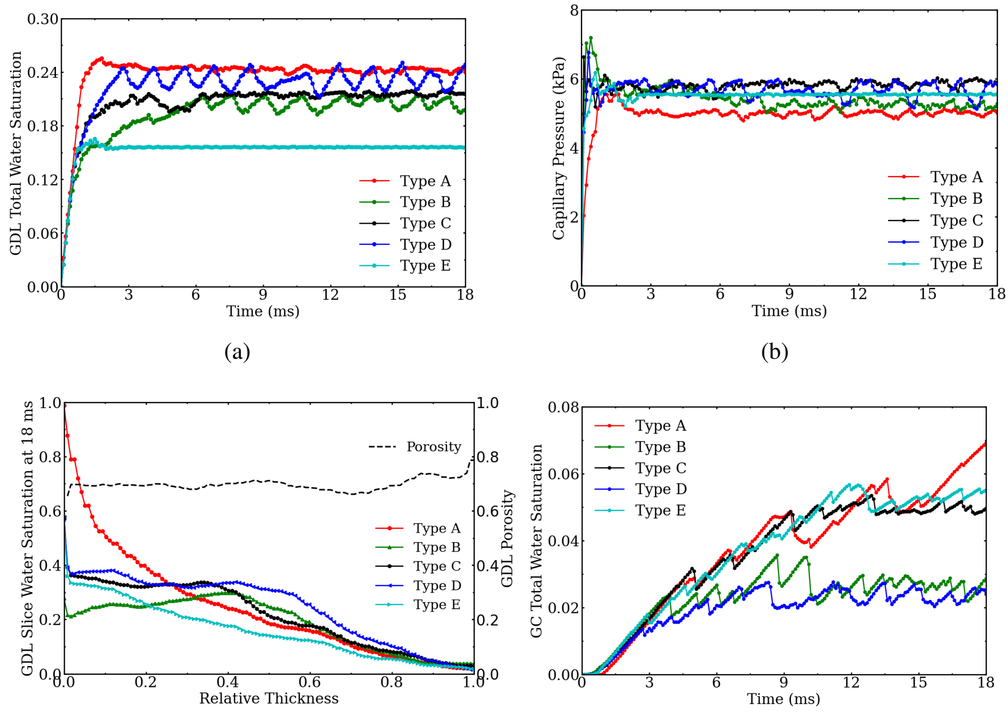

(a)

(b)

(c)

(d)

Figure 6.7: Time-varying GDL (a) water saturation, (b) capillary pressure. (c) through-plane local water saturation at 18 ms. (d) Time-dependent total water saturation within GC, which is calculated based on the part above GDL along the airflow direction.

Figure 6.7(d) shows the time-varying total GC water saturation relating to the connected GDL structures. The spatial evolution of water distribution within the GC following breakthrough is illustrated in Fig. 6.8. For GCs associated with Type A, C, and E inlets, water mainly accumulates in a single corner, forming slug flow and leading to a sustained rise in saturation. Type A, in particular, displays a continuous increase throughout the simulation, driven by the gradual formation of an attached film along the sidewall. In contrast, Types B and D reach a steady saturation earlier and maintain comparatively lower levels. These results highlight that the inlet configuration in the GDL strongly affects water transport and breakthrough behavior, which in turn governs downstream distribution in the GC. The flow regimes observed are governed by a combination of breakthrough characteristics (location, number, and size), detachment dynamics (interface position and droplet size), and attachment modes (none, single-side, or double-side attachment).

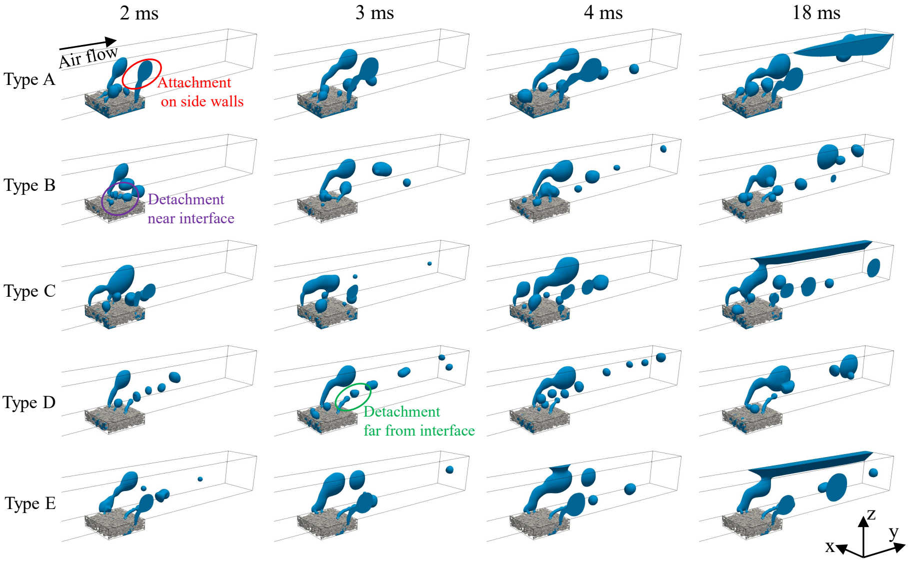

Figure 6.8: GC water distribution (blue color) corresponding to Type A-E liquid injections at 2 ms, 3 ms, 4 ms, and 18 ms.

Despite simplifications of the full-area liquid injection, it remains widely used in previous studies [73, 79, 88, 90] due to its effectiveness in providing a relatively consistent framework for evaluating water transport mechanisms. Most existing work focuses on water behavior under varying structural, material, and operational conditions. The advantage of full-area injection is particularly apparent when comparing different GDL structures, as it eliminates the variability introduced by inlet location. However, localized injection can lead to significant internal variations within the same GDL, complicating comparative analysis. For this reason, full-area injection is adopted in Papers II, III, and V. To improve statistical reliability, multiple GDL samples generated with similar reconstruction procedures need to be tested. Nonetheless, to address potential overestimation of water retention, future work may consider supplementary cases involving gas counter-flow or localized injection, offering a more representative evaluation of GDL drainage capacity.

6.2.2 Effect of fiber diameter

This section summarizes the effect of varying fiber diameter on water transport in GDLs and GCs. Three cases with varying GDL fiber diameters, $d = 10\ \mu$m (Case d10), 15 μm (Case d15), and 20 μm (Case d20), have been studied. Figure 6.9(a) shows the temporal variation of water distribution inside three GCs. Increasing the fiber diameter promotes the water breakthrough from GDLs, e.g., at 6 ms. Once a water breakthrough occurs in the central region, water continues to accumulate as droplets, which detach upon reaching a critical size. On the other hand, when water breaks through near the wall, it rapidly adheres to the hydrophilic surface and forms a water bridge at the GDL/GC interface, connecting the water in the GDL and the water on the wall. However, this water connection can be broken (e.g., Case d10) or maintained for a long time (e.g., Case d20). During this process, the water interface deforms under the competing effects of drag and surface tension forces. It is observed that increasing the fiber diameter promotes the formation of a more continuous slug flow for removal, as seen when comparing Case d10 and Case d20 at 21 ms.

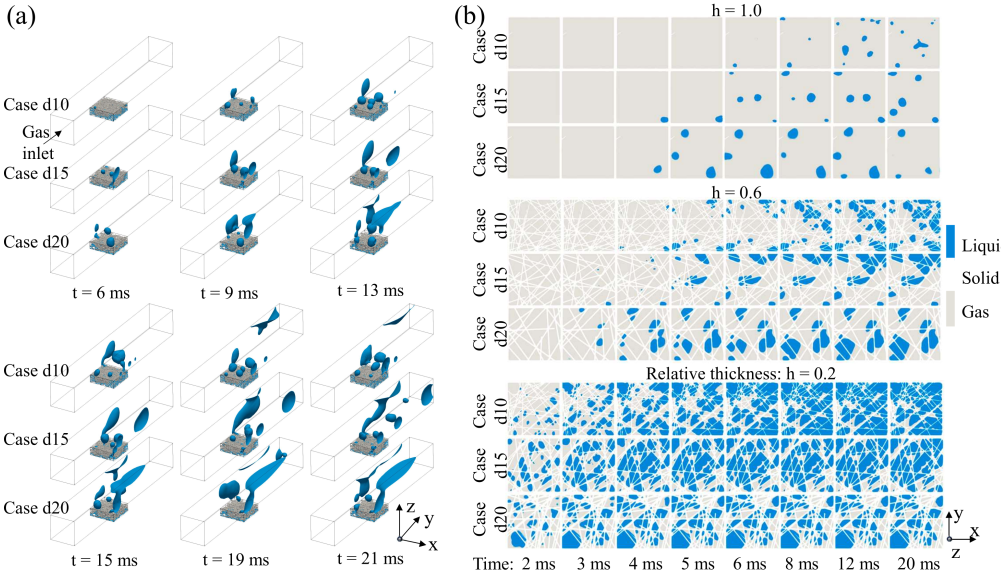

Figure 6.9: (a) Water spatial distribution in three GCs at 6 moments, shown by the form of isosurface of $\alpha = 0.5$. (b) In-plane water distribution of three GDLs at three relative thicknesses ($h = 0.2, 0.6, 1.0$) and different moments.

Figure 6.9(b) presents the in-plane water distribution of three GDLs at three relative thicknesses ($h = 0.2, 0.6, 1.0$) and different time steps. $h = 0.2$ is a position close to the water injection. A decreasing trend of water retention from the water injection area to the breakthrough area can be seen in all GDLs. Over time, the in-plane water distribution below $h = 1$ shows a stable trend, while that at $h = 1$ changes randomly due to the water breakthrough and droplet detachment. At a given relative thickness, increasing fiber diameter leads to earlier water emergence and higher steady-state water content. Moreover, both the water breakthrough time and stabilization time tend to be advanced. Specifically, as the fiber diameter increases, the reconstructed GDL has an increased number of large pores, which ultimately contributes to the larger water clusters, e.g., Case d20. At $h = 1$, the water distribution shows instability, characterized by the appearance, disappearance, reduction, and increase of water clusters. Decreasing fiber diameter tends to increase the number of water clusters, but with a decrease in size, indicating an increase in the potential breakthrough sites.

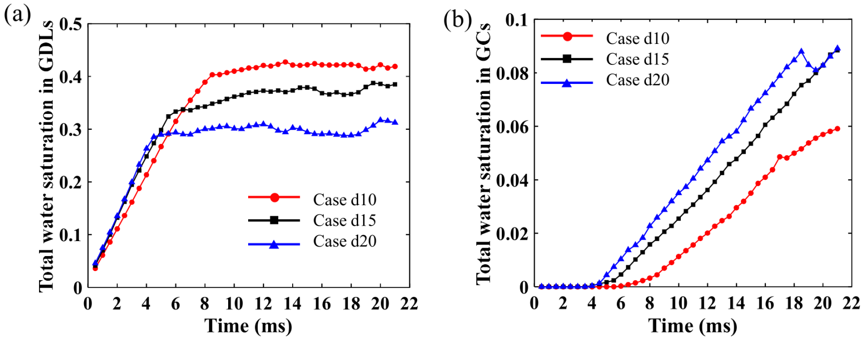

Figure 6.10: Comparison of the time-varying total liquid water saturation in GDLs and GCs for three cases. (a) In GDLs. (b) In GCs.

Figure 6.10 shows the time-dependent total water saturation in both the GDL and GC regions. In the GDL, Case A shows the lowest saturation throughout, whereas Case C stabilizes first at approximately 0.30, followed by Case B at around 0.37. These results suggest that smaller fiber diameters slow water transport through more tortuous pathways and smaller pores, leading to higher overall saturation. The final saturation values (0.30-0.45) are consistent with earlier studies [90, 204]. After the breakthrough, GC saturation increases in three GDLs, with Case C exhibiting the highest values until 18.5 ms, after which the discharge of a large droplet detachment causes a rapid drop. The saturation then follows a similar trend to Case B. Case A remains consistently lower due to a delayed breakthrough.

6.2.3 Effect of fiber curvature

The effect of fiber curvature on the GDL two-phase flow transport is almost unknown. In this section, a comparative analysis of water transport in randomly reconstructed GDLs under nearly identical conditions is presented for the first time, while taking into account the effect of the fiber curvature. Three types of GDLs, denoted as S-GDL, C1-GDL, and C2-GDL, have been reconstructed using straight, moderately curved, and highly curved fibers, respectively. Four samples were generated for each GDL type to improve the statistical representativeness of the results. The water saturation and capillary pressure for each sample are presented in Paper III, while the ensemble-averaged values are shown in Fig. 6.11.

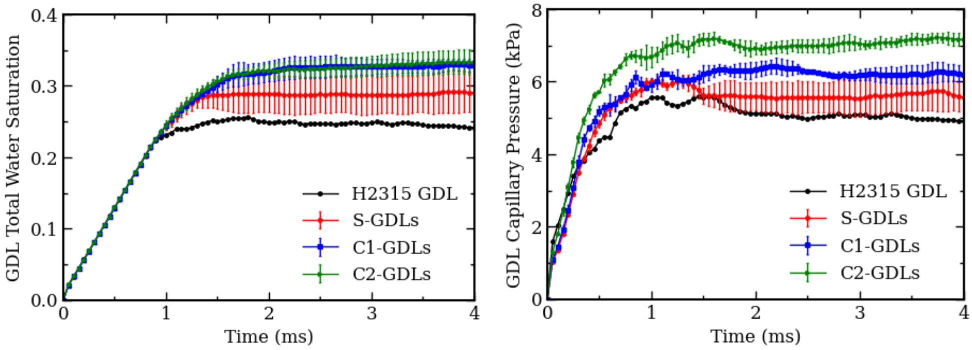

(a) (b)

Figure 6.11: Ensemble average time-dependent water saturation and capillary pressure in the GDLs with three distinct fiber curvatures in 4 ms. The simulation results based on a physical GDL H2315 are used for comparison.

The four S-GDL samples show apparent variations in water saturation and capillary pressure, with maximum deviations of 17% and 19%, respectively. Their average values are consistently lower than those of the C1-GDL and C2-GDL samples. As fiber curvature increases, the variation in saturation and capillary pressure across samples decreases, reflecting more uniform drainage performance. Although the C1-GDL and C2-GDL sets result in similar average saturation levels, capillary pressure differs significantly between them. Despite all reconstructed GDLs sharing a comparable through-plane local porosity distribution, both water retention and capillary pressure tend to increase with fiber curvature. Moreover, all reconstructed GDLs produce higher water saturation and capillary pressure than the reference Freudenberg H2315 GDL, indicating that further improvements in reconstruction methodology are required to more accurately replicate realistic GDL behavior.

To explore the reasons behind the above findings, we plotted the water distribution and filtered pore networks of four representative GDL samples in the early stage of invasion and after breakthrough, as shown in Fig. 6.12. The gray, dark purple, and light purple regions represent water saturation at 1 ms, water saturation at 4 ms, and the overlapping water distribution at these two timesteps, respectively. From Fig. 6.11(a), all GDLs show similar water saturation levels at 1 ms, with differences emerging thereafter. The water distribution between 1 ms and 4 ms reveals that in GDL H2315, water rapidly breaks through at multiple locations without significant lateral spreading, leading to faster statistical stabilization. In contrast, as fiber curvature increases, water disperses more extensively within regions containing small pore clusters, prolonging the stabilization of high water saturation levels. Furthermore, the enhanced capillary pressure in Fig. 6.11(b) results from the increased small pores within GDLs of highly curved fibers.

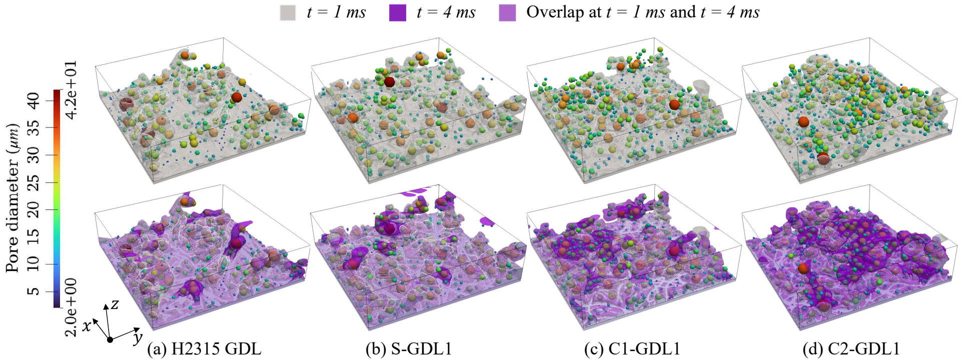

(a) H2315 GDL (b) S-GDL1 (c) C1-GDL1 (d) C2-GDL1

Figure 6.12: Combination of filtered pores and GDL water distribution state at 1 ms (gray surface) and 4 ms (purple surface). The pores are colored according to the pore diameter (see left color bar).

6.2.4 Effect of additive structure

Figures 6.13(a-c) show the normalized values of pores, throats, and coordination numbers for the extracted GDL pore networks, based on total amounts of 3500, 12000, and 3500, respectively. All GDLs have a significant fraction of small pores and throats. By decreasing the number of fibers, i.e., from GDL1 to GDL3, the total number of all three parameters decreases over the entire range of variation, especially in the range of smaller values. By adding binders into GDL2 and GDL3, a further decrease in small pores and throats has been observed, as shown in Fig. 6.13(b), thereby resulting in a much smaller coordination number, namely, worse pore connectivity. A similar trend is also observed when more additives are included in GDL1. Therefore, adding additives will decrease the total number of pores and throats in GDLs, especially the proportion of small pores and throats. As a result, the GDL pore connectivity is reduced.

Figure 6.14 presents the normalized water volume (relative to the GDL bounding box volume, 2.925×10^{-11} μm^3) and the corresponding total water saturation. A direct comparison with their definitions is provided in Eq. 6.1, highlighting their shared parameter, i.e., the water volume inside the GDL. Among the three GDLs without additives, GDL1 contains the most pores and throats but shows the lowest water content, suggesting that smaller pores contribute minimally to water retention. In contrast, GDL3 has the smallest number of pores, yet maintains a comparable proportion of large pores

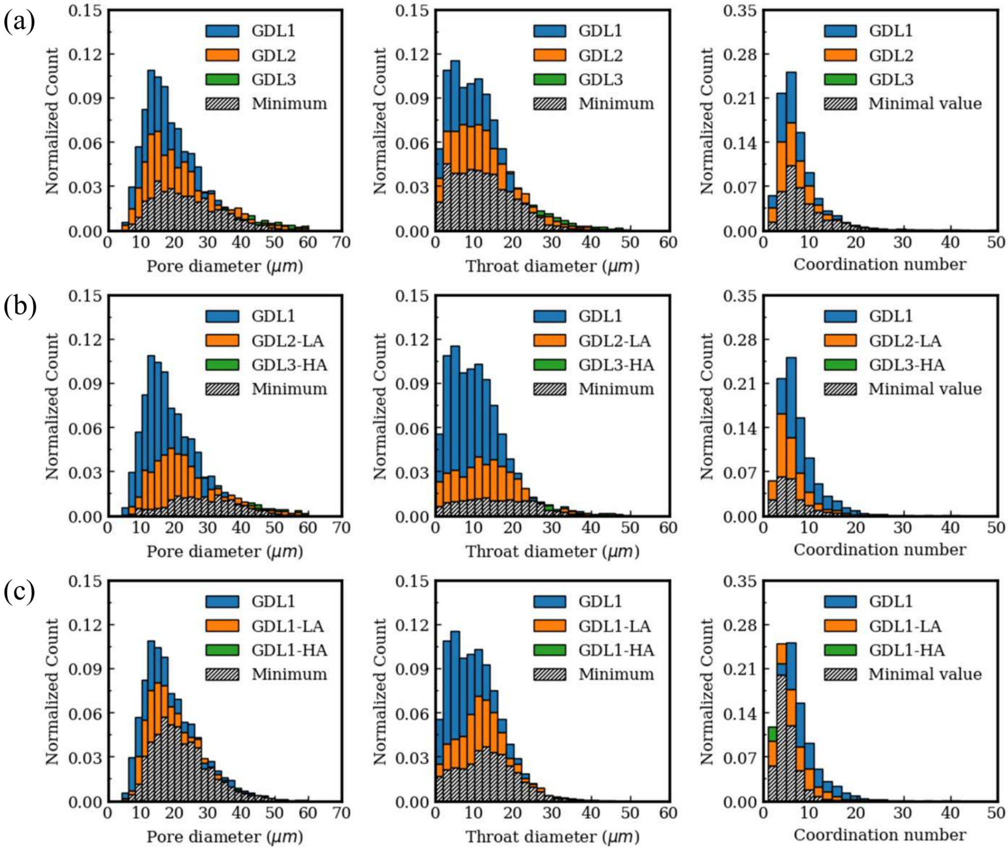

Figure 6.13: The normalized count of pore diameter, throat diameter, and coordination number based on the total count of 3500, 12000, 3500, respectively. (a) Original GDLs, (b) Same porosity but different additive fractions, (c) Decreasing porosity with increasing additive fractions.

relative to the others, which supports its highest water content due to the dominance of water retention in large pores. As shown in Figure 6.14(a-b), the total water volume shows only minor changes upon the addition of additives, even when they occupy over 34% of the solid phase (0.16/0.46), as long as porosity remains constant. Notably, the presence of additives stabilizes the water volume evolution after 1 ms. This stabilization is primarily attributed to the reduced number of small pores, which dampens the water penetration dynamics. Although additives decrease the porosity in GDL1, both GDL1-LA and GDL1-HA demonstrate similar temporal water volume profiles, indicating that the addition of additives has a negligible effect on water volume when the number of large pores remains unchanged. Consequently, previous two-phase flow studies that omit additive structures are unlikely to misrepresent the overall trend of water saturation dynamics. Moreover, conclusions drawn from water saturation comparisons among different GDLs in Papers II and III remain valid. When incorporating additives into GDL models, the updated water saturation can be approximately adjusted using the ratio of the new to the original pore volume while preserving the trend, as formulated in Eq. 6.2.

$$\hat{V}_{water} = \frac{V_{water}}{V_{ref}}, S_{water} = \frac{V_{water}}{V_{pore}} \tag{6.1}$$

$$S_{water,new} = \frac{V_{water,new}}{V_{pore,new}} \approx \frac{V_{water,old}}{V_{pore,new}} = S_{water,old} \frac{V_{pore,old}}{V_{pore,new}} \tag{6.2}$$

Figure 6.14(d-f) shows the total water saturation in the five GDL samples. The higher porosity in GDL2 and GDL3 has slowed down the saturation buildup; however, the final water saturations observed across these three GDLs have converged to similar values, which warrants further investigation to determine whether this similarity is coincidental. Thereafter, water saturation evolves with porosity changes introduced by additives. Given that the overall water volume in a GDL remains relatively unchanged before and after additive incorporation, a reduction in porosity due to additive addition results in higher water saturation and a more rapid increase in saturation, as demonstrated in Fig. 6.14(e–f).

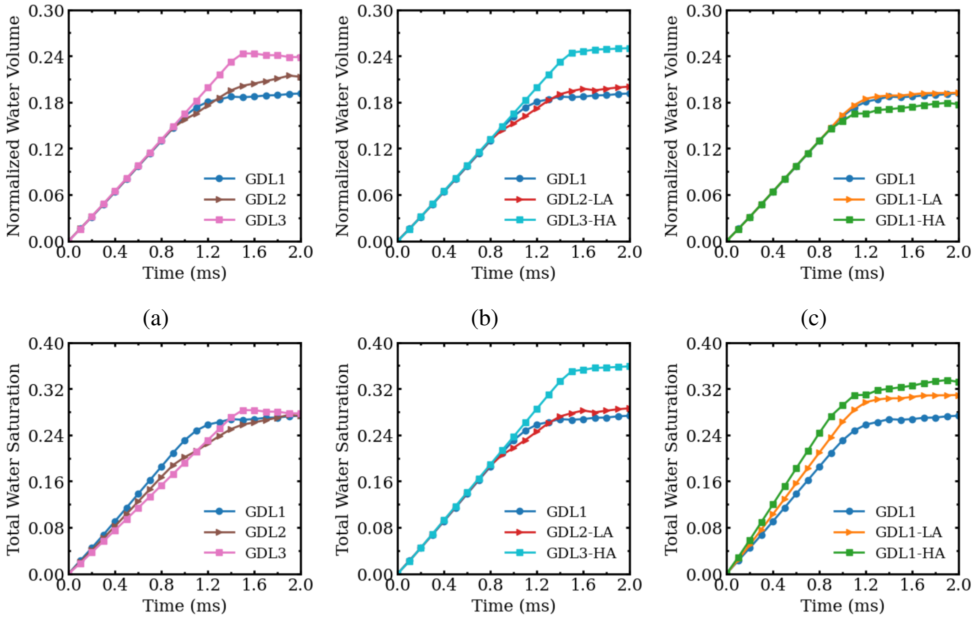

(a) (b) (c)

(d) (e) (f)

Figure 6.14: Normalized water volume and total water saturation at different conditions: (a) varying the number of fibers; (b) keeping the same porosity; (c) keeping the same GDL base but increasing additives.

Figure 6.15 presents the variation in capillary pressure during the water intrusion process. GDL1, GDL1-LA, and GDL1-HA show similar magnitudes and trends in their capillary pressure profiles. A comparable behavior is also observed for the pairs GDL2 and GDL2-LA, as well as GDL3 and GDL3-HA. These observations suggest that capillary pressure is predominantly governed by the intrinsic fibrous pore structure of the GDLs, while the presence of additives exerts only a minor influence. Combined with pore network analysis, it is found that the high capillary pressure in GDL1 is primarily attributed to its large fraction of small pores, as predicted by the Young–Laplace equation.

A comparison between GDL3 (highest porosity) and GDL1-HA (lowest porosity) underscores the importance of pore connectivity. Only small pores that are well-connected within water transport pathways contribute significantly to capillary pressure. For example, GDL1-HA exhibits better connectivity than GDL3, facilitating water transport through small pores. Additionally, introducing a low additive volume fraction (0.08) has minimal impact on capillary pressure, as seen in GDL1 vs. GDL1-LA and GDL2 vs. GDL2-LA. In contrast, a higher additive volume fraction (0.16), as in GDL1-HA and GDL3-HA, results in a slight increase in capillary pressure compared to their unmodified counterparts.

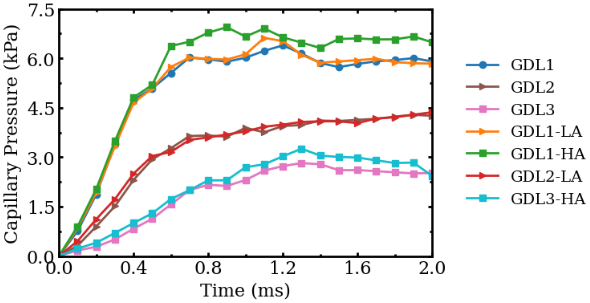

Figure 6.15: Capillary pressure variation within different GDLs.

6.2.5 Investigation on GDL water-gas counterflow

During PEMFC operation, water-gas counterflow naturally occurs in the GDL due to opposing transport directions of drainage water and incoming reactants. Most previous VOF simulations in GDLs have primarily focused on the liquid phase, while the gas outflow is often neglected. This section examines whether the presence of gas-phase counterflow toward the reaction region affects the liquid transport behavior within the GDL. To apply boundary conditions for liquid inflow and gas outflow, the Type F configuration (Fig. 5.9) is adopted. Unlike the Type B setup, the four corner outlets of the Type F domain utilize totalPressure, zero gradient of liquid volume fraction ($\nabla \alpha_l = 0$), and zero normal gradient of velocity ($\nabla \mathbf{U} \cdot \hat{\mathbf{n}} = 0$). Figure 6.16 compares water distributions in the GDLs under Type B and Type F conditions. While initial invasion behavior is similar, the two cases deviate over time. In the Type B case, water gradually spreads toward the boundary wall, as highlighted by the red dashed rectangle, whereas in the Type F case, such spreading is suppressed. Consequently, Type B results in higher and more fluctuating water saturation (Fig. 6.17(a)), along with slightly lower capillary pressure (Fig. 6.17(b)). The observed oscillations in the Type B case beyond 6 ms are attributed to receding and advancing movements within the GDL during breakthrough. This behavior is also significantly weakened in Type F, indicating that the water distribution marked in Type B is the leading cause of the periodic fluctuations.

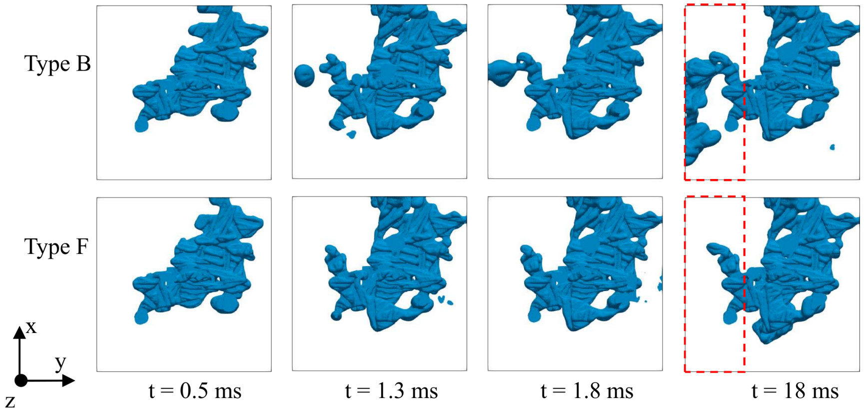

Figure 6.16: Overhead view (perpendicular to the x-y plane) of water distribution evolution in Type B and F GDLs.

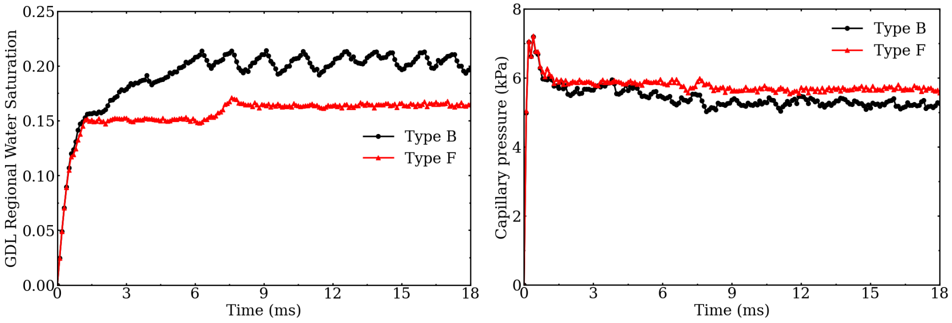

(a) (b)

Figure 6.17: Comparison between Type B and F GDL time-varying total water saturation level and capillary pressure.

To gain further insight, the GDL is divided into two sub-regions, namely Region Q1 and Q2. As shown in Fig. 6.18(a-d), the key difference between the two cases is primarily associated with Region Q1, while both Region Q2 show comparable water saturation and capillary pressure. A consistent trend is observed in both regions, e.g., higher water saturation corresponds to lower capillary pressure. In Region Q1 of the Type B inlet, water content increases rapidly, accompanied by a sharp decline in capillary pressure, which later fluctuates within a limited range. Conversely, Region Q1 in the Type F case maintains a higher and more stable pressure profile. Further investigation is needed to understand the suppression mechanism of water behavior in Region Q1 associated with Type F water ingress. In addition, it is necessary to determine whether the differences caused by the inclusion of the air outlet boundary condition persist in other GDL configurations, that is, whether there is a geometry dependency. The sudden rise in water saturation in Region Q2, as shown in Fig. 6.18(c), is attributed to newly advancing water in small pores during the water breakthrough process.

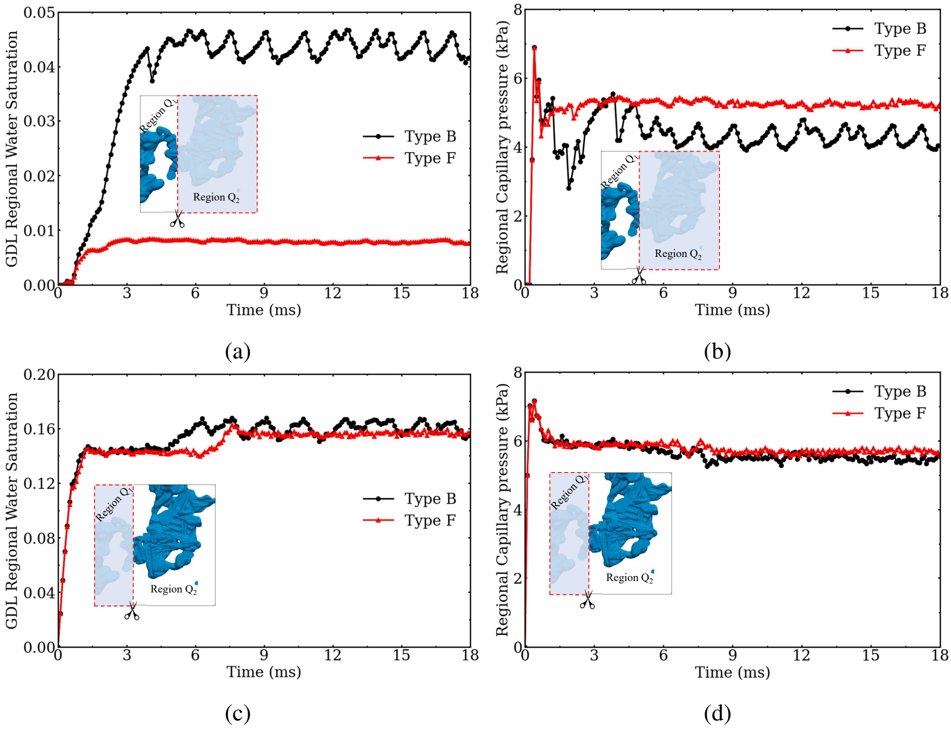

(a)

(b)

(c)

(d)

Figure 6.18: Comparison between Type B and F GDL time-varying regional water saturation level and capillary pressure.

Figure 6.19 further illustrates the streamlines and water distribution in the GDL and above GC region at 4 ms. Under Type B configuration, the gas velocity streamlines terminate or change direction near the GDL bottom due to the imposed wall boundary condition, resulting in a more chaotic and dispersed flow pattern. In contrast, Type F shows closely spaced streamlines converging toward the four bottom corners of the GDL, accompanied by higher velocity magnitudes. Consequently, the gas flow structure in Type F is more organized compared to the random and irregular pattern observed in Type B.

These variations in gas flow significantly impact liquid distribution within both the GDL and GC. In addition to the distinct water accumulation in the GDL, as discussed earlier, water behavior in the GC also differs, particularly in terms of droplet breakthrough and detachment dynamics. Once liquid enters the GC, the airflow influences its detachment and transport, simultaneously altering the gas flow pathways above the GDL/GC interface. Depending on local conditions, airflow may either accelerate or become obstructed as it enters the GDL, further amplifying differences in gas dynamics.

The effect of boundary conditions on two-phase interactions is evident, yet the complex coupling mechanisms between gas and liquid phases remain unclear. In particular, the dominant phase (liquid or gas) and the governing region (GC or GDL) during interactions require further investigation. Addressing these uncertainties necessitates additional studies in future work.

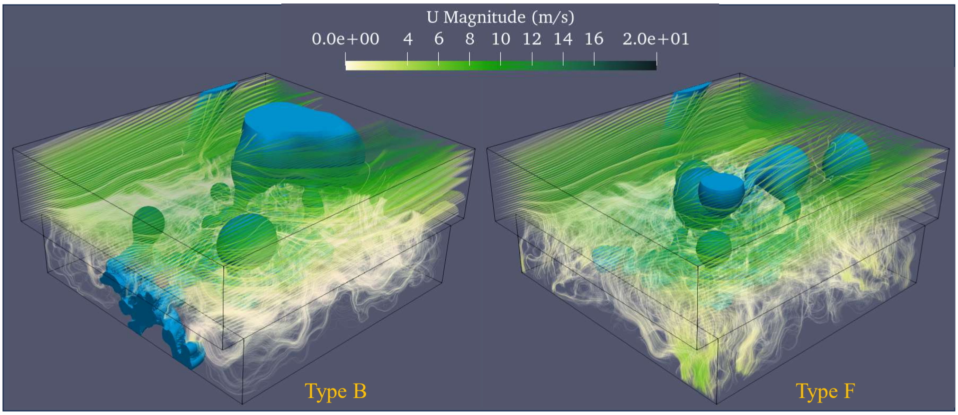

Figure 6.19: Liquid phase distribution (Blue color) and gas phase velocity streamlines (color bar) within GDL and GC of Type B and Type F at t = 4 ms.

Chapter 7

Conclusion and outlook

This chapter summarizes the main findings of my four years of doctoral research and outlines potential directions for future work.

7.1 Conclusion

This thesis has provided an in-depth understanding of the local transport characteristics of water-gas two-phase flow in PEMFCs, with particular emphasis on the influence of surrounding structural features on flow behavior. A series of numerical investigations has been carried out using the VOF method within the OpenFOAM framework. These simulations have considered several critical aspects, including microchannel and porous GDL domains, liquid water injection configurations, GDL fiber diameter and curvature, additive treatment, and the GDL gas outlet boundary condition.

Experimental electrochemical analyses have shown that fuel cell performance degradation is strongly associated with the wettability transition of BPPs from hydrophobic to hydrophilic. Building on this observation, this thesis has carried out two-phase flow simulations in a straight GC with a rectangular cross-section and multiple water inlets. The effects of GC surface wettability and water injection locations on liquid water dynamics have been systematically investigated. In contrast to previous studies with single-point injection, the present simulations reveal additional interfacial behaviors such as forced droplet detachment, droplet collision, and coalescence, which are found to significantly influence flow stability and water transport. Hydrophilic channels tend to accumulate an additional amount of liquid water, forming slug flow that leads to larger pressure drops and stronger oscillations. Sudden spikes in pressure drop frequently result from droplet coalescence. Conversely, hydrophobic GC surfaces help stabilize water saturation and maintain a more uniform gas flow. The combined experimental and numerical findings indicate that hydrophilic surface conditions over time contribute to accelerated fuel cell degradation through persistent water accumulation and unstable pressure behavior. Notably, even under hydrophilic conditions, positioning all water inlets near the GC sidewalls results in higher water saturation but significantly smoother and lower pressure drops, due to fewer droplet mergers in the central region. This insight aligns with earlier studies employing perforated GDLs to optimize water injection and underscores the critical role of GC flow patterns in long-term PEMFC performance. Overall, tuning surface wettability and injection configuration has emerged as a promising strategy for improving water management and mitigating performance loss in PEMFCs.

Furthermore, the simulation framework has been extended to a T-shaped GDL and GC domain, enabling the investigation of coupled water-gas transport phenomena across the GDL and GC interface. Porous fibrous GDL structures have been stochastically reconstructed using in-house code. Straight and curved fiber generation, additive structure, bulk and local porosity, along with random and layer-by-layer fiber stacking strategies, have been implemented to generate representative GDL morphologies. This modeling capability provides a valuable platform for future studies aiming to link GDL microstructure to fuel cell performance and to support the rational design of advanced GDL materials. From the two-phase flow simulations of these GDLs, the observed liquid water transport process can be summarized as: invading, advancing, and breaking through the GDL, followed by growing, deforming, separating, attaching, colliding, merging, and being removed from the GC. It is noted that these behaviors in GCs can be disordered. Compared with the previous studies, which separately considered only GDLs or GCs, a water receding behavior inside the GDL occurs during water breakthrough because of the release of capillary pressure. Moreover, the size of the water breakthrough near the GDL/GC interface varies over time, indicating that a dynamic boundary condition for the GC simulations is required.

The effect of carbon fiber geometry and additive inclusion on two-phase flow behavior has been systematically investigated, which has received limited prior attention. Even when maintaining constant porosity, pore network analyses have revealed that structural modifications in the GDL inevitably alter pore size distribution and connectivity, thereby influencing capillary-driven water transport. Larger fiber diameters create larger pores that enhance drainage and reduce water saturation in the GDL; however, they may also promote faster water accumulation in the connected GCs, suggesting a water management trade-off between adjacent components. Increased fiber curvature has been found to introduce an increased number of small pores and improve pore connectivity, yet at the cost of higher water retention. However, GDLs with curved fibers exhibit more uniform water saturation compared to those with straight fibers, indicating enhanced structural robustness against stochastic variation. The incorporation of additive structures, especially at high content, reduces the number of small pores and diminishes pore connectivity, thus significantly altering water behavior. Nonetheless, low additive content has minimal impact under highly hydrophobic conditions. Capillary pressure is found to be related to the initial fibrous skeleton structures before incorporating additives. These findings suggest that a well-balanced combination of additive content and fiber skeleton porosity can offer improved drainage performance while preserving mechanical stability.

Porosity has long been regarded as a key parameter in characterizing porous GDLs for macro-scale PEMFC simulations. However, the present study has demonstrated that maintaining constant porosity alone does not ensure consistent two-phase flow behavior, such as water saturation and capillary pressure, due to intrinsic structural heterogeneity. In contrast, GDL structures with different porosity levels but the same partial fiber skeleton can exhibit comparable water saturation behaviors. These findings highlight that beyond bulk porosity, the internal microstructural attributes, such as pore size, spatial distribution, and connectivity, play a crucial role in determining water transport characteristics. Future modeling and design efforts should therefore account for these microscopic features to predict and optimize GDL performance accurately.

The water inlet and gas outlet conditions at the GDL surface close to the reaction region have been investigated. Various locations and sizes of water inlets contribute to the distinct water saturation and local water advancing and receding behavior in a particular area. Such uncertainty challenges the evaluation of GDL drainage capacity. To minimize the influence of localized inlets, a full-area water injection strategy is recommended for evaluating GDL drainage capacity under consistent conditions. Nevertheless, where numerical or experimental setups allow, future studies incorporating controlled localized injections may offer deeper insights and contribute to a more comprehensive understanding of local water transport phenomena. An air outlet boundary condition at the GDL/electrode interface for interface-resolved two-phase flow simulations is a problematic issue that has not been addressed by previous studies. In this thesis, our purpose is to provide one solution to show the different liquid-gas interactions with the presence of air outlets and then to attract more attention from peer researchers to think further and offer better solutions in this direction. This is not the final step; a more realistic air outlet boundary condition that accounts for electrochemical reactions, coupled with an interface-capturing method, is essential for accurate simulation.

7.2 Outlook

This thesis has provided valuable insights into water transport in GDLs and GCs through VOF simulations. However, there is still a gap between the current numerical findings and their application in practical PEMFC systems. Future research should focus on enhancing the realism, accuracy, and predictive ability of simulation models to better represent actual operating conditions and support more effective fuel cell design.

While the present study has mainly explored the sensitivity of water behavior to key structural and operational parameters, optimal strategies for water management have not been pursued. Achieving this would require integrating additional GDL features, such as thermal and electrical conductivity, gas transport resistance, and flow uniformity, into a unified multiphysics framework.

Moreover, future simulations should incorporate more complex operating conditions, including electrochemical reactions, humidity control, and temperature gradients. These factors are essential in governing water transport and phase-change dynamics but are not fully captured under the current simplified conditions. Incorporating membrane water transport models and evaporation–condensation mechanisms, possibly through hybrid modeling approaches, could significantly improve simulation fidelity.

Reliable validation remains a crucial bottleneck for GDL two-phase simulations. Despite their flexibility and depth, numerical models must be benchmarked against high-quality experimental data. Coordinated efforts to generate shared databases under controlled and consistent conditions would greatly facilitate cross-validation and enhance confidence in model predictions. Establishing an open-access platform for experimental–numerical data exchange is strongly encouraged.

Stochastic microstructure reconstruction has proven effective in capturing GDL heterogeneity and its influence on water behavior. Nonetheless, current geometry-based methods require further refinement to better reflect real GDL morphologies. Looking ahead, machine learning-assisted structural design, particularly data-driven generation of physical GDL structure, holds promise for accelerating parameter studies and structure-performance optimization.

A promising research direction could be the control of surface properties for enhanced water management. The interplay between BPP and GDL hydrophobic/hydrophilic patterns and channel geometry remains insufficiently understood. Future work could investigate how spatially controlled wettability or advanced micro-patterned designs enable self-regulating water pathways, mitigating flooding while maintaining sufficient membrane hydration. These studies will also help reduce the utilization of per- and polyfluoroalkyl substances (PFAS) in PEMFC components.

References

[1] United Nations Framework Convention on Climate Change (UNFCCC). Paris agreement: Report of the conference of the parties to the united nations framework convention on climate change. https://unfccc.int/process-and-meetings/the-paris-agreement, 2015. Accessed: 12th November 2024.

[2] J. Lincoln. *Carbon, Confusion and Conflict: Global Governance Implications of the Net-Zero Energy Transition*. Routledge India.

[3] World Meteorological Organisation (WMO). WMO confirms that 2023 smashes global temperature record. https://wmo.int/media/news/wmo-confirms-2023-smashes-global-temperature-record, 2024. Accessed: 12th November 2024.

[4] E. Qu, X. Hao, M. Xiao, D. Han, S. Huang, Z. Huang, S. Wang, and Y. Meng. Proton exchange membranes for high temperature proton exchange membrane fuel cells: Challenges and perspectives. *Journal of Power Sources*, 533:231386, 2022. doi: https://doi.org/10.1016/j.jpowsour.2022.231386.

[5] E. R. Management. The fuel cell industry review 2022. https://www.erm.com/contentassets/55c43361e857413387f28fbacea6e91a/the-fuel-cell-industry-review-2022.pdf, 2022. Accessed: 12th November 2024.

[6] The U.S. Department of Energy. Hydrogen and fuel cell technologies office, department of energy. 2019. URL https://www.energy.gov/eere/fuelcells/fact-month-april-2018-fuel-cell-cost-decreased-60-2006. Accessed: 12th November 2024.

[7] The U.S. Department of Energy. 2024 annual merit review and peer evaluation report, 2024. URL https://www.hydrogen.energy.gov/library/annual-review/2024-annual-merit-review-and-peer-evaluation-report. Accessed: 12th November 2024.

[8] P.-Y. A. Chuang, M. A. Rahman, F. Mojica, D. S. Hussey, D. L. Jacobson, and J. M. LaManna. The interactive effect of heat and mass transport on water con-

densation in the gas diffusion layer of a proton exchange membrane fuel cell. *Journal of Power Sources*, 480:229121, 2020. doi: https://doi.org/10.1016/j.jpowsour.2020.229121.

[9] T. A. Trabold. Minichannels in polymer electrolyte membrane fuel cells. *Heat Transfer Engineering*, 26(3):3–12, 2005. doi: https://doi.org/10.1080/01457630590907149.

[10] M. Andersson, S. B. Beale, M. Espinoza, Z. Wu, and W. Lehnert. A review of cell-scale multiphase flow modeling, including water management, in polymer electrolyte fuel cells. *Applied energy*, 180:757–778, 2016. doi: https://doi.org/10.1016/j.apenergy.2016.08.010.

[11] J. Li, Y. Ke, W. Yuan, Y. Bai, B. Zhang, Z. Lin, Q. Liu, Y. Tang, and others. Enhancement of two-phase flow and mass transport by a two-dimensional flow channel with variable cross-sections in proton exchange membrane fuel cells. *Renewable Energy*, 219:119500, 2023. doi: https://doi.org/10.1016/j.renene.2023.119500.

[12] Y. Wu, X. Lu, J. Cho, L. Rasha, M. Whiteley, T. Neville, R. Ziesche, N. Kardjilov, H. Markötter, I. Manke, and others. Multi-length scale characterization of compression on metal foam flow-field based fuel cells using X-ray computed tomography and neutron radiography. *Energy Conversion and Management*, 230:113785, 2021. doi: https://doi.org/10.1016/j.enconman.2020.113785.

[13] T. Suzuki, Y. Tabuchi, S. Tsushima, and S. Hirai. Measurement of water content distribution in catalyst coated membranes under water permeation conditions by magnetic resonance imaging. *International Journal of Hydrogen Energy*, 36(9): 5479–5486, 2011. doi: https://doi.org/10.1016/j.ijhydene.2011.01.162.

[14] A. Kato, S. Kato, S. Yamaguchi, T. Suzuki, and Y. Nagai. Dependence of vapor and liquid water removal on cross-flow in polymer electrolyte fuel cell investigated by operando synchrotron X-ray radiography. *International Journal of Hydrogen Energy*, 50:1218–1227, 2024. doi: https://doi.org/10.1016/j.ijhydene.2023.06.239.

[15] A. Bozorgnezhad, M. Shams, H. Kanani, M. Hasheminasab, and G. Ahmadi. Two-phase flow and droplet behavior in microchannels of PEM fuel cell. *International Journal of Hydrogen Energy*, 41(42):19164–19181, 2016. doi: https://doi.org/10.1016/j.ijhydene.2016.09.043.

[16] H. Guo, Q. Zhao, and F. Ye. An experimental study on gas and liquid two-phase flow in orientated-type flow channels of proton exchange membrane fuel

cells by using a side-view method. *Renewable Energy*, 188:603–618, 2022. doi: https://doi.org/10.1016/j.renene.2022.02.070.

[17] Y. Liu, Z. Pan, X. Huo, W. Li, X. Shi, R. Chen, and L. An. Two-phase flow visualization in direct ammonia fuel cells. *International Journal of Hydrogen Energy*, 70:159–169, 2024. doi: https://doi.org/10.1016/j.ijhydene.2024.05.158.

[18] F. Barreras, A. Lozano, L. Valino, C. Marin, and A. Pascau. Flow distribution in a bipolar plate of a proton exchange membrane fuel cell: Experiments and numerical simulation studies. *Journal of Power sources*, 144(1):54–66, 2005. doi: https://doi.org/10.1016/j.jpowsour.2004.11.066.

[19] S. Hasanpour, M. Ahadi, M. Bahrami, N. Djilali, and M. Akbari. Woven gas diffusion layers for polymer electrolyte membrane fuel cells: Liquid water transport and conductivity trade-offs. *Journal of Power Sources*, 403:192–198, 2018. doi: https://doi.org/10.1016/j.jpowsour.2018.09.076.

[20] D. Muirhead, R. Banerjee, M. G. George, N. Ge, P. Shrestha, H. Liu, J. Lee, and A. Bazylak. Liquid water saturation and oxygen transport resistance in polymer electrolyte membrane fuel cell gas diffusion layers. *Electrochimica Acta*, 274: 250–265, 2018. doi: https://doi.org/10.1016/j.electacta.2017.03.162.

[21] A. Mularczyk, Q. Lin, M. J. Blunt, A. Lamibrac, F. Marone, T. J. Schmidt, F. N. Büchi, and J. Eller. Droplet and percolation network interactions in a fuel cell gas diffusion layer. *Journal of The Electrochemical Society*, 167(8):084506, 2020. doi: https://doi.org/10.1149/1945-7111/ab8c85.

[22] J. Hinebaugh, J. Lee, C. Mascarenhas, and A. Bazylak. Quantifying percolation events in pem fuel cell using synchrotron radiography. *Electrochimica Acta*, 184:417–426, 2015. doi: https://doi.org/10.1016/j.electacta.2015.09.058.

[23] J. P. Owejan, T. A. Trabold, and M. M. Mench. Oxygen transport resistance correlated to liquid water saturation in the gas diffusion layer of PEM fuel cells. *International Journal of Heat and Mass Transfer*, 71:585–592, 2014. doi: https://doi.org/10.1016/j.ijheatmasstransfer.2013.12.059.

[24] M. Maier, J. Dodwell, R. Ziesche, C. Tan, T. Heenan, J. Majasan, N. Kardjilov, H. Markötter, I. Manke, L. Castanheira, and others. Mass transport in polymer electrolyte membrane water electrolyser liquid-gas diffusion layers: A combined neutron imaging and X-ray computed tomography study. *Journal of Power Sources*, 455:227968, 2020. doi: https://doi.org/10.1016/j.jpowsour.2020.227968.

[25] J. Park, X. Li, D. Tran, T. Abdel-Baset, D. S. Hussey, D. L. Jacobson, and M. Arif. Neutron imaging investigation of liquid water distribution in and the performance of a PEM fuel cell. *International Journal of Hydrogen Energy*, 33(13): 3373–3384, 2008. doi: https://doi.org/10.1016/j.ijhydene.2008.03.019.

[26] R. Banerjee and S. G. Kandlikar. Liquid water quantification in the cathode side gas channels of a proton exchange membrane fuel cell through two-phase flow visualization. *Journal of Power Sources*, 247:9–19, 2014. doi: https://doi.org/10.1016/j.jpowsour.2013.08.016.

[27] R. F. Ziesche, J. Hack, L. Rasha, M. Maier, C. Tan, T. M. Heenan, H. Markötter, N. Kardjilov, I. Manke, W. Kockelmann, and others. High-speed 4D neutron computed tomography for quantifying water dynamics in polymer electrolyte fuel cells. *Nat. Commun.*, 13(1):1616, 2022. doi: https://doi.org/10.1038/s41467-022-29313-5.

[28] B. Wang, W. Pan, Z. Hu, G. Zhang, L. Tang, X. Chen, and F. Wang. A novel spider-web-like design of transition zone to improve two-phase flow uniformity for large-scale proton exchange membrane fuel cells. *Journal of Power Sources*, 623:235441, 2024. doi: https://doi.org/10.1016/j.jpowsour.2024.235441.

[29] G. Zhang, X. Xie, B. Xie, Q. Du, and K. Jiao. Large-scale multi-phase simulation of proton exchange membrane fuel cell. *International Journal of Heat and Mass Transfer*, 130:555–563, 2019. doi: https://doi.org/10.1016/j.ijheatmasstransfer.2018.10.122.

[30] K. N. Kim, J. H. Kang, S. G. Lee, J. H. Nam, and C.-J. Kim. Lattice Boltzmann simulation of liquid water transport in microporous and gas diffusion layers of polymer electrolyte membrane fuel cells. *Journal of Power Sources*, 278:703–717, 2015. doi: https://doi.org/10.1016/j.jpowsour.2014.12.044.

[31] Y. Xu, D. Ye, W. Zhang, Y. Wang, J. Li, L. Zhang, J. Huang, X. Zhu, and Q. Liao. Dual-scale pore network modeling of two-phase transport in anode porous transport layer and catalyst layer of proton exchange membrane electrolyzers. *Energy Conversion and Management*, 322:119089, 2024. doi: https://doi.org/10.1016/j.enconman.2024.119089.

[32] D. Niblett, A. Mularczyk, V. Niasar, J. Eller, and S. Holmes. Two-phase flow dynamics in a gas diffusion layer-gas channel-microporous layer system. *Journal of Power Sources*, 471:228427, 2020. doi: https://doi.org/10.1016/j.jpowsour.2020.228427.

[33] P. A. García-Salaberri and A. Sánchez-Ramos. Modeling of a polymer electrolyte membrane fuel cell with a hybrid continuum/discrete formulation at

the rib/channel scale: Effect of relative humidity and temperature on performance and two-phase transport. *Applied Energy*, 367:123332, 2024. doi: https://doi.org/10.1016/j.apenergy.2024.123332.

[34] C. Su, Z. Chen, H. Zhan, Z. Wang, D. Zhang, Z. Wu, K. Li, L. Yang, X. Du, J. Hao, and others. Optimal design and performance analysis of anode flow channels in proton exchange membrane water electrolyzers. *Applied Thermal Engineering*, 248:123201, 2024. doi: https://doi.org/10.1016/j.applthermaleng.2024.123201.

[35] J. Choi, Y. Park, J. Park, C. Kim, S. Heo, S.-D. Kim, and H. Ju. Innovative flow field design strategies for performance optimization in polymer electrolyte membrane fuel cells. *Applied Energy*, 377:124551, 2025. doi: https://doi.org/10.1016/j.apenergy.2024.124551.

[36] Q. Wang, W. Zheng, B. Li, J. P. Zheng, G. Cui, L. Hao, and P. Ming. Simulation-based study of local hydrogen crossover dynamics and their effects on proton exchange membrane fuel cells. *Chemical Engineering Journal*, 499:156408, 2024. doi: https://doi.org/10.1016/j.cej.2024.156408.

[37] E. Tardy, J.-P. Poirot-Crouvezier, P. Schott, C. Morel, G. Serre, and Y. Bultel. Investigation of liquid water heterogeneities in large area proton exchange membrane fuel cells using a Darcy two-phase flow model in a multiphysics code. *International Journal of Hydrogen Energy*, 47(91):38721–38735, 2022. doi: https://doi.org/10.1016/j.ijhydene.2022.09.039.

[38] U. Pasaogullari, C.-Y. Wang, and K. S. Chen. Two-phase transport in polymer electrolyte fuel cells with bilayer cathode gas diffusion media. *Journal of the Electrochemical Society*, 152(8):A1574, 2005. doi: https://doi.org/10.1149/1.1938067.

[39] G. He, Y. Yamazaki, and A. Abudula. A droplet size dependent multiphase mixture model for two phase flow in PEMFCs. *Journal of Power Sources*, 194 (1):190–198, 2009. doi: https://doi.org/10.1016/j.jpowsour.2009.05.008.

[40] S. Zhang, S. Hess, H. Marschall, U. Reimer, S. Beale, and W. Lehnert. openFuelCell2: A new computational tool for fuel cells, electrolyzers, and other electrochemical devices and processes. *Computer Physics Communications*, 298: 109092, 2024. doi: https://doi.org/10.1016/j.cpc.2024.109092.

[41] G. Zhang and K. Jiao. Three-dimensional multi-phase simulation of PEMFC at high current density utilizing Eulerian-Eulerian model and two-fluid model. *Energy Conversion and Management*, 176:409–421, 2018. doi: https://doi.org/10.1016/j.enconman.2018.09.031.

[42] J. Bear. *Dynamics of fluids in porous media*. Courier Corporation, 2013.

[43] M. Ishii and T. Hibiki. *Thermo-fluid dynamics of two-phase flow*. Springer Science & Business Media, 2010.

[44] D. A. Drew and S. L. Passman. *Theory of multicomponent fluids*, volume 135. Springer Science & Business Media, 2006.

[45] C. W. Hirt and B. D. Nichols. Volume of fluid (VOF) method for the dynamics of free boundaries. *Journal of Computational Physics*, 39(1):201–225, 1981. doi: https://doi.org/10.1016/0021-9991(81)90145-5.

[46] Y. Liu, C. Tang, M. Kohrn, B. Shi, Z. Wang, M. Wick, S. Pischinger, and J. Andert. A numerical study of the polarization effect of liquid water in the gas diffusion layer of a proton exchange membrane fuel cell. *Journal of Power Sources*, 529:231221, 2022. doi: https://doi.org/10.1016/j.jpowsour.2022.231221.

[47] S. Chen, H. Chen, D. Martnez, and W. Matthaeus. Lattice Boltzmann model for simulation of magnetohydrodynamics. *Physical Review Letters*, 67(27):3776, 1991. doi: https://doi.org/10.1103/PhysRevLett.67.3776.

[48] M. Sussman, P. Smereka, and S. Osher. A level set approach for computing solutions to incompressible two-phase flow. *Journal of Computational physics*, 114(1):146–159, 1994. doi: https://doi.org/10.1006/jcph.1994.1155.

[49] P.-H. Chiu and Y.-T. Lin. A conservative phase field method for solving incompressible two-phase flows. *Journal of Computational Physics*, 230(1):185–204, 2011. doi: https://doi.org/10.1016/j.jcp.2010.09.021.

[50] S. T. Zalesak. Fully multidimensional flux-corrected transport algorithms for fluids. *Journal of computational physics*, 31(3):335–362, 1979. doi: https://doi.org/10.1016/0021-9991(79)90051-2.

[51] E. G. Puckett, A. S. Almgren, J. B. Bell, D. L. Marcus, and W. J. Rider. A high-order projection method for tracking fluid interfaces in variable density incompressible flows. *Journal of computational physics*, 130(2):269–282, 1997. doi: https://doi.org/10.1006/jcph.1996.5590.

[52] M. Dianat, M. Skarysz, and A. Garmory. A coupled level set and volume of fluid method for automotive exterior water management applications. *International Journal of Multiphase Flow*, 91:19–38, 2017. doi: https://doi.org/10.1016/j.ijmultiphaseflow.2017.01.008.

[53] S. Mirjalili, S. S. Jain, and M. Dodd. Interface-capturing methods for two-phase flows: An overview and recent developments. *Center for Turbulence Research Annual Research Briefs*, 2017(117-135):13, 2017.

[54] M. Xiao, G. Yang, Y. Huang, and J. Wu. Evaluation of different interface-capturing methods for cryogenic two-phase flows under microgravity. *Physics of Fluids*, 34(11), 2022. doi: https://doi.org/10.1063/5.0127146.

[55] T. Marić, D. B. Kothe, and D. Bothe. Unstructured un-split geometrical volume-of-fluid methods–a review. *Journal of Computational Physics*, 420:109695, 2020. doi: https://doi.org/10.1016/j.jcp.2020.109695.

[56] J. López and J. Hernández. gVOF: An open-source package for unsplit geometric volume of fluid methods on arbitrary grids. *Computer Physics Communications*, 277:108400, 2022. doi: https://doi.org/10.1016/j.cpc.2022.108400.

[57] J. Roenby, H. Bredmose, and H. Jasak. A computational method for sharp interface advection. *Royal Society open science*, 3(11):160405, 2016. doi: https://doi.org/10.1098/rsos.160405.

[58] H. Scheufler and J. Roenby. Accurate and efficient surface reconstruction from volume fraction data on general meshes. *Journal of computational physics*, 383: 1–23, 2019. doi: https://doi.org/10.1016/j.jcp.2019.01.009.

[59] A. Esteban, J. Lopez, P. Gomez, C. Zanzi, J. Roenby, and J. Hernandez. A comparative study of two open-source state-of-the-art geometric VOF methods. *Computers & Fluids*, 250:105725, 2023. doi: https://doi.org/10.1016/j.compfluid.2022.105725.

[60] A. Bazylak, D. Sinton, and N. Djilali. Dynamic water transport and droplet emergence in PEMFC gas diffusion layers. *Journal of Power Sources*, 176(1): 240–246, 2008. doi: https://doi.org/10.1016/j.jpowsour.2007.10.066.

[61] L. Chen, T.-F. Cao, Z.-H. Li, Y.-L. He, and W.-Q. Tao. Numerical investigation of liquid water distribution in the cathode side of proton exchange membrane fuel cell and its effects on cell performance. *International Journal of Hydrogen Energy*, 37(11):9155–9170, 2012. doi: https://doi.org/10.1016/j.ijhydene.2012.01.101.

[62] T. Hellstern, E. Gauthier, M. J. Cheah, and J. B. Benziger. The role of the gas diffusion layer on slug formation in gas flow channels of fuel cells. *International Journal of Hydrogen Energy*, 38(35):15414–15427, 2013. doi: https://doi.org/10.1016/j.ijhydene.2013.09.073.

[63] R. B. Ferreira, D. Falcão, V. Oliveira, and A. Pinto. Numerical simulations of two-phase flow in proton exchange membrane fuel cells using the volume of fluid method–A review. *Journal of Power Sources*, 277:329–342, 2015. doi: https://doi.org/10.1016/j.jpowsour.2014.11.124.

[64] M. Andersson, S. Beale, U. Reimer, W. Lehnert, and D. Stolten. Interface resolving two-phase flow simulations in gas channels relevant for polymer electrolyte fuel cells using the volume of fluid approach. *International Journal of Hydrogen Energy*, 43(5):2961–2976, 2018. doi: https://doi.org/10.1016/j.ijhydene.2017.12.129.

[65] Y. Ding, H. Bi, and D. Wilkinson. Three-dimensional numerical simulation of water droplet emerging from a gas diffusion layer surface in micro-channels. *Journal of Power Sources*, 195(21):7278–7288, 2010. doi: https://doi.org/10.1016/j.jpowsour.2010.05.059.

[66] Y. Ding, R. Anderson, L. Zhang, X. Bi, and D. P. Wilkinson. Simulations of two-phase flow distribution in communicating parallel channels for a PEM fuel cell. *International Journal of Multiphase Flow*, 52:35–45, 2013. doi: https://doi.org/10.1016/j.ijmultiphaseflow.2012.12.001.

[67] R. B. Ferreira, D. S. Falcão, V. B. Oliveira, and A. M. Pinto. 1D+ 3D two-phase flow numerical model of a proton exchange membrane fuel cell. *Applied energy*, 203:474–495, 2017. doi: https://doi.org/10.1016/j.apenergy.2017.06.048.

[68] L. Liu, L. Guo, R. Zhang, L. Chen, and W.-Q. Tao. Numerically investigating two-phase reactive transport in multiple gas channels of proton exchange membrane fuel cells. *Applied energy*, 302:117625, 2021. doi: https://doi.org/10.1016/j.apenergy.2021.117625.

[69] D. Lorenzini-Gutierrez, S. G. Kandlikar, A. Hernandez-Guerrero, and F. Elizalde-Blancas. Residence time of water film and slug flow features in fuel cell gas channels and their effect on instantaneous area coverage ratio. *Journal of Power Sources*, 279:567–580, 2015. doi: https://doi.org/10.1016/j.jpowsour.2015.01.041.

[70] Y. Ding, H. Bi, and D. Wilkinson. Three dimensional numerical simulation of gas–liquid two-phase flow patterns in a polymer–electrolyte membrane fuel cells gas flow channel. *Journal of Power Sources*, 196(15):6284–6292, 2011. doi: https://doi.org/10.1016/j.jpowsour.2011.03.100.

[71] E. Mancusi, É. Fontana, de A. A. U. Souza, and de S. M. G. U. Souza. Numerical study of two-phase flow patterns in the gas channel of PEM fuel cells

with tapered flow field design. *International Journal of Hydrogen Energy*, 39 (5):2261–2273, 2014. doi: https://doi.org/10.1016/j.ijhydene.2013.11.106.

[72] L. Zhang, S. Liu, Z. Wang, R. Li, and Q. Zhang. Numerical simulation of two-phase flow in a multi-gas channel of a proton exchange membrane fuel cell. *International Journal of Hydrogen Energy*, 47(40):17713–17736, 2022. doi: https://doi.org/10.1016/j.ijhydene.2022.03.246.

[73] Z. Niu, K. Jiao, Y. Wang, Q. Du, and Y. Yin. Numerical simulation of two-phase cross flow in the gas diffusion layer microstructure of proton exchange membrane fuel cells. *International Journal of Energy Research*, 42(2):802–816, 2018. doi: https://doi.org/10.1002/er.3867.

[74] Z. Bao, Y. Li, X. Zhou, F. Gao, Q. Du, and K. Jiao. Transport properties of gas diffusion layer of proton exchange membrane fuel cells: Effects of compression. *International Journal of Heat and Mass Transfer*, 178:121608, 2021. doi: https://doi.org/10.1016/j.ijheatmasstransfer.2021.121608.

[75] G. Chen, Q. Xu, J. Xuan, J. Liu, Q. Fu, W. Shi, H. Su, and L. Xing. Numerical study of inhomogeneous deformation of gas diffusion layers on proton exchange membrane fuel cells performance. *Journal of Energy Storage*, 44:103486, 2021. doi: https://doi.org/10.1016/j.est.2021.103486.

[76] P. Sarkezi-Selsky, H. Schmies, A. Kube, A. Latz, and T. Jahnke. Lattice Boltzmann simulation of liquid water transport in gas diffusion layers of proton exchange membrane fuel cells: Parametric studies on capillary hysteresis. *Journal of Power Sources*, 535:231381, 2022. doi: https://doi.org/10.1016/j.jpowsour.2022.231381.

[77] D. H. Jeon. Effect of gas diffusion layer thickness on liquid water transport characteristics in polymer electrolyte membrane fuel cells. *Journal of Power Sources*, 475:228578, 2020. doi: https://doi.org/10.1016/j.jpowsour.2020.228578.

[78] S. Zhang, S. Xu, and F. Dong. Study on ice-melting performance of gradient gas diffusion layer in proton exchange membrane fuel cell. *International Journal of Hydrogen Energy*, 47(54):22981–22992, 2022. doi: https://doi.org/10.1016/j.ijhydene.2022.05.093.

[79] D. Jiao, K. Jiao, and Q. Du. Vapor condensation in reconstructed gas diffusion layers of proton exchange membrane fuel cell. *International Journal of Energy Research*, 45(3):4466–4478, 2021. doi: https://doi.org/10.1002/er.6116.

[80] X. Shi, D. Jiao, Z. Bao, K. Jiao, W. Chen, and Z. Liu. Liquid transport in gas diffusion layer of proton exchange membrane fuel cells: Effects of microporous layer cracks. *International Journal of Hydrogen Energy*, 47(9):6247–6258, 2022. doi: https://doi.org/10.1016/j.ijhydene.2021.11.248.

[81] Y. Yu, S. Chen, and H. Wei. Numerical study on the effect of microporous layer crack changes on water management in gas diffusion layer of proton exchange membrane fuel cell. *International Journal of Heat and Mass Transfer*, 212: 124275, 2023. doi: https://doi.org/10.1016/j.ijheatmasstransfer.2023.124275.

[82] Y. Ira, Y. Bakhshan, and J. Khorshidimalahmadi. Effect of wettability heterogeneity and compression on liquid water transport in gas diffusion layer coated with microporous layer of PEMFC. *International Journal of Hydrogen Energy*, 46 (33):17397–17413, 2021. doi: https://doi.org/10.1016/j.ijhydene.2021.02.160.

[83] L. Guo, L. Chen, R. Zhang, M. Peng, and W.-Q. Tao. Pore-scale simulation of two-phase flow and oxygen reactive transport in gas diffusion layer of proton exchange membrane fuel cells: Effects of nonuniform wettability and porosity. *Energy*, 253:124101, 2022. doi: https://doi.org/10.1016/j.energy.2022.124101.

[84] S. B. Beale, M. Andersson, N. Weber, H. Marschall, and W. Lehnert. Combined two-phase co-flow and counter-flow in a gas channel/porous transport layer assembly. *ECS Transactions*, 98(9):305, 2020. doi: https://doi.org/10.1149/09809.0305ecst.

[85] D. Yang, H. Garg, and M. Andersson. Numerical simulation of two-phase flow in gas diffusion layer and gas channel of proton exchange membrane fuel cells. *International Journal of Hydrogen Energy*, 48(41):15677–15694, 2023. doi: https://doi.org/10.1016/j.ijhydene.2023.01.013.

[86] D. Niblett, V. Niasar, S. Holmes, A. Mularczyk, J. Eller, R. Prosser, and M. Mamlouk. Water cluster characteristics of fuel cell gas diffusion layers with artificial microporous layer crack dilation. *Journal of Power Sources*, 555:232383, 2023. doi: https://doi.org/10.1016/j.jpowsour.2022.232383.

[87] R. Lin, M. Dong, S. Lan, and M. Lou. Numerical simulation of liquid water transport in perforated cracks of microporous layer. *Energy*, 262:125372, 2023. doi: https://doi.org/10.1016/j.energy.2022.125372.

[88] Y. Sun, C. Bao, Z. Jiang, X. Zhang, and T. Gao. A two-dimensional numerical study of liquid water breakthrough in gas diffusion layer based on phase field method. *Journal of Power Sources*, 448:227352, 2020. doi: https://doi.org/10.1016/j.jpowsour.2019.227352.

[89] X. Zhou, L. Wu, Z. Niu, Z. Bao, X. Sun, Z. Liu, Y. Li, K. Jiao, Z. Liu, and Q. Du. Effects of surface wettability on two-phase flow in the compressed gas diffusion layer microstructures. *International Journal of Heat and Mass Transfer*, 151: 119370, 2020. doi: https://doi.org/10.1016/j.ijheatmasstransfer.2020.119370.

[90] Z. Niu, J. Wu, Z. Bao, Y. Wang, Y. Yin, and K. Jiao. Two-phase flow and oxygen transport in the perforated gas diffusion layer of proton exchange membrane fuel cell. *International Journal of Heat and Mass Transfer*, 139:58–68, 2019. doi: https://doi.org/10.1016/j.ijheatmasstransfer.2019.05.008.

[91] X. Zhou, Z. Niu, Y. Li, X. Sun, Q. Du, J. Xuan, and K. Jiao. Investigation of two-phase flow in the compressed gas diffusion layer microstructures. *International Journal of Hydrogen Energy*, 44(48):26498–26516, 2019. doi: https://doi.org/10.1016/j.ijhydene.2019.08.108.

[92] Z. Niu, Z. Bao, J. Wu, Y. Wang, and K. Jiao. Two-phase flow in the mixed-wettability gas diffusion layer of proton exchange membrane fuel cells. *Applied energy*, 232:443–450, 2018. doi: https://doi.org/10.1016/j.apenergy.2018.09.209.

[93] Z. Lu, M. M. Daino, C. Rath, and S. G. Kandlikar. Water management studies in PEM fuel cells, part III: Dynamic breakthrough and intermittent drainage characteristics from GDLs with and without MPLs. *International Journal of Hydrogen Energy*, 35(9):4222–4233, 2010. doi: https://doi.org/10.1016/j.ijhydene.2010.01.012.

[94] Y.-C. Chen, C. Karageorgiou, J. Eller, T. J. Schmidt, and F. N. Büchi. Determination of the porosity and its heterogeneity of fuel cell microporous layers by X-ray tomographic microscopy. *Journal of Power Sources*, 539:231612, 2022. doi: https://doi.org/10.1016/j.jpowsour.2022.231612.

[95] A. Z. Weber, R. L. Borup, R. M. Darling, P. K. Das, T. J. Dursch, W. Gu, D. Harvey, A. Kusoglu, S. Litster, M. M. Mench, and others. A critical review of modeling transport phenomena in polymer-electrolyte fuel cells. *Journal of The Electrochemical Society*, 161(12):F1254, 2014. doi: https://doi.org/10.1149/2.0751412jes.

[96] A. D. Santamaria, P. K. Das, J. C. MacDonald, and A. Z. Weber. Liquid-water interactions with gas-diffusion-layer surfaces. *Journal of The Electrochemical Society*, 161(12):F1184, 2014. doi: https://doi.org/10.1149/2.0321412jes.

[97] X. Zhou, Z. Niu, Z. Bao, J. Wang, Z. Liu, Y. Yin, Q. Du, and K. Jiao. Two-phase flow in compressed gas diffusion layer: Finite element and volume of

fluid modeling. *Journal of Power Sources*, 437:226933, 2019. doi: https://doi.org/10.1016/j.jpowsour.2019.226933.

[98] Z. Li, Z. Ke, Y. Huang, W. Wu, Y. Zhang, and P. Li. Investigation of flow characteristics on porous gas diffusion layer microstructure that generated with binder and polytetrafluoroethylene distribution. *Physics of Fluids*, 35(1), 2023. doi: https://doi.org/10.1063/5.0131680.

[99] Y. Ding, X. Bi, and D. P. Wilkinson. 3D simulations of the impact of two-phase flow on PEM fuel cell performance. *Chemical Engineering Science*, 100:445–455, 2013. doi: https://doi.org/10.1016/j.ces.2012.11.007.

[100] P. Feng, L. Tan, Y. Cao, and D. Chen. Numerical investigations of two-phase flow coupled with species transport in proton exchange membrane fuel cells. *Energy*, 278:127918, 2023. doi: https://doi.org/10.1016/j.energy.2023.127918.

[101] Y. Cao, M. El-Shorbagy, M. Dahari, D. N. Cao, E. M. T. El Din, P. H. Huynh, and M. Wae-hayee. Examining the relationship between gas channel dimensions of a polymer electrolyte membrane fuel cell with two-phase flow dynamics in a flooding situation using the volume of fluid method. *Energy Reports*, 8:9420–9430, 2022. doi: https://doi.org/10.1016/j.egyr.2022.07.048.

[102] J. Hu, W. Liu, H. Li, Q. Zhu, D. Dong, and Y. Yuan. Enhanced water management via vibration for proton exchange membrane fuel cells cathode. *Energy Conversion and Management*, 327:119591, 2025. doi: https://doi.org/10.1016/j.enconman.2025.119591.

[103] S. Nazari, E. R. Silva, U. Trdan, D. Culliton, and others. Computational fluid dynamics analysis of superhydrophobic and superhydrophilic micro-textures for biofouling mitigation. *Results in Engineering*, page 104627, 2025. doi: https://doi.org/10.1016/j.rineng.2025.104627.

[104] S. Li, L. Huang, D. Wang, S. Zhou, X. Sun, R. Zhao, G. Wang, T. Yao, K. Zhao, and R. Chen. A review of 3D superhydrophilic porous materials for oil/water separation. *Separation and Purification Technology*, 326:124847, 2023. doi: https://doi.org/10.1016/j.seppur.2023.124847.

[105] M. Andersson, A. Mularczyk, A. Lamibrac, S. Beale, J. Eller, W. Lehnert, and F. Büchi. Modeling and synchrotron imaging of droplet detachment in gas channels of polymer electrolyte fuel cells. *Journal of Power Sources*, 404:159–171, 2018. doi: https://doi.org/10.1016/j.jpowsour.2018.10.021.

[106] Q. Chen, Z. Niu, H. Li, K. Jiao, and Y. Wang. Recent progress of gas diffusion layer in proton exchange membrane fuel cell: Two-phase flow and material

properties. *International Journal of Hydrogen Energy*, 46(12):8640–8671, 2021. doi: https://doi.org/10.1016/j.ijhydene.2020.12.076.

[107] H.-Y. Tang, A. Santamaria, J. W. Park, C. Lee, and W. Hwang. Quantification of water in hydrophobic and hydrophilic flow channels subjected to gas purging via neutron imaging. *Journal of Power Sources*, 196(22):9373–9381, 2011. doi: https://doi.org/10.1016/j.jpowsour.2011.05.057.

[108] T. Zhao, K. Jiang, W. Fan, D. Lu, D. Zheng, H. Cui, L. Yang, G. Lu, and Z. Liu. Nature-inspired hybrid wettability surface to enhance water management on bipolar plates of PEMFC. *Chemical Engineering Journal*, 466:143288, 2023. doi: https://doi.org/10.1016/j.cej.2023.143288.

[109] Y. Hou, G. Zhang, Y. Qin, Q. Du, and K. Jiao. Numerical simulation of gas liquid two-phase flow in anode channel of low-temperature fuel cells. *International Journal of Hydrogen Energy*, 42(5):3250–3258, 2017. doi: https://doi.org/10.1016/j.ijhydene.2016.09.219.

[110] P. Liao, D. Yang, S. Xu, B. Li, P. Ming, Z. Li, and X. Zhou. Effect of three-dimensional geometric structure and surface wettability on two-phase flow behavior in a proton exchange membrane fuel cell gas flow channel: modeling and simulation. *International Journal of Hydrogen Energy*, 50:1183–1199, 2024. doi: https://doi.org/10.1016/j.ijhydene.2023.06.228.

[111] Z. Bao, Z. Niu, and K. Jiao. Numerical simulation for metal foam two-phase flow field of proton exchange membrane fuel cell. *International Journal of Hydrogen Energy*, 44(12):6229–6244, 2019. doi: https://doi.org/10.1016/j.ijhydene.2019.01.086.

[112] Z. Lu, C. Rath, G. Zhang, and S. G. Kandlikar. Water management studies in PEM fuel cells, part IV: Effects of channel surface wettability, geometry and orientation on the two-phase flow in parallel gas channels. *International Journal of Hydrogen Energy*, 36(16):9864–9875, 2011. doi: https://doi.org/10.1016/j.ijhydene.2011.04.226.

[113] P. Gopalan and S. G. Kandlikar. Effect of channel materials and trapezoidal corner angles on emerging droplet behavior in proton exchange membrane fuel cell gas channels. *Journal of Power Sources*, 248:230–238, 2014. doi: https://doi.org/10.1016/j.jpowsour.2013.09.070.

[114] E. Shakerinejad, M. Kayhani, M. Nazari, and A. Tamayol. Increasing the performance of gas diffusion layer by insertion of small hydrophilic layer in proton-exchange membrane fuel cells. *International Journal of Hydrogen Energy*, 43 (4):2410–2428, 2018. doi: https://doi.org/10.1016/j.ijhydene.2017.12.038.

[115] Y. Yin, T. Wu, P. He, Q. Du, and K. Jiao. Numerical simulation of two-phase cross flow in microstructure of gas diffusion layer with variable contact angle. *International Journal of Hydrogen Energy*, 39(28):15772–15785, 2014. doi: https://doi.org/10.1016/j.ijhydene.2014.07.162.

[116] S. P. Kuttanikkad, M. Prat, and J. Pauchet. Pore-network simulations of two-phase flow in a thin porous layer of mixed wettability: Application to water transport in gas diffusion layers of proton exchange membrane fuel cells. *Journal of Power Sources*, 196(3):1145–1155, 2011. doi: https://doi.org/10.1016/j.jpowsour.2010.09.029.

[117] B. Lim, E. Majlan, W. Daud, M. Rosli, and T. Husaini. Numerical analysis of modified parallel flow field designs for fuel cells. *International Journal of Hydrogen Energy*, 42(14):9210–9218, 2017. doi: https://doi.org/10.1016/j.ijhydene.2016.03.189.

[118] H. Huang, M. Liu, X. Li, X. Guo, T. Wang, S. Li, and H. Lei. Numerical simulation and visualization study of a new tapered-slope serpentine flow field in proton exchange membrane fuel cell. *Energy*, 246:123406, 2022. doi: https://doi.org/10.1016/j.energy.2022.123406.

[119] V. Thitakamol, A. Therdthianwong, and S. Therdthianwong. Mid-baffle interdigitated flow fields for proton exchange membrane fuel cells. *International Journal of Hydrogen Energy*, 36(5):3614–3622, 2011. doi: https://doi.org/10.1016/j.ijhydene.2010.12.060.

[120] H. Heidary, M. Kermani, A. K. Prasad, and S. G. Advani. Experimental and numerical studies of enhanced interdigitated flow field for pem fuel cells. *Journal of Energy Engineering*, 147(4):04021026, 2021. doi: https://doi.org/10.1061/(ASCE)EY.1943-7897.0000767.

[121] X. Liu, H. Guo, F. Ye, and C. F. Ma. Flow dynamic characteristics in flow field of proton exchange membrane fuel cells. *International Journal of Hydrogen Energy*, 33(3):1040–1051, 2008. doi: https://doi.org/10.1016/j.ijhydene.2007.11.018.

[122] N. Konno, S. Mizuno, H. Nakaji, and Y. Ishikawa. Development of compact and high-performance fuel cell stack. *SAE International Journal of Alternative Powertrains*, 4(1):123–129, 2015. URL https://www.jstor.org/stable/26169071.

[123] G. Zhang, Z. Qu, W.-Q. Tao, X. Wang, L. Wu, S. Wu, X. Xie, C. Tongsh, W. Huo, Z. Bao, and others. Porous flow field for next-generation proton exchange membrane fuel cells: materials, characterization, design, and challenges. *Chemical Reviews*, 123(3):989–1039, 2022. doi: https://doi.org/10.1021/acs.chemrev.2c00539.

[124] L. Xia, Z. Yu, G. Xu, S. Ji, and B. Sun. Design and optimization of a novel composite bionic flow field structure using three-dimensional multiphase computational fluid dynamic method for proton exchange membrane fuel cell. *Energy Conversion and Management*, 247:114707, 2021. doi: https://doi.org/10.1016/j.enconman.2021.114707.

[125] L. Chen, Y.-L. He, and W.-Q. Tao. Effects of surface microstructures of gas diffusion layer on water droplet dynamic behaviors in a micro gas channel of proton exchange membrane fuel cells. *International Journal of Heat and Mass Transfer*, 60:252–262, 2013. doi: https://doi.org/10.1016/j.ijheatmasstransfer.2012.11.024.

[126] X. Lv, Z. Zhou, W.-T. Wu, L. Wei, L. Gao, Y. Yang, Y. Li, Y. Li, and Y. Song. Two-phase flow dynamics study in the trapezoidal gas channel of PEM fuel cell based on lattice Boltzmann model. *International Journal of Green Energy*, 21 (10):2264–2280, 2024. doi: https://doi.org/10.1080/15435075.2023.2300376.

[127] G. He, Y. Yamazaki, and A. Abudula. The effect of wall roughness on the liquid removal in micro-channels related to a proton exchange membrane fuel cell (PEMFC). *Journal of Power Sources*, 195(6):1561–1568, 2010. doi: https://doi.org/10.1016/j.jpowsour.2009.09.052.

[128] Y. Bao and Y. Gan. Roughness effects of gas diffusion layers on droplet dynamics in PEMFC flow channels. *International Journal of Hydrogen Energy*, 45 (35):17869–17881, 2020. doi: https://doi.org/10.1016/j.ijhydene.2020.04.228.

[129] J. Yang, L. Fei, X. Zhang, X. Ma, K. H. Luo, and S. Shuai. Dynamic behavior of droplet transport on realistic gas diffusion layer with inertial effect via a unified lattice Boltzmann method. *International Journal of Hydrogen Energy*, 46(66): 33260–33271, 2021. doi: https://doi.org/10.1016/j.ijhydene.2021.07.124.

[130] S. G. Kandlikar, S. Joshi, and S. Tian. Effect of surface roughness on heat transfer and fluid flow characteristics at low Reynolds numbers in small diameter tubes. *Heat Transfer Engineering*, 24(3):4–16, 2003. doi: https://doi.org/10.1080/01457630304069.

[131] V. Parry, G. Berthomé, and J.-C. Joud. Wetting properties of gas diffusion layers: Application of the Cassie–Baxter and Wenzel equations. *Applied surface science*, 258(15):5619–5627, 2012. doi: https://doi.org/10.1016/j.apsusc.2012.02.038.

[132] J. Park and X. Li. Multi-phase micro-scale flow simulation in the electrodes of a pem fuel cell by lattice Boltzmann method. *Journal of Power Sources*, 178(1): 248–257, 2008. doi: https://doi.org/10.1016/j.jpowsour.2007.12.008.

[133] G. E.-E. Aquah, D. Niblett, J. Shokri, and V. Niasar. Characterisation of hydraulic properties of commercial gas diffusion layers: Toray, SGL, MGL, woven carbon cloth. *Scientific Reports*, 14(1):18812, 2024. doi: https://doi.org/10.1038/s41598-024-68681-4.

[134] J. Hinebaugh, J. Gostick, and A. Bazylak. Stochastic modeling of polymer electrolyte membrane fuel cell gas diffusion layers – Part 2: A comprehensive substrate model with pore size distribution and heterogeneity effects. *International Journal of Hydrogen Energy*, 42(24):15872–15886, 2017. ISSN 0360-3199. doi: https://doi.org/10.1016/j.ijhydene.2017.04.269.

[135] H. Wang, G. Yang, S. Li, Q. Shen, J. Liao, Z. Jiang, G. Zhang, H. Zhang, and F. Su. Effect of binder and compression on the transport parameters of a multilayer gas diffusion layer. *Energy & Fuels*, 35(18):15058–15073, 2021. doi: https://doi.org/10.1021/acs.energyfuels.1c01598.

[136] S. Li, P. Chen, Q. Shen, S. Zhang, J. Liao, Z. Jiang, P. Gao, and M. Andersson. Pore-scale study of two-phase flow in the gas diffusion layer of proton exchange membrane fuel cells: The impact of polytetrafluoroethylene content and gradient distribution. *Materials Today Communications*, 39:108773, 2024. doi: https://doi.org/10.1016/j.mtcomm.2024.108773.

[137] J. Mo, C. Zhang, W. Zheng, Y. Hu, Z. Li, and T. Suekane. Influence of binder content on gas-water two-phase flow and displacement phase diagram in the gas diffusion layer of PEMFC: A pore network view. *International Journal of Heat and Mass Transfer*, 231:125838, 2024. doi: https://doi.org/10.1016/j.ijheatmasstransfer.2024.125838.

[138] T. G. Tranter, P. Boillat, A. Mularczyk, V. Manzi-Orezzoli, P. Shearing, D. Brett, J. Eller, J. Gostick, and A. Forner-Cuenca. Pore network modelling of capillary transport and relative diffusivity in gas diffusion layers with patterned wettability. *Journal of The Electrochemical Society*, 167(11):114512, 2020. doi: https://doi.org/10.1149/1945-7111/ab9d61.

[139] M. Bosomoiu, G. Tsotridis, and T. Bednarek. Study of effective transport properties of fresh and aged gas diffusion layers. *Journal of Power Sources*, 285: 568–579, 2015. doi: https://doi.org/10.1016/j.jpowsour.2015.03.132.

[140] R. Flückiger, F. Marone, M. Stampanoni, A. Wokaun, and F. N. Büchi. Investigation of liquid water in gas diffusion layers of polymer electrolyte fuel cells using X-ray tomographic microscopy. *Electrochimica Acta*, 56(5):2254–2262, 2011. doi: https://doi.org/10.1016/j.electacta.2010.12.016.

[141] P. Satjaritanun, J. Weidner, S. Hirano, Z. Lu, Y. Khunatorn, S. Ogawa, S. Litster, A. Shum, I. Zenyuk, and S. Shimpalee. Micro-scale analysis of liquid water breakthrough inside gas diffusion layer for PEMFC using X-ray computed tomography and lattice Boltzmann method. *Journal of The Electrochemical Society*, 164(11):E3359, 2017. doi: https://doi.org/10.1149/2.0391711jes.

[142] C. Tötzke, G. Gaiselmann, M. Osenberg, J. Bohner, T. Arlt, H. Markoetter, A. Hilger, F. Wieder, A. Kupsch, B. R. Müller, and others. Three-dimensional study of compressed gas diffusion layers using synchrotron X-ray imaging. *Journal of Power Sources*, 253:123–131, 2014. doi: https://doi.org/10.1016/j.jpowsour.2013.12.062.

[143] I. V. Zenyuk, D. Y. Parkinson, L. G. Connolly, and A. Z. Weber. Gas-diffusion-layer structural properties under compression via X-ray tomography. *Journal of Power Sources*, 328:364–376, 2016. doi: https://doi.org/10.1016/j.jpowsour.2016.08.020.

[144] L. Xiao, M. Luo, H. Zhang, R. Zeis, and P.-C. Sui. Solid mechanics simulation of reconstructed gas diffusion layers for PEMFCs. *Journal of The Electrochemical Society*, 166(6):F377, 2019. doi: https://doi.org/10.1149/2.0421906jes.

[145] Q. Shi, C. Feng, P. Ming, F. Tang, and C. Zhang. Compressive stress and its impact on the gas diffusion layer: A review. *International Journal of Hydrogen Energy*, 47(6):3994–4009, 2022. doi: https://doi.org/10.1016/j.ijhydene.2021.10.058.

[146] Q. Chen, Z. Niu, H. Li, K. Jiao, and Y. Wang. Recent progress of gas diffusion layer in proton exchange membrane fuel cell: Two-phase flow and material properties. *International Journal of Hydrogen Energy*, 46(12):8640–8671, 2021. ISSN 0360-3199. doi: https://doi.org/10.1016/j.ijhydene.2020.12.076.

[147] L. Zhu, W. Yang, L. Xiao, H. Zhang, X. Gao, and P.-C. Sui. Stochastically modeled gas diffusion layers: effects of binder and polytetrafluoroethylene on effective gas diffusivity. *Journal of The Electrochemical Society*, 168(1):014514, 2021. doi: https://doi.org/10.1149/1945-7111/abdc60.

[148] J. Lee, S. Chevalier, R. Banerjee, P. Antonacci, N. Ge, R. Yip, T. Kotaka, Y. Tabuchi, and A. Bazylak. Investigating the effects of gas diffusion layer substrate thickness on polymer electrolyte membrane fuel cell performance via synchrotron X-ray radiography. *Electrochimica Acta*, 236:161–170, 2017. doi: https://doi.org/10.1016/j.electacta.2017.03.162.

[149] D. H. Jeon and H. Kim. Effect of compression on water transport in gas diffusion layer of polymer electrolyte membrane fuel cell using lattice Boltzmann method.

Journal of Power Sources, 294:393–405, 2015. doi: https://doi.org/10.1016/j.jpowsour.2015.06.080.

[150] D. Yang, H. Garg, S. B. Beale, and M. Andersson. Numerical reconstruction of proton exchange membrane fuel cell gas diffusion layers. *ECS Transactions*, 112(4):49, 2023. doi: https://doi.org/10.1149/11204.0049ecst.

[151] W. Chen and F. Jiang. Impact of PTFE content and distribution on liquid–gas flow in pemfc carbon paper gas distribution layer: 3D lattice Boltzmann simulations. *International Journal of Hydrogen Energy*, 41(20):8550–8562, 2016. ISSN 0360-3199. doi: https://doi.org/10.1016/j.ijhydene.2016.02.159.

[152] S. Zhou, G. Xie, H. Hu, and M. Ni. Simulation on water transportation in gas diffusion layer of a PEM fuel cell: Influence of non-uniform PTFE distribution. *International Journal of Hydrogen Energy*, 48(28):10644–10658, 2023. doi: https://doi.org/10.1016/j.ijhydene.2022.12.063.

[153] H. Zhang, L. Zhu, H. B. Harandi, K. Duan, R. Zeis, P.-C. Sui, and P.-Y. A. Chuang. Microstructure reconstruction of the gas diffusion layer and analyses of the anisotropic transport properties. *Energy Conversion and Management*, 241:114293, 2021. doi: https://doi.org/10.1016/j.enconman.2021.114293.

[154] G. Gaiselmann, D. Froning, C. Tötzke, C. Quick, I. Manke, W. Lehnert, and V. Schmidt. Stochastic 3D modeling of non-woven materials with wet-proofing agent. *International Journal of Hydrogen Energy*, 38(20):8448–8460, 2013. doi: https://doi.org/10.1016/j.ijhydene.2013.04.144.

[155] S. Didari, Y. Wang, and T. A. Harris. Modeling of gas diffusion layers with curved fibers using a genetic algorithm. *International Journal of Hydrogen Energy*, 42(36):23130–23140, 2017. doi: https://doi.org/10.1016/j.ijhydene.2017.07.198.

[156] Y. Wang. Periodic surface modeling for computer-aided nano design. *Computer Aided Design*, 39(3):179–189, 2007. doi: https://doi.org/10.1016/j.cad.2006.09.005.

[157] M. Hossain, S. Z. Islam, A. Colley-Davies, and E. Adom. Water dynamics inside a cathode channel of a polymer electrolyte membrane fuel cell. *Renew. Energy*, 50:763–779, 2013. doi: https://doi.org/10.1016/j.renene.2012.08.041.

[158] S. S. Deshpande, L. Anumolu, and M. F. Trujillo. Evaluating the performance of the two-phase flow solver interfoam. *Computational Science & Discovery*, 5 (1):014016, 2012. doi: https://doi.org/10.1088/1749-4699/5/1/014016.

[159] J. Brackbill, D. Kothe, and C. Zemach. A continuum method for modeling surface tension. *Journal of Computational Physics*, 100(2):335–354, 1992. ISSN 0021-9991. doi: https://doi.org/10.1016/0021-9991(92)90240-Y.

[160] J. H. Ferziger and M. Perić. *Computational methods for fluid dynamics*. Springer, 2002.

[161] OpenFOAM Foundation. *OpenFOAM: The Open Source CFD Toolbox*, 2019. URL https://openfoam.org. Version 7.

[162] P. Sarkezi-Selsky, H. Schmies, A. Latz, and T. Jahnke. Lattice Boltzmann simulation of liquid water transport in gas diffusion layers of proton exchange membrane fuel cells: Impact of gas diffusion layer and microporous layer degradation on effective transport properties. *Journal of Power Sources*, 556:232415, 2023. doi: https://doi.org/10.1016/j.jpowsour.2022.232415.

[163] S. Sakaida, Y. Tabe, and T. Chikahisa. Large scale simulation of liquid water transport in a gas diffusion layer of polymer electrolyte membrane fuel cells using the lattice Boltzmann method. *Journal of Power Sources*, 361:133–143, 2017. doi: https://doi.org/10.1016/j.jpowsour.2017.06.054.

[164] Q. Liu, F. Lan, J. Wang, J. Chen, and C. Zeng. Numerical effect of random poral microstructures in stacking gas diffusion layers on water transport capability. *Journal of Power Sources*, 556:232440, 2023. doi: https://doi.org/10.1016/j.jpowsour.2022.232440.

[165] L. Zhu, H. Zhang, L. Xiao, A. Bazylak, X. Gao, and P.-C. Sui. Pore-scale modeling of gas diffusion layers: Effects of compression on transport properties. *Journal of Power Sources*, 496:229822, 2021. doi: https://doi.org/10.1016/j.jpowsour.2021.229822.

[166] L. Gamet, M. Scala, J. Roenby, H. Scheufler, and J.-L. Pierson. Validation of volume-of-fluid OpenFOAM® isoadvector solvers using single bubble benchmarks. *Computers& Fluids*, 213:104722, 2020. doi: https://doi.org/10.1016/j.compfluid.2020.104722.

[167] K. G. Lyras, B. Hanson, M. Fairweather, and P. J. Heggs. A coupled level set and volume of fluid method with a re-initialisation step suitable for unstructured meshes. *Journal of Computational Physics*, 407:109224, 2020. doi: https://doi.org/10.1016/j.jcp.2019.109224.

[168] J. López, A. Esteban, J. Hernández, P. Gómez, R. Zamora, C. Zanzi, and F. Faura. A new isosurface extraction method on arbitrary grids. *Journal of Computational Physics*, 444:110579, 2021. doi: https://doi.org/10.1016/j.jcp.2021.110579.

[169] S. Sakaida, Y. Tabe, K. Tanaka, and M. Konno. Study on water transport in hydrophilic gas diffusion layers for improving the flooding performance of polymer electrolyte fuel cells. *International Journal of Hydrogen Energy*, 46(10): 7464–7474, 2021. doi: https://doi.org/10.1016/j.ijhydene.2020.11.202.

[170] A. Mularczyk, Q. Lin, D. Niblett, A. Vasile, M. J. Blunt, V. Niasar, F. Marone, T. J. Schmidt, F. N. Buchi, and J. Eller. Operando liquid pressure determination in polymer electrolyte fuel cells. *ACS Applied Materials & Interfaces*, 13(29): 34003–34011, 2021. doi: https://doi.org/10.1021/acsami.1c04560.

[171] A. Bazylak, D. Sinton, Z.-S. Liu, and N. Djilali. Effect of compression on liquid water transport and microstructure of pemfc gas diffusion layers. *Journal of Power Sources*, 163(2):784–792, 2007. doi: https://doi.org/10.1016/j.jpowsour.2006.09.045.

[172] Z. Niu, Y. Wang, K. Jiao, and J. Wu. Two-phase flow dynamics in the gas diffusion layer of proton exchange membrane fuel cells: volume of fluid modeling and comparison with experiment. *Journal of The Electrochemical Society*, 165 (9):F613, 2018. doi: doi={https://doi.org/10.1149/2.0261809jes}.

[173] J. Liao, G. Yang, Q. Shen, S. Li, Z. Jiang, H. Wang, G. Zhang, Z. Li, and B. Sun. Simulation of the purging process of liquid water in a gas diffusion layer with a wetting gradient using the lattice Boltzmann method. *Transport in Porous Media*, 148(2):335–353, 2023. doi: https://doi.org/10.1007/s11242-023-01950-4.

[174] F. Wang and U. D. Schiller. Computational characterization of nonwoven fibrous media: I. Pore-network extraction and morphological analysis. *Physical Review Materials*, 4(8):083803, 2020. doi: https://doi.org/10.1103/PhysRevMaterials.4.083803.

[175] S. Simaafrookhteh, R. Taherian, and M. Shakeri. Stochastic microstructure reconstruction of a binder/carbon fiber/expanded graphite carbon fiber paper for pemfcs applications: mass transport and conductivity properties. *Journal of The Electrochemical Society*, 166(7):F3287, 2019. doi: https://doi.org/10.1149/2.0331907jes.

[176] D. Stoyan, J. Mecke, and S. Pohlmann. Formulas for stationary planar fibre processes II-partially oriented-fibre systems. *Statistics: A Journal of Theoretical and Applied Statistics*, 11(2):281–286, 1980. doi: https://doi.org/10.1080/02331888008801540.

[177] D. Jiao, K. Jiao, S. Zhong, and Q. Du. Investigations on heat and mass transfer in gas diffusion layers of PEMFC with a gas–liquid-solid coupled model. *Applied*

energy, 316:118996, 2022. doi: https://doi.org/10.1016/j.apenergy.2022.118996.

[178] J. Hinebaugh, J. Gostick, and A. Bazylak. Stochastic modeling of polymer electrolyte membrane fuel cell gas diffusion layers–Part 2: A comprehensive substrate model with pore size distribution and heterogeneity effects. *International Journal of Hydrogen Energy*, 42(24):15872–15886, 2017. doi: https://doi.org/10.1016/j.ijhydene.2017.04.268.

[179] A. Grießer, R. Westerteiger, E. Glatt, H. Hagen, and A. Wiegmann. Deep learning based segmentation of binder and fibers in gas diffusion layers. *Next Materials*, 6:100411, 2025. doi: https://doi.org/10.1016/j.nxmate.2024.100411.

[180] F. Calili-Cankir, E. M. Can, D. B. Ingham, K. Hughes, L. Ma, M. Pourkashanian, S. Lyth, and M. Ismail. Patterned hydrophobic gas diffusion layers for enhanced water management in polymer electrolyte fuel cells. *Chemical Engineering Journal*, 484:149711, 2024. doi: https://doi.org/10.1016/j.cej.2024.149711.

[181] J. Gostick, M. Aghighi, J. Hinebaugh, T. Tranter, M. A. Hoeh, H. Day, B. Spellacy, M. H. Sharqawy, A. Bazylak, A. Burns, and others. OpenPNM: a pore network modeling package. *Comput. Sci. Eng.*, 18(4):60–74, 2016. doi: https://doi.org/10.1109/MCSE.2016.49.

[182] Q. Xiong, T. G. Baychev, and A. P. Jivkov. Review of pore network modelling of porous media: Experimental characterisations, network constructions and applications to reactive transport. *Journal of contaminant hydrology*, 192:101–117, 2016. doi: https://doi.org/10.1016/j.jconhyd.2016.07.002.

[183] J. T. Gostick, Z. A. Khan, T. G. Tranter, M. D. Kok, M. Agnaou, M. Sadeghi, and R. Jervis. Porespy: A python toolkit for quantitative analysis of porous media images. *Journal of Open Source Software*, 4(37):1296, 2019. doi: https://doi.org/10.21105/joss.01296.

[184] J. T. Gostick. Versatile and efficient pore network extraction method using marker-based watershed segmentation. *Phys. Rev. E*, 96(2):023307, 2017. doi: https://doi.org/10.1103/PhysRevE.96.023307.

[185] R. Anderson, L. Zhang, Y. Ding, M. Blanco, X. Bi, and D. P. Wilkinson. A critical review of two-phase flow in gas flow channels of proton exchange membrane fuel cells. *Journal of Power Sources*, 195(15):4531–4553, 2010. doi: https://doi.org/10.1016/j.jpowsour.2009.12.123.

[186] R. Lenormand. Flow through porous media: limits of fractal patterns. *Proceedings of the Royal Society of London. A. Mathematical and Physical Sciences*, 423(1864):159–168, 1989. doi: https://doi.org/10.1098/rspa.1989.0048.

[187] M. Grimm, E. J. See, and S. G. Kandlikar. Modeling gas flow in pemfc channels: Part I–Flow pattern transitions and pressure drop in a simulated ex situ channel with uniform water injection through the GDL. *International Journal of Hydrogen Energy*, 37(17):12489–12503, 2012. doi: https://doi.org/10.1016/j.ijhydene.2012.06.001.

[188] L. Zhang, S. Liu, Z. Wang, and R. Li. Experimental and simulation analysis of liquid capillary fingering process in the gas diffusion layer. *Journal of Power Sources*, 554:232276, 2023. doi: https://doi.org/10.1016/j.jpowsour.2022.232276.

[189] P. K. Sinha and C.-Y. Wang. Pore-network modeling of liquid water transport in gas diffusion layer of a polymer electrolyte fuel cell. *Electrochimica Acta*, 52(28):7936–7945, 2007. doi: https://doi.org/10.1016/j.electacta.2007.06.061.

[190] D. Jiao, K. Jiao, Z. Niu, S. Zhong, and Q. Du. Water transport in the gas diffusion layer of proton exchange membrane fuel cell under vibration conditions. *International Journal of Energy Research*, 44(6):4438–4448, 2020. doi: https://doi.org/10.1002/er.5219.

[191] A. Ghanavati, S. Khodadadi, M. H. Taleghani, M. Gorji-Bandpy, and D. D. Ganji. Numerical simulation of the motion and interaction of bubble pair rising in a quiescent liquid. *Applied Ocean Research*, 141:103769, 2023. doi: https://doi.org/10.1016/j.apor.2023.103769.

[192] F. Vosoughi, G. Rakhshandehroo, M. R. Nikoo, and M. Sadegh. Experimental study and numerical verification of silted-up dam break. *Journal of Hydrology*, 590:125267, 2020. doi: https://doi.org/10.1016/j.jhydrol.2020.125267.

[193] W. Meng, C.-h. Yu, J. Li, and R. An. Three-dimensional simulation of silted-up dam-break flow striking a rigid structure. *Ocean Engineering*, 261:112042, 2022. doi: https://doi.org/10.1016/j.oceaneng.2022.112042.

[194] S. Malekzadeh and E. Roohi. Investigation of different droplet formation regimes in a T-junction microchannel using the VOF technique in OpenFOAM. *Microgravity Science and Technology*, 27:231–243, 2015. doi: https://doi.org/10.1007/s12217-015-9440-2.

[195] S.-R. Hysing, S. Turek, D. Kuzmin, N. Parolini, E. Burman, S. Ganesan, and L. Tobiska. *Proposal for quantitative benchmark computations of bubble dynamics*. Technische Universität, Fakultät für Mathematik, 2007.

[196] T. Wu and N. Djilali. Experimental investigation of water droplet emergence in a model polymer electrolyte membrane fuel cell microchannel. *Journal of Power*

Sources, 208:248–256, 2012. doi: https://doi.org/10.1016/j.jpowsour.2012.02.026.

[197] M. Shahraeeni and M. Hoorfar. Effect of gas diffusion layer properties on the time of breakthrough. *Journal of Power Sources*, 196(14):5918–5921, 2011. doi: https://doi.org/10.1016/j.jpowsour.2011.02.089.

[198] X. Wang, S. Chen, Z. Fan, W. Li, S. Wang, X. Li, Y. Zhao, T. Zhu, and X. Xie. Laser-perforated gas diffusion layer for promoting liquid water transport in a proton exchange membrane fuel cell. *International Journal of Hydrogen Energy*, 42(50):29995–30003, 2017. doi: https://doi.org/10.1016/j.ijhydene.2017.08.131.

[199] T. E. Springer, T. A. Zawodzinski, and S. Gottesfeld. Polymer electrolyte fuel cell model. *Journal of The Electrochemical Society*, 138(8):2334, aug 1991. doi: https://doi.org/10.1149/1.2085971.

[200] J. Sim, M. Kang, and K. Min. Effects of porosity gradient and average pore size in the in-plane direction and disposition of perforations in the gas diffusion layer on the performance of proton exchange membrane fuel cells. *Journal of Power Sources*, 544:231912, 2022. doi: https://doi.org/10.1016/j.jpowsour.2022.231912.

[201] C. Csoklich, H. Xu, F. Marone, T. J. Schmidt, and F. N. Buchi. Laser structured gas diffusion layers for improved water transport and fuel cell performance. *ACS Applied Energy Materials*, 4(11):12808–12818, 2021. doi: https://doi.org/10.1021/acsaem.1c02454.

[202] H. Jia, Y. Yu, B. Yin, F. Dong, X. Xie, and S. Xu. Influence of laser-perforated gas diffusion layer on mass transfer and performance of proton exchange membrane fuel cell. *International Journal of Energy Research*, 46(13):18634–18647, 2022. doi: https://doi.org/10.1002/er.8478.

[203] Z. Jiang, G. Yang, Q. Shen, S. Li, J. Liao, H. Wang, Z. Sheng, R. Ying, Z. Li, G. Zhang, and others. Study on gas transport performance in perforated gas diffusion layer by lattice Boltzmann method. *Transport in Porous Media*, 141 (2):417–438, 2022. doi: https://doi.org/10.1007/s11242-021-01726-8.

[204] K.-J. Lee, J. H. Nam, and C.-J. Kim. Pore-network analysis of two-phase water transport in gas diffusion layers of polymer electrolyte membrane fuel cells. *Electrochimica Acta*, 54(4):1166–1176, 2009. doi: https://doi.org/10.1016/j.electacta.2008.08.068.

Scientific publications

Author contributions

Co-authors are abbreviated as follows:
Danan Yang (DY), Himani Garg (HG), Martin Andersson (MA), Steven B. Beale (SB), and Patrick Fortin (PF).

Paper I: The influence of bipolar plate wettability on performance and durability of a proton exchange membrane fuel cell

D. Yang, P. Fortin, H. Garg, M. Andersson

This study is motivated by the experimental findings of our collaborator PF, showing that prolonged operation leads to a visible decline in the original hydrophobicity of bipolar plate surfaces. Experimental characterization at the fuel cell scale reveals that excessive utilization of bipolar plates results in accelerated degradation of fuel cell performance, primarily attributed to increased mass transport resistance. Channel-scale two-phase flow simulations suggest that this resistance is mainly caused by an increased risk of water flooding when using hydrophilic bipolar plates.

The candidate (DY) carried out the two-phase flow simulations, conducted the data post-processing, generated the figures, analyzed the results, and wrote the manuscript. PF performed the PEMFC experimental characterization and contributed to the manuscript by drafting the sections related to the experimental findings. MA and HG provided supervision and guidance throughout the simulations, manuscript preparation, and revision.

Paper II: Numerical simulation of two-phase flow in gas diffusion layer and gas channel of proton exchange membrane fuel cells

D. Yang, H. Garg, M. Andersson

This study investigates two-phase flow within a T-shaped GDL and GC domain, accounting for variations in GDL fiber diameters. While maintaining constant porosity across the GDLs, an increase in fiber diameter leads to reduced water saturation within the GDLs and an earlier breakthrough time. However, this also results in greater water accumulation within the GCs. Consequently, a more continuous liquid slug flow is observed in the GCs.

The candidate (DY) performed the two-phase flow simulations, carried out data post-processing, generated the figures, analyzed the results, and drafted the manuscript. MA and HG provided supervision and guidance throughout the simulation process, manuscript preparation, and subsequent revision.

Paper III: Effect of fiber curvature on gas diffusion layer two-phase dynamics of proton exchange membrane fuel cells

D. Yang, M. Andersson, H. Garg

In this study, liquid transport in GDLs with varying fiber curvatures is investigated using two-phase Volume of Fluid simulations implemented in OpenFOAM. A rod periodic surface model is employed in conjunction with a layer-by-layer fiber stacking strategy to reconstruct the GDL microstructures. The simulation results show that increased fiber curvature enhances pore connectivity and leads to higher water saturation and capillary pressure, thereby increasing the risk of flooding. Furthermore, GDLs with curved fibers present a more consistent water saturation across the same type of GDLs.

The candidate (DY) carried out the two-phase flow simulations, conducted the data post-processing, generated the figures, analyzed the results, and wrote the manuscript. MA and HG provided supervision and guidance throughout the simulations, manuscript preparation, and revision.

Paper IV: Two-phase fluid dynamics in proton exchange membrane fuel cells: counter-flow liquid inlets and gas outlets at the electrolyte-cathode interface

D. Yang, S. B. Beale, H. Garg, M. Andersson

This study employs the VOF method to investigate liquid behavior under various GDL liquid injection configurations, including the presence of gas outlets. The results demonstrate that the injection location and configuration significantly influence saturation levels, stabilization processes, and breakthrough dynamics within the GDL. Furthermore, comparative analyses with and without air outflow reveal distinct counter-flow interactions in GDLs and notable differences in two-phase transport characteristics within the interconnected GCs.

The candidate (DY) carried out the two-phase flow simulations, conducted the data post-processing, generated the figures, analyzed the results, and wrote the manuscript.

SB provided support in writing and reviewing the manuscript. MA and HG provided supervision and guidance throughout the simulations, manuscript preparation, and revision.

Paper V: Numerical investigation of two-phase flow transport in additive-treated gas diffusion layers for proton exchange membrane fuel cells

D. Yang, M. Andersson, H. Garg

This study extends previous investigations that have neglected the additive structures within GDLs. To evaluate the influence of these additives, image-processing techniques are integrated with established GDL reconstruction methods to incorporate additive structures. Furthermore, GDLs with and without including additives are compared. The results demonstrate a significant impact of the additives on the pore network morphology and the resulting water saturation within the GDLs. However, at a high contact angle, the total water volume within the GDLs remains hardly changed, providing a reference point for relating water saturation levels before and after accounting for additive structures.

The candidate (DY) carried out the two-phase flow simulations, conducted the data post-processing, generated the figures, analyzed the results, and wrote the manuscript. MA and HG provided supervision and guidance throughout the simulations, manuscript preparation, and revision.